Multiscale and Upscaling Methods for Geophysical Electromagnetic Forward Modeling

by

Luz Angélica Caudillo Mata

B.Sc. Computer Science, University of Guanajuato, 2004

M.Sc. Computer Science and Industrial Mathematics,

Mathematics Research Center (CIMAT), 2008

A THESIS SUBMITTED IN PARTIAL FULFILLMENT

OF THE REQUIREMENTS FOR THE DEGREE OF

Doctor of Philosophy

in

THE FACULTY OF GRADUATE AND POSTDOCTORAL STUDIES

(Geophysics)

The University of British Columbia

(Vancouver)

October 2017

Abstract

Accurate and efficient simulation of electromagnetic responses in realistic geo-physical settings is crucial to the exploration, imaging, and characterization of buried natural resources, such as mineral and hydrocarbon deposits. However, in practice, these simulations are computationally expensive. The geophysical settings consider highly heterogeneous media and features at multiple spatial scales that require a very large mesh to be accurately represented. This results in a system of equations to be solved that often exceeds the limits of average computers. Thus, the key is to reduce the problem size but retain the accuracy of the electromagnetic responses.

Upscaling and multiscale techniques have been successfully applied to the problem of simulating fluid flow through heterogeneous porous media, where they are able to drastically reduce the size of the resulting fine-mesh system by casting it into a coarse-mesh system that is much cheaper to solve, while achieving a level of accuracy similar to that obtained with conventional discretization schemes. Recognizing the success that such techniques have had in fluid flow applications, this dissertation extends their use for application to electromagnetic modeling.

In this dissertation, two new parallel simulation methods for the quasi-static Maxwell's equations in the frequency domain are proposed: an upscaling framework for the electrical conductivity, and a multiscale finite volume with oversampling method. Both methods are combined with an adaptive mesh refinement technique (OcTree) to boost their computational performance. The performance of these methods is demonstrated by using field-inspired and synthetic examples that include a large electrical conductivity contrast.

This investigation shows that both proposed methods are feasible to tackle geophysical electromagnetic problems, where being able to reduce the size of the problem can be particularly advantageous when extended domains are considered or when the mesh must capture the spatial distribution of the media heterogeneity outside the region where the electromagnetic responses are measured. Furthermore, both methods are new contributions to the literature in the field of computational methods in geophysical electromagnetics. Finally, both methods increase the current predictive and analytic capabilities by making the simulation of electromagnetic responses in larger and more complex geophysical settings more feasible than currently is possible.

Lay Summary

The focus of this investigation is to study how to reduce the computational cost of simulating the behavior of electromagnetic fields in complicated geophysical settings. This type of simulations are crucial to the exploration of buried natural resources (mineral, groundwater and hydrocarbon deposits) using electromagnetic methods. However, the size of the computation they involve often exceeds the limits of average computers. This investigation proposes two innovative mathematical alternatives (an upscaling and a multiscale with oversampling method) that achieve a great reduction of the problem's size and the simulation cost without sacrificing much accuracy. It also opens the door to use such alternatives to create more powerful computational environments capable of simulating electromagnetic fields in larger and more complex geophysical settings than currently is possible. Furthermore, this study is the first one in the literature to demonstrate the practical use of the proposed alternatives in the context of geophysical electromagnetic problems.

Preface

All of the work presented henceforth was conducted at the Geophysical Inversion Facility in the Department of Earth, Ocean and Atmospheric Sciences at the University of British Columbia (UBC), Point Grey campus. This research resulted in two peer-reviewed publications and in three expanded conference proceedings. I presented this research in eleven international conferences.

Chapter 3 presents extended and revised versions of the publications:

1. L. A. Caudillo-Mata, E. Haber, L. J. Heagy, and C. Schwarzbach, *A framework for the upscaling of the electrical conductivity in the quasi-static Maxwell's equations*, J. Comput. Appl. Math., vol. 317, pp. 388 to 402, 2017

2. L. A. Caudillo-Mata, E. Haber, L. J. Heagy, and D. W. Oldenburg, *Numerical upscaling of electrical conductivity: A problem specific approach to generate coarse-scale models*, in SEG Technical Program Expanded Abstracts 2014, 2014, pp. 680 to 684.

I was the lead investigator, responsible for all major areas of concept formation, background investigation, software development, simulation process, analysis of results, as well as manuscript composition. D. W. Oldenburg and L. J. Heagy were involved in the early stages of concept formation, the design of the simulations presented in Section 3.5.1 and their corresponding analysis of results, and contributed to manuscript edits for the SEG expanded abstract. L. J. Heagy also contributed to manuscript revision and edits for the peer-reviewed publication. C. Schwarzbach contributed to software development and the design of the simulations presented in Section 3.5. E. Haber was the supervisory author on this study and contributed in all related processes to the project at all its stages.

Chapter 4 presents extended and revised versions of the publications:

1. L. A. Caudillo-Mata, E. Haber, and C. Schwarzbach, *An oversampling technique for the multiscale finite volume method to simulate electromagnetic responses in the frequency domain*, Computational Geosciences, 2017, doi:10.1007/s10596-017-9647-y

2. L. A. Caudillo-Mata, E. Haber, and C. Schwarzbach, *An oversampling technique for the multiscale finite volume method to simulate frequency-domain electromagnetic responses*, in SEG Technical Program Expanded Abstracts 2016, 2016, pp. 981 to 985.

3. L. A. Caudillo-Mata, E. Haber, and C. Schwarzbach. *A multiscale finite volume method with oversampling for geophysical electromagnetic simulations*. In EAGE - ECMOR XV - 15th Eur. Conf. Math. Oil Recover. - Expand. Abstr., 2016. doi:10.3997/2214-4609.201601892.

I was the lead investigator, responsible for all major areas of concept formation, background investigation, simulation process, analysis of results, as well as manuscript composition. C. Schwarzbach and I developed the necessary software to run the simulations; together we conceived and analyzed the experiments. I performed all the experiments presented in Section 4.4. E. Haber was the supervisory author on this study and contributed in all related processes to the project at all its stages.

Table of Contents

List of Tables

List of Figures

xv

Glossary

DOF Degrees of Freedom

EM Electromagnetic

FD Finite Difference discretization method

FE Finite Element discretization method

FV Finite Volume discretization method

MFV Mimetic Finite Volume discretization method

MSFV Multiscale Finite Volume Method

MSFV+O Multiscale Finite Volume Method with Oversampling

PDE Partial Differential Equation

SPD Symmetric Positive Definite

UBC University of British Columbia

Acknowledgments

This dissertation represents a long-awaited dream, which to be honest, there were some times I thought I will not be able to realize. In this space, I want to acknowledge to those who have provided me with words of wisdom to overcome my mental barriers in those difficult moments, as well as to those who have contributed to make my PhD experience outstanding. Two pages are not enough to express my deep gratitude to you all!

At the top of the list is my advisor, Dr. Eldad Haber. Eldad, you have earned my deepest gratitude, admiration, and respect not only as a scientist, but also as a human being. Thank you for providing me with the right balance of freedom and guidance during my PhD; it allowed me to recognize and nurture my own 'scientific voice'. Thank you for taking me as a student, for providing me with continuous support (emotional, scientific, financial) when I have needed it the most, for pointing me to truly interesting and exciting projects to work on, and for continuously challenging me and helping me to grow.

I also thank the members of the GIF research group. I was truly blessed to be surrounded by such an extraordinary, diverse, and well-rounded group of people. I benefited a lot from the can-do culture of our group. The standards that you set for yourselves in the quality of your work helped me to set a high standard for me to try to live up to. Special thanks to Dr. Doug Oldenburg for his scientific vision and for his efforts (including Christmas dinners, dragon boating, and hikes) on maintaining a cohesive group throughout time. Thanks as well to Christoph, Jenn, Klara, Kris, Gudni, Dominique, Sarah, Lars, Eran, Lindsey, and Wenke for their insightful contributions to improve my work and for fun.

I also thank Drs. D. Oldenburg and M. Friedlander for being part of my supervisory committee and for their valuable contributions to improve my dissertation; to Drs. U. Ascher, C. Greif, A. Adem, M. Lamoureux, B. Homsey, and B. Wetton for their wisdom when I needed good advice; and to Dr. F. Herrmann for inviting me to work on geophysical inverse problems when I started at UBC, which let me to pursue research in this field.

Many thanks for the funding provided to pursue my studies by UBC through a Four-Year fellowship, EOAS through a H. W. Matthews scholarship, Mitacs through its Acceler-

Dedication

*A mi querida familia: Elias, Ramona, Isauro, Missael, Hiram,
Michelle, Ximena, Alan, Axel.
[To my beloved family: Elias, Ramona, Isauro, Missael, Hiram,
Michelle, Ximena, Alan, Axel.]*

*A mi entrenador de ajedrez: Marco Antonio Rodríguez Ortega.
[To my chess coach: Marco Antonio Rodriguez Ortega.]*

Chapter 1

Introduction

Everything can be taken from a person but one thing: the last of the human freedoms – to choose one's attitude in any given set of circumstances, to choose one's own way. — Viktor Frankl

1.1 Motivation

Since their inception in the early 1900s, geophysical electromagnetic (EM) methods have been used in industrial, geoscientific and engineering applications worldwide to detect, locate and characterize buried natural resources of economic significance. Currently, the two dominant commercial uses of geophysical EM methods are in exploration and monitoring of mineral deposits and hydrocarbon (oil and gas) reserves (see [91, 139, 153, 166, 179] and references within). Other commercial uses include exploration of geothermal and groundwater deposits (e.g. [42, 155]), detection of buried unexploded ordnance (e.g. [154]), and monitoring environmental impact, such as carbon dioxide sequestration (e.g. [42]).

Geophysical EM methods infer underground structures from measurements of electric and/or magnetic fields that are acquired through a variety of survey settings [144, 161]. A geophysical EM survey consists of one or several EM experiments. Figure 1.1 shows an example of a typical EM experiment setup used in the mining exploration.

A typical EM experiment starts by energizing the ground using an electromagnetic source, which can be harmonic or transient, natural or controlled (cf.

[144]). The energy propagates throughout the subsurface and induces secondary electromagnetic fields in the regions where there is a (high) contrast in electrical conductivity (Figure 1.1). Electrical conductivity is the physical property of the ground that quantifies the ability of a material to allow the flow of electric currents, and it is used in exploration geophysics to characterize Earth's (conductive or resistive) materials [161]. Next, EM measurements or data containing information of the distribution of the subsurface conductivity are recorded by placing receivers at the Earth's surface, in the air, in the sea, or in wells. The experiment is typically repeated for various source and receiver locations, resulting in a large volume of data. Subsequent processing, modeling and inversion of EM data is performed to construct detailed subsurface electrical conductivity models. The geological interpretation and assessment of these conductivity models allows the understanding of the spatial distribution of the underground structures, and it ultimately leads to better-informed exploration decisions. Figure 1.2 shows the concept of a geophysical inversion of EM data.
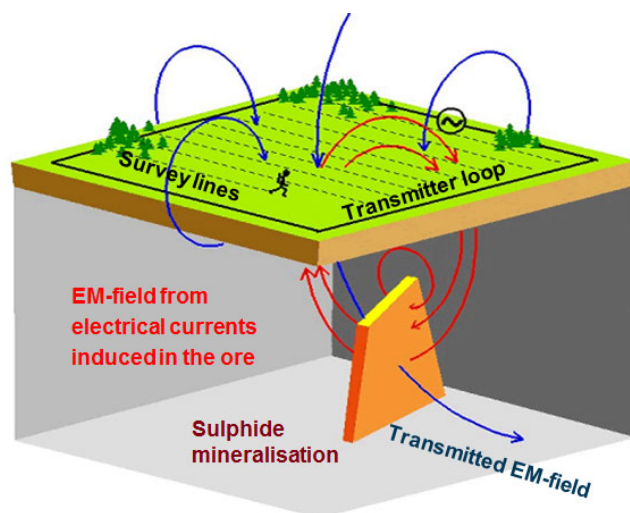
Figure 1.1: Sketch of a geophysical large-loop EM experiment used in mining exploration and the induced secondary EM fields generated by the mineralized conductive body. Figure courtesy of Boliden Group (www.boliden.com).
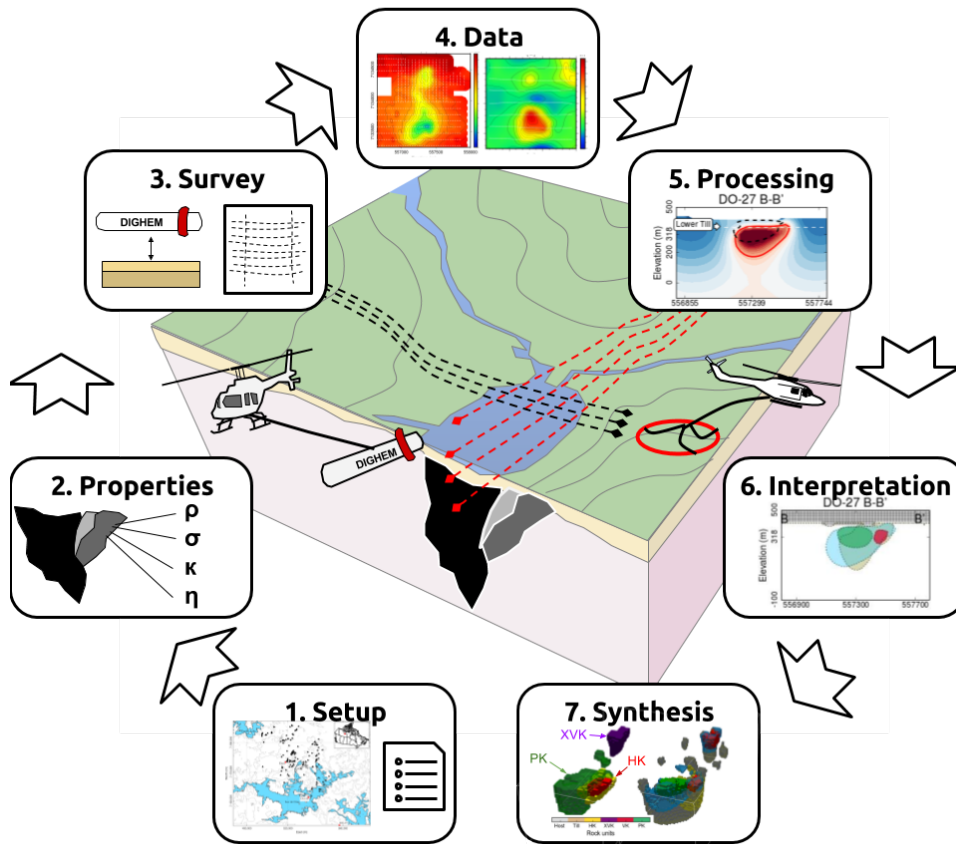
Figure 1.2: Geophysical inversion of EM data for natural resource exploration. The output is an electrical conductivity model of the underground structures that were surveyed. Figure taken from the EM geosci website: https://em.geosci.xyz, which distributes its content under Creative Commons 4.0.

Modeling and inversion of geophysical EM data are powerful interpretation tools; however, using them as part of exploration programs in industry is both time consuming and computationally challenging [19, 68, 134, 139, 153, 166, 179].

Inversion of EM data is achieved by solving a non-linear and (often) large-scale inverse problem using optimization techniques [138, 159]. The major bot-

tleneck of performing an inversion is to solve the forward problem. The EM forward problem is the mathematical procedure by which, given information of the physical properties of the medium and the sources, we can predict (simulate) EM data through numerically solving the corresponding governing Maxwell's equations [156, 159, 169]. That is, the solution of the forward problem involves a numerical process for solving a partial differential equation (PDE) or a system of PDEs (depending on the formulation of Maxwell's equations that is chosen to work with). In the geosciences, solving a forward problem is also referred as forward modeling or just modeling. Besides playing a key role within an inversion, the EM forward problem is by itself crucial to simulate physical processes governed by EM induction phenomena — which has a rich spectrum of applications in different fields of knowledge, including, medical imaging and the various engineering branches (electrical, mechanical, materials, to name a few) [58, 78, 129, 156].

Even though there has been significant progress in advancing existing computational EM capability, solving the forward problem for realistic, large-scale geophysical settings remains a computational challenge (see [19, 68, 134, 139, 153, 166, 179] and references within). As we will see in the next section, such challenge consists on dealing effectively with the elevated computational cost (both in CPU memory and run time) of this type of simulations. Therefore, working towards faster and more accurate computational solutions for the geophysical EM forward problem will have a tangible impact in the overall processes of imaging and monitoring buried natural resources using geophysical EM methods.

1.2   Problem Statement

Accurate and efficient simulation of EM responses — EM fields and fluxes — through solving the EM forward problem for realistic, large-scale geophysical settings can be a very computationally expensive task, specially when conducted within an EM inversion procedure (see [22, 68, 134, 179] and references within). The major challenge in practice to perform this type of (forward) simulation is the size of the computation it involves.

Realistic geophysical settings typically consider large computational domains in 3D; geologic, topographic, and other simulation-related features that vary at

4

multiple spatial scales; and a wide variation over several orders of magnitude of the physical properties (e.g. electrical conductivity) of the heterogeneous media. Figure 1.3 shows one example of a complex geophysical setting that can be encountered in practice, where some features in the model can vary from millimeters upward (e.g. the thickness of the casing of wells), while the simulation domain can be on the order of hundreds of kilometers. In addition, the electrical conductivity of Earth's materials varies over many orders of magnitude [161]. For the example shown in Figure 1.3, the values of the electrical conductivity can range from 10^{-8} to 10^6 S/m, when the setting considers air and steel well casing, which correspond to the features in the model that are less and most conductive, respectively.

Since all of the features considered in a geophysical setting can have a significant impact on the behavior of the EM responses of interest (that are typically measured at the surface), if we need to obtain an accurate approximation to the responses, the mesh used in traditional discretization techniques, such as finite volume or finite element, should be able to capture the structure of the heterogeneity present in the setting with sufficient detail. This need leads to the use of a very large mesh to discretize the model, which results into solving a very large, and often very ill-conditioned, system of equations — in some cases, in the order of millions (10^6), or even larger than billions (10^9) of unknowns. For the geophysical setting shown in Figure 1.3, the system of equations (depending on the level of detail considered in the model) can lead to a system in the order of 10^{12} of unknowns. Such a large system of equations require specialized computing resources (e.g. clusters) to be solved. When an EM simulation is conducted in practice (e.g. for different frequencies or survey configurations) or within an EM inversion procedure (where there is the need to deal with adjoint operators per frequency and/or source), several forward EM simulations must be conducted (the book in [68] gives a more detail estimate of the number of linear systems to be solved). This can lead to a very computational expensive process overall, and therefore it is of interest to reduce effectively the computational cost of individual EM simulations.

Conventional approaches used to reduce the computational cost of EM forward simulations are: parallel computing, adaptive mesh refinement, and iterative solvers. The combination of these three approaches is one of the most efficient
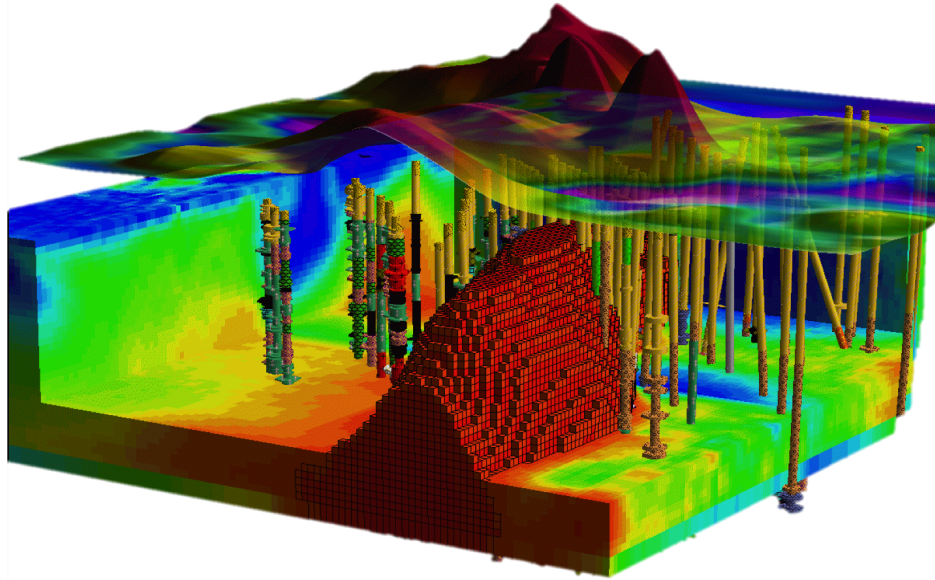
Figure 1.3: Example of a realistic geophysical EM setting that considers a large computational domain, features that vary at multiple spatial scales (millimeters, meters, and kilometers), and a wide variation over several orders of magnitude of the physical properties of the medium. Figure not drawn to scale. Figure courtesy of Rockware, Inc (www.rockware.com).

ways currently used to tackle this problem [68, 134]. However, the ever increasing need to accurately simulate larger and more complex settings, which requires us to be able to include more detail in the modeling stage, limits their sustainability [22]. As we see next, each individual approach faces some issues to reduce the size of the computation, in terms of both CPU memory and time requirements.

Parallel computing drastically reduces the run time of the simulation by breaking the problem into discrete pieces of work that can be carried out simultaneously using multiple processors; however, the size of the system of equations is not reduced. The workload is merely distributed among processors. See [100, 134] for a recent review of high-performance computational strategies for EM modeling.

Adaptive mesh refinement (AMR) approaches have been used to overcome (reduce) the computational cost of EM modeling in geophysical applications (e.g.

[72, 86, 108, 118, 149]). They do so by refining selected areas of the mesh to meet certain error bounds based on the requirements of the problem. AMR approaches have produced accurate approximations to the EM responses at an affordable cost; however, when used to simulate geophysical EM responses in heterogeneous settings, the mesh must still capture the relevant features in the spatial distribution of the media heterogeneity both inside and outside the region where we measure the EM responses. This restricts the ability of AMR approaches to reduce the size of the system to be solved.

Efficient iterative solvers and preconditioners have been developed for the large, sparse, and ill-conditioned system of equations that results from the discretization of the Maxwell's equations (e.g. [63, 64, 68, 70, 71, 83, 134, 172]). These solvers lead to substantial savings on time and memory usage, as they are based on optimized (sparse) matrix-vector product multiplications and do not require to store the matrix of the system [146]. Nevertheless, using iterative solvers to solve the EM forward problem as part of an EM inversion routine suffer a major drawback: the system needs to be solved multiple times for the number of sources and the different frequencies or time steps in the geophysical EM survey configuration [68], which can be in the order of thousands or even millions (e.g. an airborne survey) [144]. In such cases, being able to use direct solvers to decompose the matrix of the system of equations is the most cost-effective way to overcome this issue [43, 68]. However, a matrix factorization requires us to be able to store the matrix.

The issues described suggest the need for a new computational framework capable of reducing the size of the system of equations more effectively. Furthermore, the new framework needs to be able to compute accurate approximations for the EM problem at a coarser resolution, such that the impact caused by small-scale features in the model is still included but without resolving for such small-scale features. For instance, in the example provided in Figure 1.3, we can not afford to mesh the model at the millimeter scale when the domain varies over hundreds of kilometers. Instead, we need an accurate approximation to the solution at the meter scale that includes the effect due to the presence of the relevant millimetric conductive feature (casing) in the model. Moreover, the new framework must be able to leverage most, if not all, of the advantages of the methods

7

described above. That is, it needs to run in parallel, be able to work with adaptive mesh refinement, and be accurate and cost-effective.

The literature reports that upscaling and multiscale (finite volume and finite element) methods provide parallel methods to solve linear, elliptic PDE problems with multiple scale features and highly heterogeneous settings. For such type of PDE problems, both of these methods are able to compute large-scale physical solutions that capture the small-scale effect accurately and efficiently without resolving for the small-scale features in the model [49, 51, 56, 88, 89].

Favorably, upscaling and multiscale methods have been rigorously studied in the field of petroleum engineering for the problem of modeling (single-phase) fluid flow through highly heterogeneous porous media, whose governing PDE model is the steady-state, linear Poisson's equation (cf. [6, 51]). Such a problem shares several key challenges similar to the problem of simulating geophysical EM responses in highly heterogeneous settings, namely, the governing PDE model in both problems is linear, the simulation considers large-scale computational domains, features varying at multiple spatial scales, and a wide variation over several orders of magnitude of the physical properties (e.g. permeability) of the media. For single-phase flow in porous media problems, these two methods have been successfully used to drastically reduce the size of the fine-mesh system from the discretization of the Poisson's equation by constructing a coarse-mesh version of the system that is much cheaper to solve, while achieving a level of accuracy similar to that obtained with traditional discretization schemes (e.g. finite element or finite volume) on a fine mesh [49–51, 56, 60, 80, 81, 88, 101, 122, 123, 132, 141, 175].

Since the use of upscaling and multiscale techniques has not been rigorously investigated for application to geophysical EM modeling, in this dissertation, I investigate how these two techniques can be extended to do so. At present, developing efficient multiscale methods using different discretization schemes and tailoring them for use to diverse applications is an active research area (e.g. [38, 39, 59, 87, 114] and references within).

1.3   Aim and Scope of the Study

The *aim* of this study is to investigate the applicability and feasibility of using up-scaling and multiscale (finite volume and finite element) techniques to efficiently solve the geophysical EM forward problem for complex settings that include features varying at multiple spatial scales and several orders of magnitude. I develop the aim of this study by focusing on answering the following research questions:

- How to extend the core mathematical ideas of some successful upscaling and multiscale methods developed for the problem of simulating fluid flow in highly porous media for application to the problem of simulating geophysical EM responses in highly heterogeneous conductive media? That is, how to extend some of the core mathematical procedures developed for a linear scalar PDE model (i.e. the Poisson's equation) to a linear vector PDE model (i.e. the Maxwell's equations)?

- How do upscaling and multiscale methods perform for geophysical EM problems with highly heterogeneous settings when they are combined with an adaptive mesh refinement technique? In particular, can these methods be used to drastically reduce the size of the system of equations to be solved?

In order to answer these questions, the *scope* of this study is focused solely on geophysical EM problems in the frequency domain where the quasi-static approximation applies. The quasi-static approximation of EM fields refers to the fact that the contribution of the electric current displacement is negligible compared to the electric current density when working at frequencies lower than 10^5 Hz [169]. This is the case for a wide range of geophysical EM surveys used in practice. For example, we can model the EM responses of controlled-source EM surveys (e.g. large-loop surface and airborne surveys) and natural-source EM surveys (e.g. magnetotellurics and ZTEM surveys). The books in [144, 161] include a thorough description for each of these surveys.

Since most geophysical EM surveys in the quasi-static regime aim to characterize the electrical conductivity, we assume that the electrical conductivity is the primary medium's physical property of interest in this study [138, 144, 161, 179].

1.4 Overview of the Study

Given the background information and proposed problem statement in this introductory chapter, the rest of this dissertation is organized as follows.

Chapter 2 introduces the quasi-static Maxwell's equations in the frequency domain, which is the mathematical model I focus on in this dissertation; provides an overview of the mimetic finite volume discretization method, which is used as a building block to develop the upscaling and multiscale techniques proposed in this work; and provides a summary of the relevant problem characteristics, the literature review as well as related work.

Chapter 3 develops an upscaling framework for the electrical conductivity of the quasi-static Maxwell's equations in the frequency domain. The goal of such framework is to construct accurate coarse-mesh conductivity models from given fine-mesh ones that can be used to accurately simulate EM responses on a coarse mesh. The main contribution of this chapter is to pose upscaling as a parameter estimation problem to be solved on each coarse-mesh cell, which is fundamentally different than other upscaling formulations proposed in the literature. This chapter starts by introducing the components for the framework that are used to propose a general least-squares formulation for the upscaling problem in geophysical EM applications. Then, I use a 1D example to illustrate the general principle behind the framework and to show its performance to upscale well log electrical conductivity data from the Canadian McMurray formation. This example provides the perfect scenario to test our upscaling framework and to offer a potential alternative to upscale well log electrical conductivity data in practice. Afterwards, I adapt the upscaling formulation to construct coarse-mesh 3D anisotropic electrical conductivity models from given fine-mesh isotropic models. Finally, I show the performance of the adapted upscaling formulation for 3D problems using two upscaling examples on a single coarse cell, and one example of a synthetic electrical conductivity model from inversion results of field measurements over the Canadian Lalor mine. The last example also shows how the upscaling method can be combined with OcTree (a type of adaptive mesh refinement technique) in a parallel environment to boost its performance.

Chapter 4 develops a multiscale finite volume method with oversampling for

the quasi-static Maxwell's equations in the frequency domain. The goal of this method is to provide more accurate approximations to the EM responses than those obtained with the multiscale finite volume technique (without oversampling) developed by [73] for tensor meshes and at a fraction of the cost of traditional discretization techniques (such as mimetic finite volume) on a fine mesh. The main contribution of this chapter is to show how the core mathematical ideas used to develop one of the most successful oversampling techniques for flow in porous media applications can be extended to geophysical EM problems, as well as to show how the multiscale finite volume method with and without oversampling can be combined with OcTree meshes in a parallel environment to tackle more challenging geophysical EM simulations. This chapter starts by providing a summary of a multiscale finite volume method for geophysical EM problems. I discuss how the accuracy of such method can be improved by complementing it with an oversampling technique. Finally, I show the performance of the method using two 3D synthetic models: the Lalor model (introduced in Chapter 3), and one with random isotropic heterogeneous media.

Finally, Chapter 5 summarizes the work, discusses the contribution of this investigation to the field of computational EM, and discusses the remaining challenges and future research directions of the work presented in this dissertation.

Chapter 2

Mathematical Background

Live as if you were to die tomorrow.
Learn as if you were to live forever. — Mahatma Gandhi

2.1 Overview

This chapter provides a literature review of the numerical methods used to solve the quasi-static EM forward problem in the frequency domain, introduces the mathematical model I focus on in this dissertation, provides an overview of the mimetic finite volume discretization method, discusses the existing solvers for the resulting system of equations obtained from the discretization of the Maxwell's equations using the mimetic finite volume method, and concludes with a literature review of the related upscaling and multiscale techniques developed for flow in porous media problems that are used as a building block to develop the upscaling and multiscale with oversampling methods proposed in this doctoral dissertation for application to geophysical EM problems.

2.2 The Electromagnetic Forward Problem

This section provides a literature review of the conventional methods that are used to solve the geophysical quasi-static EM forward problem in the frequency domain.

In Geophysics, the EM forward problem or forward modeling refers to the mathematical procedure by which given information of the physical properties of

the medium (e.g. spatial distribution of both the electrical conductivity and magnetic permeability) and the sources, we can predict (compute) geophysical EM data (responses) by numerically solving the Maxwell's equations [158, 169]. The empirical Maxwell's equations are widely accepted in the scientific community as the mathematical model that governs all macroscopic EM phenomena [58, 156].

Over the last four decades, the scientific community has been proposing efficient numerical methods to solve the EM forward problem for different geophysical applications [5, 7, 19, 34, 53, 68, 70, 76, 106, 142, 153, 157, 166, 179]. The progress has happened on several fronts in the fields of scientific and high-performance computing. Nowadays, we have a broader set of numerical methods (e.g. adaptive mesh refinement and discretization techniques, solvers and preconditioners) to use as well as more powerful machines to run the simulations. This progress has enabled modelers to increase the complexity of the simulation. For example, we went from 1D settings to 3D settings, from small-scale to large-scale domains, from simple homogeneous or layered models that consider targets in the form of blocks to highly heterogeneous models that consider more complicated geological and topographical structures. In particular, performing 3D simulations has been possible due to the increase in computing power we have had over the last two decades [134, 179]. Currently, we are still not at the point where we can fully tackle computationally this problem. For example, running an EM forward simulation on a geophysical setting as the one showed in Figure 1.3 can not be handled without specialized computing resources (e.g. a cluster supercomputer), to which few people have access.

To propose a better strategy to solve the geophysical EM forward problem, we first need to understand how it has been traditionally solved. The conventional approach to solve this problem consists of the following three major steps:

1. Select a well-posed boundary value problem (in the sense of Hadamard) that represents the physical phenomenon of interest. A well-posed boundary value problem in the sense of Hadamard consist of a PDE model with boundary conditions that has a unique solution, which depends continuously on the input [77].

   The quasi-static Maxwell's equations are the established mathematical PDE

13

model to simulate physical responses resulting from a geophysical EM experiment [68, 169]. This model can be formulated in the frequency or time domain. For the sake of simplicity of exposition, I focus on frequency-domain EM problems. In addition, the model can be formulated in first-order or second-order form. The literature reports that using the first-order form leads to more accurate results when both EM fields and fluxes need to be computed [68]. In this dissertation, I work with the first-order formulation for this reason.

Section 2.3 provides full details about the boundary value problem I work with in this dissertation.

2. Discretize the quasi-static Maxwell's equations using an appropriate mesh and discretization method.

The mesh used in this step can be structured, semi-structured or unstructured. The literature reports that structured and semi-structured meshes are used more often than unstructured meshes for the geophysical EM forward problem. However, there is increasing research on how to use effectively unstructured meshes as well (e.g. [100, 115, 150] and references within).

Structured and semi-structured meshes have the advantage of leading to more accurate solutions, structured, symmetric and sparse matrices, as well as being simpler to program and parallelize. Their main disadvantage is that they cannot model effectively complicated geometries (e.g. Figure 1.3). The most common structured and semi-structured meshes used in practice are: tensor meshes (i.e., any mesh that has a constant width along the entire axis such that it can be defined by a single width vector), orthogonal locally refined meshes (e.g. QuadTree and OcTree), and logically orthogonal meshes (i.e., a distorted orthogonal mesh) [68].

Conventional discretization methods for this step are: the finite difference discretization method (FD) (e.g. [41, 99, 106, 178] and references within), the finite element discretization method (FE) (e.g. [100, 104, 115, 130, 131, 149]), the finite volume discretization method (FV) (e.g. [54, 68, 100]), and the Integral Equation method (e.g. [8, 126, 168]). The Integral Equation

method has been reported to be less competitive than the other methods [149]; it cannot deal with large conductivity contrasts neither with complicated geometries and it involves large dense matrices, which increase the cost of solving the system of equations. Currently, the most common discretization methods used in practice for our problem are FD and FV methods on orthogonal structured or semi-structured meshes, and FE on structured and unstructured meshes.

The state-of-the-Art is to use a mimetic discretization method as it results on discrete solutions that preserve (mimic) the relevant underlying mathematical and physical properties of the continuum PDE model on general polygonal and polyhedral meshes, and it leads to sparse and symmetric systems of equations [68, 121]. Mimetic discretizations have been derived for FD, FE and FV methods [93–96, 104, 121, 131]. In this dissertation, we use the mimetic finite volume discretization method (covered in detail in Section 2.4) on tensor and OcTree meshes. Section 2.4 elaborates further on the advantages of using this discretization method as well as on the physical properties that this mimetic discretization preserves for the quasi-static Maxwell's equations.

3. Solve the linear system of algebraic equations resulting from the previous step to obtain an approximation to the EM responses. Section 2.5 discusses the solver options for the system of equations that we actually solve in this dissertation.

Using the conventional approach outlined above to solve the quasi-static EM forward problem in practice is computationally very expensive. As discussed in Section 1.2, the cost comes from solving a very large system of equations that results from the discretization of a complex geophysical setting that includes features at multiple spatial scales (e.g. Figure 1.3), which often requires a very detailed mesh. As pointed out in [22, 23, 122], just building more powerful machines does not constitute a sustainable methodology to solve this problem as the amount of processing increases too steeply with the rise in problem size. As discussed in Section 1.2, this study proposes two new methods, an upscaling method and a multiscale method with oversampling, to overcome this situation.

15

2.3 The Quasi-static Maxwell's Equations in the Frequency Domain

This section introduces the boundary value problem I focus on in this dissertation. More detailed discussions on EM theory for geophysical applications can be found in [144, 156, 161, 169].

Due to attenuation of the EM responses in the earth, geophysical EM surveys usually utilize frequencies in the range $(0, 10^5)$ Hz, in which case electrical displacement currents can be neglected [169]. For this scenario, the governing mathematical model is given by the first-order form of the quasi-static Maxwell's equations ([68, 169]):

$$\nabla \times \vec{E} + \iota\omega\vec{B} = \vec{0}, \quad \text{in } \Omega, \tag{2.1}$$

$$\nabla \times \mu^{-1}\vec{B} - \Sigma\vec{E} = \vec{J}_s, \quad \text{in } \Omega, \tag{2.2}$$

where $\vec{B}$ denotes the magnetic flux density, $\vec{E}$ denotes the electric field intensity, $\vec{J}_s$ denotes the source term, ω denotes the angular frequency, ι is the unit imaginary number, and $\Omega \subset \mathbb{R}^3$ denotes the domain. The PDE coefficients, μ and Σ, denote the magnetic permeability and electrical conductivity, respectively. Note that the system of equations (2.1)-(2.2) constitutes a linear, complex and vector PDE system.

The PDE coefficients, μ and Σ, can be scalars or Symmetric Positive Definite (SPD) tensors. For the sake of generality in the exposition, let us assume that both coefficients are 3×3 SPD matrices of the form

$$\mu(\vec{x}) = \begin{bmatrix} \mu^1(\vec{x}) & \mu^4(\vec{x}) & \mu^5(\vec{x}) \\ \mu^4(\vec{x}) & \mu^2(\vec{x}) & \mu^6(\vec{x}) \\ \mu^5(\vec{x}) & \mu^6(\vec{x}) & \mu^3(\vec{x}) \end{bmatrix}, \ \Sigma(\vec{x}) = \begin{bmatrix} \sigma^1(\vec{x}) & \sigma^4(\vec{x}) & \sigma^5(\vec{x}) \\ \sigma^4(\vec{x}) & \sigma^2(\vec{x}) & \sigma^6(\vec{x}) \\ \sigma^5(\vec{x}) & \sigma^6(\vec{x}) & \sigma^3(\vec{x}) \end{bmatrix}, \tag{2.3}$$

where $\mu^l, \sigma^l : \Omega \to \mathbb{R}; \ l = 1, ..., 6$. Under these assumptions, these coefficients model the anisotropic and highly heterogeneous behavior of the medium in the geophysical problem that is considered. Since in practice these coefficients tend to vary over multiple spatial scales and several orders of magnitude, let us assume that the entries of these coefficients are piecewise smooth functions with

jump discontinuities at the material interfaces. These coefficients are referred as the *medium parameters* throughout this dissertation. The stated PDE system assumes International System Units and $e^{i\omega t}$ time dependence.

Note that taking the divergence of equation (2.1) leads to

$$\nabla \cdot \vec{B} = 0, \text{ in } \Omega, \tag{2.4}$$

which implies that $\vec{B}$ must be divergence free for every point in the domain. This condition is known as the Gauss's law for magnetic fields [58].

As shown in [68, 169], the system (2.1)-(2.2) is typically closed with the *natural boundary conditions* given by

$$\mu^{-1}(\vec{x})\vec{B}(\vec{x}) \times \vec{n} = \vec{0}, \quad \forall \vec{x} \in \partial\Omega, \tag{2.5}$$

or with the non-homogeneous Dirichlet boundary conditions given by

$$\vec{E}(\vec{x}) \times \vec{n} = \vec{E}_0(\vec{x}) \times \vec{n}, \quad \forall \vec{x} \in \partial\Omega, \tag{2.6}$$

were $\partial\Omega$ denotes the boundary of Ω, $\vec{n}$ denotes the unit outward-pointing normal vector to $\partial\Omega$, and $\vec{E}_0$ specifies the tangential components of $\vec{E}$ at $\partial\Omega$. However, more general boundary conditions can be imposed to the Maxwell's system (2.1)-(2.2) as discussed in [104, 169]. For the sake of simplicity in the exposition, the discussion is limited to the boundary conditions (2.5) and (2.6).

For realistic geophysical settings with highly heterogeneous medium parameters, the quasi-static Maxwell's equations do not have analytical solutions [169]. In such cases, a numerical solution is computed. The next section provides an overview of the mimetic finite volume discretization method, which is the discretization method I use in this dissertation to do so.

2.4 The Mimetic Finite Volume Discretization

In this section, I provide an overview of the mimetic finite volume discretization method (MFV). Full derivation details can be found in [68, 93–98]. Since the MFV method provides a conservative, consistent and stable discretization of the

Maxwell's equations introduced in Section 2.3, I use it as a building block to develop the multiscale and upscaling approaches proposed in this work. However, edge-based FE or FD discretization methods as the ones proposed in [104, 121, 131, 135, 149, 165], which also provide a conservative, consistent and stable discretization for Maxwell's equations, can be used as well.

The MFV is an extension of Yee's FD method ([178]) that constructs discrete curl, divergence and gradient operators satisfying discrete analogs of the main theorems of vector calculus involving such operators. For example, $\nabla \times (\nabla \phi) = \vec{0}$, where ϕ is a scalar potential, and $\nabla \cdot (\nabla \times \vec{A}) = 0$, where $\vec{A}$ is a vector potential. Therefore, the discrete differential operators obtained with MFV do not have spurious solutions and the divergence-free condition for the magnetic field (2.4) is automatically satisfied in the discrete setting. In addition, MFV models the correct behavior of the tangential and normal components of $\vec{E}$ and $\vec{B}$ through material interfaces (i.e., the tangential components of $\vec{E}$ and the normal components of $\vec{B}$ are continuous through material interfaces, and the normal components of $\vec{E}$ and the tangential components of $\vec{B}$ are discontinuous through material interfaces [169]). Due to these reasons, the discretization is called mimetic as it preserves (mimics) the underlying relevant mathematical and physical properties of the quasi-static Maxwell's equations. Furthermore, MFV leads to sparse and symmetric linear systems of equations and it can be implemented on general polygonal and polyhedral meshes [98].

Following the guidelines provided by Hyman and Shashkov ([93, 94]), the MFV method begins by considering the weak form of the Maxwell's system (2.1)-(2.2):

$$(\nabla \times \vec{E}, \vec{F}) + \iota \omega (\vec{B}, \vec{F}) \quad = \quad 0, \tag{2.7}$$

$$(\nabla \times \mu^{-1} \vec{B}, \vec{W}) - (\Sigma \vec{E}, \vec{W}) \quad = \quad (\vec{J_s}, \vec{W}), \tag{2.8}$$

where $\vec{F} \in \mathscr{H}(div; \Omega)$ and $\vec{W} \in \mathscr{H}(curl; \Omega)$ are arbitrary test functions; $\mathscr{H}(div; \Omega)$ and $\mathscr{H}(curl; \Omega)$ are the Hilbert spaces of square-integrable vector functions on Ω with square-integrable divergence and curl, respectively; and $(\cdot, \cdot)$ denotes the inner product given by $(\vec{P}, \vec{Q}) = \int_{\Omega} P^x \overline{Q^x} + P^y \overline{Q^y} + P^z \overline{Q^z} \, dV$. In particular, $\vec{E} \in \mathscr{H}(curl; \Omega)$ and $\vec{B} \in \mathscr{H}(div; \Omega)$. For a more detailed description of the arbitrary test functions $\vec{F}$ and $\vec{W}$ used here, the interested reader is referred to

[93, 94, 131].

As shown in [68], after integrating by parts the term $(\nabla \times \mu^{-1}\vec{B}, \vec{W})$ in equation (2.8) and applying the natural boundary conditions (2.5), the boundary term vanishes and equation (2.8) becomes

$$(\mu^{-1}\vec{B}, \nabla \times \vec{W}) - (\Sigma\vec{E}, \vec{W}) = (\vec{J}_s, \vec{W}).$$ (2.9)

The resulting weak system formed by equations (2.7) and (2.9) is more convenient to work with. It only requires the tangential components of $\vec{E}$ and $\vec{W}$ be differentiable, and eliminates the differentiability condition on the tangential components of $\vec{B}$, which may be discontinuous across material interfaces. Furthermore, the discretization of the anisotropic discontinuous coefficients, Σ and μ, will be done via the numerical approximation of their corresponding inner products; as we will see, this allows an adequate treatment in such cases.

Next, the method proceeds by numerically approximating the differential operators and the inner products in the weak system formed by equations (2.7) and (2.9). To elaborate further, let us first introduce some mathematical notation. For simplicity in the exposition, let us assume Ω to be a cuboid domain that is discretized with a staggered tensor mesh, $\mathcal{M}$. In particular, $\mathcal{M} = \cup_{i,j,k=1}^{n^x,n^y,n^z} \Omega_{i,j,k}^h$, where n^x, n^y and n^z are the number of cells along the x, y and z axis, respectively; and $\Omega_{i,j,k}^h$ denotes the (i,j,k)th cell. The lengths of $\Omega_{i,j,k}^h$ along the x, y and z axis are h_i^x, h_j^y and h_k^z, respectively. Let us number the cell center of $\Omega_{i,j,k}^h$ as (i,j,k), the x, y and z edges of $\Omega_{i,j,k}^h$ as $(i, j \pm \frac{1}{2}, k \pm \frac{1}{2})$, $(i \pm \frac{1}{2}, j, k \pm \frac{1}{2})$ and $(i \pm \frac{1}{2}, j \pm \frac{1}{2}, k)$, respectively; and the x, y and z faces of $\Omega_{i,j,k}^h$ as $(i \pm \frac{1}{2}, j, k)$, $(i, j \pm \frac{1}{2}, k)$ and $(i, j, k \pm \frac{1}{2})$, respectively. Let us discretize $\vec{E}$ and $\vec{J}_s$ on the edges, $\vec{B}$ on the faces, and the PDE coefficients μ and Σ at the cell centers. Figure 2.1 shows a control volume cell with the allocation of these variables. According to [58, 68], edge variables can be physically interpreted as (electric) fields, as they represent a (line) force moving on a path around a surface. Similarly, face variables can be physically interpreted as (magnetic) fluxes, as they represent a (magnetic) flux inwards or outwards the cell. The physical meaning of such variables explains the choice of discretization location. The corresponding grid functions on $\mathcal{M}$ for the variables mentioned before are denoted as $\mathbf{e}$, $\mathbf{j}_s$, $\mathbf{b}$, $\boldsymbol{\mu}$ and $\boldsymbol{\Sigma}$, respectively.
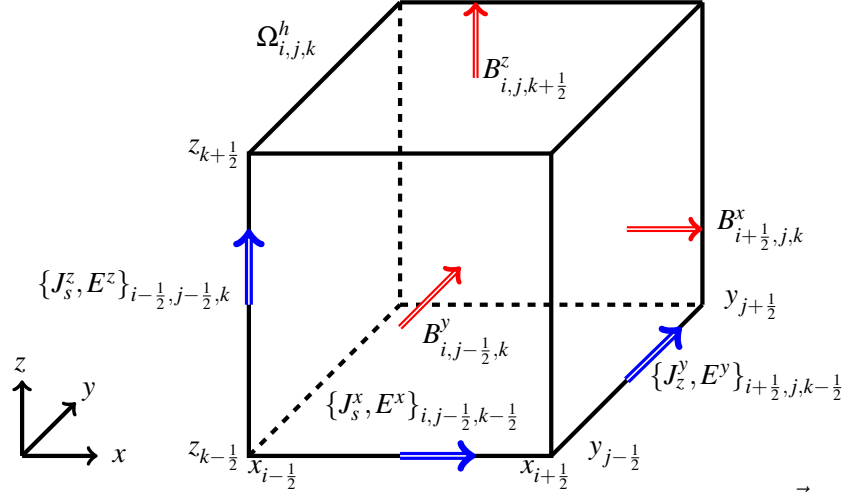
Figure 2.1: Control volume cell showing the staggered discretization for $\vec{E}$ and $\vec{J}_s$ on its edges, $\vec{B}$ on its faces, and the medium parameters μ and Σ at the cell centers.

To discretize the curl operator on each of the faces of the cell $\Omega_{i,j,k}^h$, let us use its integral form as given in [145], which is convenient as it provides a geometrical, coordinate-free expression for the definition of this operator. That is,

$$(\nabla \times \vec{E}) \cdot \vec{n}_S = \lim_{A_S \to 0} \left(\frac{1}{A_S} \int_S \nabla \times \vec{E} \cdot dS \right) = \lim_{A_S \to 0} \left(\frac{1}{A_S} \oint_{\partial S} \vec{E} \cdot dl \right), \qquad (2.10)$$

where S denotes a face of $\Omega_{i,j,k}^h$, $\vec{n}_S$ denotes the outward unit normal vector to S, ∂S denotes the boundary of S, and A_S denotes the area of S. In the above expression, the Stoke's theorem was applied ([145]).

To compute the integrals in (2.10), let us use the midpoint quadrature rule ([6]). For example, the discretization for the $(i + \frac{1}{2}, j, k)$th face, which is denoted as $S_{i+\frac{1}{2},j,k}$, can be written as

$$(\nabla \times \vec{E}) \cdot \vec{n}_{S_{i+\frac{1}{2},j,k}} \approx \frac{-h_j^y \left(E_{i+\frac{1}{2},j,k+\frac{1}{2}}^y - E_{i+\frac{1}{2},j,k-\frac{1}{2}}^y \right) + h_k^z \left(E_{i+\frac{1}{2},j+\frac{1}{2},k}^z - E_{i+\frac{1}{2},j-\frac{1}{2},k}^z \right)}{h_j^y h_k^z}.$$

$$(2.11)$$

The discretization for the rest of the faces of $\Omega_{i,j,k}^h$ can be done in a similar way.

20

The above computation is performed for every cell and its corresponding faces in the staggered mesh $\mathcal{M}$. The result can be expressed in matrix form as follows

$$\nabla \times \vec{E} \approx \mathbf{CURL\,e} = \mathbf{S}^{-1}\mathbf{CL\,e}, \qquad (2.12)$$

where $\mathbf{S}$ is a diagonal matrix that contains the area of each face in our mesh, $\mathbf{L}$ is a diagonal matrix that contains the length of each edge in our mesh, and $\mathbf{C}$ is a matrix that contains the values 0 and ± 1 that indicates the mesh connectivity (i.e., it encodes the signs in equation (2.11)).

The discretization of the divergence and gradient operators can be done in a similar manner using their corresponding geometrical, coordinate-free definition (as given in [145]). The interested reader is referred to [68, 94, 96] for more details on how to do so. In such references, the authors demonstrate that the discrete operators obtained in this way satisfy that

$$\mathbf{CURL\,GRAD} = \mathbf{0}_M, \quad \mathbf{DIV\,CURL} = \mathbf{0}_M, \qquad (2.13)$$

where $\mathbf{GRAD}$ denotes the discrete gradient operator, $\mathbf{DIV}$ denotes the discrete divergence operator, and $\mathbf{0}_M$ is a matrix with all entries equal to zero. Furthermore, they demonstrate that $\mathbf{GRAD}$ spans the non-trivial null space of $\mathbf{CURL}$. These discrete relationships are known as the *mimetic properties* of the discrete operators.

To complete the discretization procedure, we need to approximate the inner products $(\Sigma\vec{E}, \vec{W})$, $(\mu^{-1}\vec{B}, \nabla \times \vec{W})$, $(\vec{J}_s, \vec{W})$ and $(\vec{B}, \vec{F})$. As we will see, the approximation of $(\nabla \times \vec{E}, \vec{F})$ will be done in an analogous way as the approximation of $(\vec{B}, \vec{F})$. We continue to follow Hyman and Shashkov ([93, 95–97]), and use low-order quadrature formulas to do so. One of the main differences between MFV and an edge-based FE discretization for Maxwell's equations ([104, 131]) is that MFV uses low-order quadrature formulas (e.g. midpoint or trapezoidal rules) for the numerical integration of the corresponding inner products, whereas FE uses Gauss numerical integration rules.

First, let us consider the approximation of $(\Sigma\vec{E}, \vec{W})$. Recall that the x, y and z components of $\vec{E}$ and $\vec{W}$ are discretized on the edges and that Σ is discretized at

the cell center of each cell (Figure 2.1), which implies that Σ is considered to take a constant value within each cell. Since Σ is a SPD matrix of the form (2.3), the computation of the integrand $\Sigma \vec{E} \cdot \vec{W}$ involves cross-term products of the tangential components of $\vec{E}$ and $\vec{W}$ that are not discretized at the same location; thus no low-order quadrature formulas (e.g. midpoint or trapezoidal rules) can be applied in this case. To overcome this problem, one first projects the tangential components of $\vec{E}$ and $\vec{W}$ to the nearest node in the cell; then one computes $\Sigma \vec{E} \cdot \vec{W}$. This process is referred to as nearest-neighbor interpolation ([68]) and it is illustrated in Figure 2.2(a). After applying this process, one obtains an approximation to $(\Sigma \vec{E}, \vec{W})$ as follows

$$\int_\Omega \Sigma \vec{E} \cdot \vec{W} \; dV \approx \mathbf{w}^\top \left(\frac{1}{8} \sum_{n=1}^{8} \mathbf{P}_n^{\mathbf{e}\top} \mathbf{V}^{\frac{1}{2}} \mathbf{M}(\boldsymbol{\Sigma}) \mathbf{V}^{\frac{1}{2}} \mathbf{P}_n^{\mathbf{e}} \right) \mathbf{e} = \mathbf{w}^\top \mathbf{M}_\mathbf{e}(\boldsymbol{\Sigma}) \mathbf{e}, \qquad (2.14)$$

where $\mathbf{V}$ is a diagonal matrix with the volume of each cell in the mesh, $\mathbf{P}_n^\mathbf{e}$, $n = 1, \ldots, 8$, are the matrices that project the three adjacent components of the electric field to the nth node of each cell, and $\mathbf{M}(\boldsymbol{\Sigma})$ is given by

$$\mathbf{M}(\boldsymbol{\Sigma}) = \begin{pmatrix} \mathrm{diag}\,(\boldsymbol{\sigma}^1) & \mathrm{diag}\,(\boldsymbol{\sigma}^4) & \mathrm{diag}\,(\boldsymbol{\sigma}^5) \\ \mathrm{diag}\,(\boldsymbol{\sigma}^4) & \mathrm{diag}\,(\boldsymbol{\sigma}^2) & \mathrm{diag}\,(\boldsymbol{\sigma}^6) \\ \mathrm{diag}\,(\boldsymbol{\sigma}^5) & \mathrm{diag}\,(\boldsymbol{\sigma}^6) & \mathrm{diag}\,(\boldsymbol{\sigma}^3) \end{pmatrix}, \qquad (2.15)$$

where each $\mathrm{diag}\,(\boldsymbol{\sigma}^i)$ represents a diagonal matrix containing the grid function of $\boldsymbol{\sigma}^i$; $i = 1, ..., 6$, respectively. Let us define $\mathbf{M}_\mathbf{e}(\boldsymbol{\Sigma})$ in (2.14) as the edge mass matrix. Note that when Σ is a diagonal matrix, the edge mass matrices is identical to the one obtained by discretizing $(\Sigma \vec{E}, \vec{W})$ using low-order quadrature formulas [70]. The described discretization method naturally extends the use of Yee meshes (i.e., staggered tensor meshes) to the anisotropic case. Its advantage is that it only requires integration over one cell at a time; the averaging (2.14) is a result of the integration over the domain. This is similar to FE methods, where averaging is performed implicitly through the assembly of the mass matrix [104, 131].

Next, let us approximate $(\mu^{-1}\vec{B}, \nabla \times \vec{W})$. Since μ is a SPD matrix of the form (2.3), computing the integrand $\mu^{-1}\vec{B} \cdot \nabla \times \vec{W}$ leads to a similar problem as
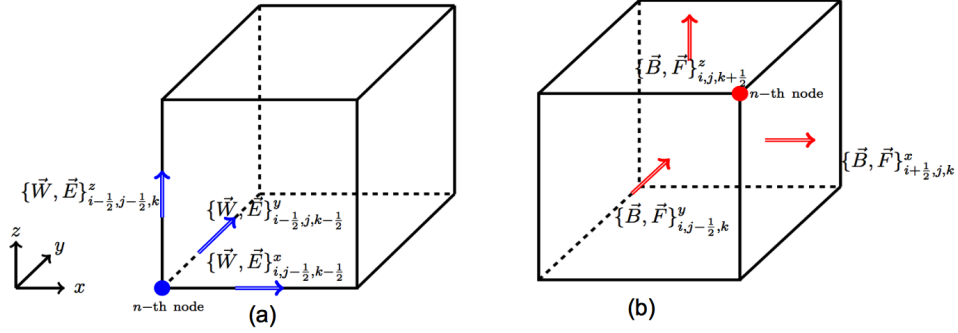
Figure 2.2: Schematic representation of the nearest-neighbor interpolation process for approximating (a) the edge inner product $(\Sigma\vec{E},\vec{W})$ and (b) the face inner product $(\mu^{-1}\vec{B},\vec{F})$ in the cuboid cell $\Omega_{i,j,k}^h$.

the one described before for the numerical integration of $(\Sigma\vec{E},\vec{W})$. In this case, one uses the nearest-neighbor interpolation method on the faces of $\mathcal{M}$ and the discrete expression of the curl operator obtained in (2.12) in order to approximate $(\mu^{-1}\vec{B},\nabla\times\vec{W})$, which leads to

$$
\int_{\Omega}\mu^{-1}\vec{B}\cdot(\nabla\times\vec{W})dV \approx \mathbf{w}^{\top}\mathbf{CURL}^{\top}\left(\frac{1}{8}\sum_{n=1}^{8}\mathbf{P}_n^{\mathsf{f}\,\top}\mathbf{V}^{\frac{1}{2}}\mathbf{M}(\boldsymbol{\mu}^{-1})\mathbf{V}^{\frac{1}{2}}\mathbf{P}_n^{\mathsf{f}}\right)\mathbf{b}
$$
$$
= \mathbf{w}^{\top}\mathbf{CURL}^{\top}\mathbf{M_f}(\boldsymbol{\mu}^{-1})\mathbf{b}, \tag{2.16}
$$

where $\mathbf{P}_n^{\mathsf{f}}$; $n=1,...,8$ are the matrices that project the three adjacent components of the magnetic flux to the nth node of each cell (see illustration of this process in Figure 2.2(b)), $\mathbf{V}$ is defined as before in (2.14), and $\mathbf{M}(\boldsymbol{\mu}^{-1})$ is given by

$$
\mathbf{M}(\boldsymbol{\mu}^{-1}) = \begin{pmatrix} \mathrm{diag}\,(\boldsymbol{\mu}^{-1^{1}}) & \mathrm{diag}\,(\boldsymbol{\mu}^{-1^{4}}) & \mathrm{diag}\,(\boldsymbol{\mu}^{-1^{5}}) \\ \mathrm{diag}\,(\boldsymbol{\mu}^{-1^{4}}) & \mathrm{diag}\,(\boldsymbol{\mu}^{-1^{2}}) & \mathrm{diag}\,(\boldsymbol{\mu}^{-1^{6}}) \\ \mathrm{diag}\,(\boldsymbol{\mu}^{-1^{5}}) & \mathrm{diag}\,(\boldsymbol{\mu}^{-1^{6}}) & \mathrm{diag}\,(\boldsymbol{\mu}^{-1^{3}}) \end{pmatrix}, \tag{2.17}
$$

where each $\mathrm{diag}\,(\boldsymbol{\mu}^{-1^{i}})$ represents a diagonal matrix containing the grid function of the ith entrance of the inverse of the matrix μ given by (2.3), denoted as $\mu^{-1^{i}}$; $i=1,...,6$, respectively. $\mathbf{M_f}(\boldsymbol{\mu}^{-1})$ in (2.16) is defined as the face mass matrix.

Next, let us approximate $(\vec{J}_s, \vec{W})$. Since the three tangential components of the integrand $\vec{J}_s \cdot \vec{W}$ are placed at the same location for every cell of the mesh (i.e., at the edges), one uses a combination of the trapezoidal and midpoint quadrature rules ([6]) to approximate this inner product, which leads to

$$\int_\Omega \vec{J}_s \cdot \vec{W} \, dV \approx \mathbf{w}^\top \left(\mathrm{diag}\, (\mathbf{A}_\mathsf{e}^\mathsf{cc})^\top \mathbf{v} \right) \mathbf{j}_s, \tag{2.18}$$

where $\mathbf{A}_\mathsf{e}^\mathsf{cc}$ is a sparse matrix that averages edge variables into the cell centers and it contains only $\frac{1}{4}$ where the edge variables are averaged ([68]), and $\mathbf{v}$ is the vector of cell volumes arising from applying the quadrature rules on each cell of the mesh.

Next, let us approximate $(\vec{B}, \vec{F})$. Since the three normal components of the integrand $\vec{B} \cdot \vec{F}$ are placed at the same location for every cell of the mesh (i.e., at the faces), one uses the midpoint quadrature rule to approximate this inner product, which leads to

$$\int_\Omega \vec{B} \cdot \vec{F} \, dV \approx \mathbf{f}^\top \left(\mathrm{diag}\, (\mathbf{A}_\mathsf{f}^\mathsf{cc})^\top \mathbf{v} \right) \mathbf{b}, \tag{2.19}$$

where $\mathbf{A}_\mathsf{f}^\mathsf{cc}$ is a sparse matrix that averages face variables into the cell centers and it contains only $\frac{1}{2}$ where the face variables are averaged [68], and $\mathbf{v}$ is defined as before in (2.18). The approximation of the inner product $(\nabla \times \vec{E}, \vec{F})$ can be done in an analogous way as for $(\vec{B}, \vec{F})$ and also uses the discrete expression of the curl operator that was obtained in (2.12). Doing so results in the following expression

$$\int_\Omega \nabla \times \vec{E} \cdot \vec{F} \, dV \approx \mathbf{f}^\top \left(\mathrm{diag}\, (\mathbf{A}_\mathsf{f}^\mathsf{cc})^\top \mathbf{v} \right) \mathbf{CURL}\, \mathbf{e}. \tag{2.20}$$

Combining equations (2.14), (2.16), (2.18), (2.19), (2.20) and applying some standard mathematical manipulations, one obtains the following discrete analog to the quasi-static Maxwell's equations

$$\mathbf{CURL}\, \mathbf{e} + \iota \omega \mathbf{b} \;\; = \;\; \mathbf{0}, \tag{2.21}$$

$$\mathbf{CURL}^\top \mathbf{M_f}(\boldsymbol{\mu}^{-1}) \mathbf{b} - \mathbf{M_e}(\boldsymbol{\Sigma}) \mathbf{e} \;\; = \;\; \mathrm{diag}\, \left((\mathbf{A}_\mathsf{e}^\mathsf{cc})^\top \mathbf{v} \right) \mathbf{j}_s =: \mathbf{q}, \tag{2.22}$$

where $\mathbf{0}$ is a column vector with all its entries equal to zero. Now, from equation

24

(2.21), one can obtain a discrete analog to the magnetic flux as follows

$$\mathbf{b} = -\frac{1}{\iota\omega}\mathbf{CURL}\,\mathbf{e}. \tag{2.23}$$

Note that multiplying (2.23) times **DIV** and using (2.13) implies that

$$\mathbf{DIV}\,\mathbf{b} = \mathbf{0}; \tag{2.24}$$

that is, one obtains the discrete analog to Gauss's law for the magnetic field (2.4).

Now, substituting (2.23) into (2.22) one obtains the following system of linear equations in terms of **e**

$$\mathbf{A}(\mathbf{\Sigma})\mathbf{e} = -\iota\omega\mathbf{q}, \tag{2.25}$$

where

$$\mathbf{A}(\mathbf{\Sigma}) = \mathbf{CURL}^{\top}\mathbf{M_f}(\boldsymbol{\mu}^{-1})\mathbf{CURL} + \iota\omega\mathbf{M_e}(\mathbf{\Sigma}). \tag{2.26}$$

The matrix $\mathbf{A}(\mathbf{\Sigma})$ is complex, sparse, symmetric, and, in practice, it tends to be severely ill-conditioned. Section 2.5 provides an overview of the direct and iterative solvers that can be used to solve this system.

As shown in [68], to impose the non-homogeneous Dirichlet boundary conditions (2.6), which imply the values of the tangential components of the electric field at the boundary are known, the matrix $\mathbf{A}(\mathbf{\Sigma})$ and the vectors **e** and **q** from equation (2.25) are reordered into interior edges (ie) and boundary edges (be). Thus, the system to be solved in terms of the unknown $\mathbf{e}^{\text{ie}}$ is

$$\mathbf{A}^{\text{ie,ie}}\mathbf{e}^{\text{ie}} = -\left(\iota\omega\mathbf{q}^{\text{ie}} + \mathbf{A}^{\text{ie,be}}\mathbf{e}^{\text{be}}\right), \tag{2.27}$$

where $\mathbf{A}^{\text{ie,ie}}$, $\mathbf{A}^{\text{ie,be}}$, and $\mathbf{q}^{\text{ie}}$ represent the corresponding partitions of the matrix $\mathbf{A}(\mathbf{\Sigma})$ and the vector **q** of the system (2.25), $\mathbf{e}^{\text{ie}}$ is the discretized electric field at the interior edges, and $\mathbf{e}^{\text{be}}$ is the discretized electric field at the boundary.

As shown in [68, 96], the MFV method is second order accurate assuming an orthogonal mesh and that the PDE coefficients are smooth or piecewise constant, which is our case. The works in [124, 131] propose discretization schemes for Maxwell's equations with higher orders of accuracy. However, these schemes are more complicated and more computationally expensive to solve. The order of

accuracy provided by MFV is sufficient for the type of large-scale geophysical EM simulations we are interested in this study.

The ideas presented in this section have been extended to OcTree meshes (for details see [72, 86]) and to logically orthogonal meshes (for details see [68]). Let us finish this section by providing a mimetic discrete approximation for the electric current density $\vec{J}$, as it will be used later in Chapter 3. The continuous form of Ohm's law ([169]) states that

$$\vec{J} = \Sigma \vec{E}. \tag{2.28}$$

In order to obtain a discrete analog of the electric current density, $\mathbf{j}$, one first interpolates the tangential components of $\vec{E}$ to the cell centers of our mesh. Next, one performs a point-wise multiplication of such components with the conductivity to obtain $\vec{J}$ at the cell centers. Finally, one interpolates the three components of $\vec{J}$ to its normal directions (i.e., to the cell faces). This procedure results in a conservative interpolation for $\vec{J}$ that preserves its continuous properties in the discrete setting. The grid function of $\vec{J}$ is denoted as $\mathbf{j}$, which is given by

$$\mathbf{j} = \mathbf{A}_{\text{cc}}^{\text{f}} \mathbf{M_e}(\mathbf{\Sigma}) \mathbf{A}_{\text{e}}^{\text{cc}} \mathbf{e}, \tag{2.29}$$

where $\mathbf{A}_{\text{e}}^{\text{cc}}$ represents the averaging matrix taking information from edges to cell centers as defined in (2.18), $\mathbf{M_e}(\mathbf{\Sigma})$ is given by (2.15) and $\mathbf{A}_{\text{cc}}^{\text{f}}$ is a sparse matrix that averages cell-center variables into the faces and it contains only $\frac{1}{2}$ where the cell-center variables are averaged ([68]).

2.5 Solvers

This section provides an overview of the direct and iterative solvers used to solve the large, complex, symmetric, and sparse linear system of algebraic equations (2.25) that result from the MFV discretization of the quasi-static Maxwell's equations.

Before discussing the solver alternatives for the system of equations (2.25), a brief discussion about the conditioning of such system of equations is given. A severe ill-conditioning problem can arise in practice when solving the system

of equations (2.25) for the cases where the EM survey configuration considers very low frequencies, i.e., $\omega \approx 0$; and/or when the geophysical setting considers very low conductivity values (e.g. when the setting considers air, whose electrical conductivity is 0 S/m, but for simulation purposes this conductivity value is typically assumed to be 10^{-8} S/m). For such cases, the matrix system (2.26) is close to be singular and its condition number is expected to be quite large.

The ill-conditioning of the system matrix (2.26) for the cases described above can be primarily explained by the fact that the discrete curl operator obtained using the MFV discretization has a non-trivial null space, namely the discrete gradient operator (see equation (2.13)). This feature is expected from using a mimetic method to discretize the quasi-static Maxwell's system. That is, the discrete system is expected to inherit the near-singularity of the underlying continuous Maxwell's system [5, 68].

More generally, the conditioning of the system matrix (2.26) can be explained by analyzing separately its two parts. The work in [40, 68] shows that the eigenvalues of the term $\mathbf{M_e}(\boldsymbol{\Sigma})$ in equation (2.26) are bounded by the minimum and maximum values (assuming volume scaling) of the electrical conductivity considered in the geophysical setting. On the other hand, the largest eigenvalue of the term $\mathbf{CURL}^\top \mathbf{M_f}(\boldsymbol{\mu}^{-1}) \mathbf{CURL}$ is not bounded. Such term comes from the MFV discretization of the differential operator $\nabla \times (\mu^{-1} \nabla \times)$. As one refines the mesh, its largest eigenvalue goes to infinity, while its smallest eigenvalue is zero (due to the non-trivial null space of the curl operator) (cf. [68]).

Once the conditioning of the system (2.25) has been discussed, lets discuss the solver alternatives for solving such system.

Iterative solvers are the natural choice to solve the large, sparse and symmetric system of equations (2.25). They lead to substantial savings on time and memory usage, as they use optimized (sparse) matrix-vector product multiplications at each iteration and do not require to store the matrix of the system [146]. The literature suggests using BiCGSTAB, MINRES or GMRES solvers for the system (2.25) [68, 134, 146]. Such solvers can experience extremely slow convergence rates or non-convergence at all when the system (2.25) is extremely ill-conditioned (e.g. when simulation setting considers very low frequencies and very low conductivity values) [75]. For such cases, the literature suggests that we

first reformulate the PDE model to obtain a better conditioned system. And second, that we precondition the system of equations obtained from the reformulation of the problem. Doing so results in faster convergence rates to the solution (e.g. [5, 12, 66, 68, 70, 100, 115, 128, 135, 149, 157, 168, 172]). Below, we briefly discuss these two complementary steps:

1. The first step is to reformulate the Maxwell's system (2.1)-(2.2) using the Helmholtz decomposition together with a Coulomb gauge condition such that, after applying an adequate discretization method, the resulting matrix is better conditioned. The Helmholtz decomposition is a fundamental theorem of vector calculus that expresses the electric field as the sum of a curl-free potential field and a divergence-free potential field [145]. This approach can lead to a saddle point system of equations, which can be solved leveraging its special structure (see [63, 64] and references within). To avoid solving the saddle point system, further algebraic manipulations can be done to the reformulated system in order to obtain a much better conditioned system to be solved (see [68, 152] and references within).

2. After the issues associated with the null space of the curl have been taken care of by reformulating the PDE system as discussed in step 1, the second second step is to construct a preconditioner matrix. Such preconditioner should transform the reformulated system to be solved into another system with more favorable properties, such as a clustered spectrum, for iterative solution [15, 146]. The literature suggests the use of the following preconditioners: Jacobi, Symmetric Gauss-Seidel, Incomplete LU and SSOR [68, 100, 134]. As discussed in [68], these preconditioners are easy to apply and work well for a moderate-sized system, if the system is not poorly conditioned. For much larger ill-conditioned systems, more sophisticated preconditioners are needed, such as multigrid [27, 164]. Research on multigrid solvers and preconditioners for Maxwell's equations can be found in [4, 83, 84, 105, 133].

Although using iterative methods (complemented with a reformulation of the PDE model as described above) is one of the most efficient ways currently used to tackle EM forward simulations, using iterative methods as part of an EM inversion

routine can suffer a major drawback: the system needs to be solved multiple times for the number of sources and the different frequencies considered in the geophysical EM survey configuration [68], which can be in the order of thousands or even millions (e.g. an airborne survey) [144]. In such cases, being able to use direct solvers to decompose the matrix of the system of equations is the most cost-effective way to overcome this issue [43, 68]. However, a matrix factorization requires us to be able to store the matrix. This requirement is what motivates my interest on being able to reduce the size of the system of equations, so that direct methods can be used to solve the system. Let us discuss next the options for direct solvers for the linear system (2.25).

Direct solvers are based on a version of Gaussian elimination to compute a LU factorization [43]. Since the factors are stored, these methods require to have enough CPU memory available. These type of solvers are known to produce more reliable and robust solutions than iterative solvers. The research in [149] pointed out that for settings that use frequencies and conductivities very close to zero, the system is severely ill-conditioned and the PDE problem may benefit from being first reformulated as discussed previously.

For 1D problems and most 2D problems direct factorization methods are available on most packages and can be used without specialized computing resources. However, for 3D problems it is not always possible to factorize the system without specialized software and hardware. There are some parallel direct solvers packages available, such as MUMPS [3], SuperLU [116], STRUMPACK [62], PARDISO [148], WSMP [65], that can solve problems with millions of unknowns. These packages use optimized memory saving strategies and its matrix factorization is done in parallel architectures on powerful hardware, large-scale problems can be handled with direct solvers. My research group has used the solver MUMPS for several years with satisfactory results, thus the simulation results presented in this dissertation use such direct solver.

2.6   Literature Review

This section reviews some of the most successful upscaling and multiscale methods, developed for single-phase flow in porous media problems, that are used

as a building block to develop their counterparts for application to geophysical EM modeling. In addition, it discusses some of the existing connections between multiscale and multigrid methods.

Upscaling and multiscale methods have been extensively studied also for problems in the fields of materials science, computational mechanics, petroleum engineering and computational water resources [51, 60]. All of these problems share the same underlying mathematical model: a Poisson-type equation (i.e., a scalar, linear and elliptic PDE). Since the amount of research for both upscaling and multiscale methods for (linear) elliptic problems is quite extensive, the following sections only discuss the closest investigations to the upscaling and multiscale approaches used in this dissertation. Fewer research along these lines has been done for the quasi-static Maxwell's equations discussed in Section 2.3.

2.6.1 Upscaling Methods

Upscaling or homogenization methods seek to derive a coarse-scale PDE and to pre-compute its coefficients from a given fine-scale PDE model with highly discontinuous coefficients (see [49, 56, 60, 111, 143, 147, 175] for reviews). The coarse-scale PDE coefficients are referred in the literature as upscaled, equivalent, averaged, homogenized or effective coefficients [122]. In practice, the setup for an upscaling method assumes a fine mesh, which accurately discretizes the fine-scale PDE, and a much coarser mesh, which is overlaid on top of the fine mesh, where the coarse-scale PDE is ultimately solved. The computation of the upscaled coefficients is done for every coarse-mesh cell. Once the upscaled coefficients are computed, one can use them to solve the coarse-scale PDE on a much coarser mesh using fewer computational resources.

Using methods from asymptotic homogenization theory ([14]), it was proved that for a Poisson's equation that satisfies certain conditions (e.g. scale separation and periodic boundary conditions), the fine- and coarse-scale equations are of the same form, except that the fine-scale coefficient is replaced by the upscaled one (see [51, 122] for details). In general, by using similar analysis techniques to study fine-scale heterogeneous structures can result in full tensor upscaled coefficients (see [119, 163] and references within). For example, the investigation in [103]

demonstrates that upscaling two-scale periodic media can result in a full SPD tensor upscaled coefficient, even though the fine-scale coefficient is a scalar.

Although technically replacing the fine-scale Poisson's equation with its analogous coarse-scale equation is only valid under very particular conditions, the literature provides numerical evidence that justifies such replacement in practice (cf. [49, 122]). In light of this knowledge, when using upscaling methods to solve flow in porous media problems in practice, the focus goes in computing the upscaled coefficient.

The research works in [102, 110, 173, 174] propose similar proofs (under similar restrictive assumptions) for the case of the quasi-static Maxwell's equations in the frequency domain. Based on these studies, in this work, I also assume that the fine- and coarse-scale Maxwell's equations are of the same form and I will focus on computing the upscaled coefficients of this mathematical model.

There is extensive research on how to compute accurate upscaled coefficients for flow in porous media problems. Some of the most popular procedures have the potential to be extended for application to geophysical EM problems, such as analytical upscaling, flow-based upscaling, and output least-squares upscaling.

Analytical Upscaling

One of the simplest ways to compute upscaled coefficients is using an analytical procedure. Analytical procedures seek to derive closed-form expressions for the upscaled coefficients using averaging principles. It is often the case that an upscaled coefficient is computed by using simple averages of the fine-scale coefficient information inside the target coarse-mesh cell. See [49, 56, 60, 141, 175] for reviews of analytical upscaling procedures.

Analytical procedures work well when the fine-scale coefficient varies over a fixed number of distinctive length scales and it has a particular structure (e.g. a layered medium or a medium with a small correlation length). Similar closed-form expressions for the upscaled coefficients can be obtained using asymptotic homogenization theory or effective medium theory. Along these two lines, the works in [28, 102, 103, 110] and in [18, 127, 151, 163] propose analytical procedures to compute the upscaled electrical conductivity in the context of EM problems,

respectively.

Analytical upscaling procedures have the advantage of being simple, very cheap to compute, and accurate in the (limited) cases where the assumptions are satisfied; however, their underlying fundamental limitation is that these procedures are quite inaccurate for arbitrary fine-scale coefficient variations, which appear most of the time in practice [49, 56, 122, 132, 175].

Flow-based Upscaling

A more general and accurate, but more expensive, way to compute upscaled coefficients for flow in porous media problems is to use a so-called flow-based procedure (cf. [45, 49, 170]). This method has its origins in early 1960s. Currently, this is one of the most popular procedures to perform upscaling in the field of petroleum engineering.

The goal of a flow-based upscaling procedure is to construct an upscaled coefficient (e.g. permeability) for every coarse-mesh cell by averaging fine-scale flow information within the target coarse-mesh cell. Such fine-scale flow is computed by numerically solving a set of local diffusion (steady-state elliptic) boundary-value problems (without source term) for a given set of boundary conditions on the target cell. The upscaled coefficient is determined such that the total flow across the coarse cell is preserved as much as possible. These types of procedures can produce full-tensor upscaled coefficients.

Flow-based procedures can be classified as local, extended, or global methods, depending on the size of the computational region used to determine the upscaled coefficient (see [49, 56, 60, 175] for reviews and discussion). With a local upscaling method, the upscaled permeability is computed using only fine-mesh information within the target coarse cell. For an extended method, the upscaled permeability is computed using fine-mesh information within an extended coarse-mesh cell, which includes the target coarse cell and a neighborhood of fine-mesh cells around the target coarse cell. Extended methods are more accurate than local methods mainly because they allow larger heterogeneous connectivities in the target cell to be represented more accurately as well as they mitigate the effect of the chosen local boundary conditions, but they are also computationally more

expensive. In a global method, the upscaled permeability for a target coarse cell is computed using the entire fine-mesh model. Global procedures are significantly more accurate as they can better capture the connectivity effects of the permeability throughout the domain, and they do not require local boundary conditions. Global upscaling procedures can be quite computationally expensive for large-scale problems as they require to solve the fine-mesh PDE problem more than once. For very large-scale 3D problems, they are still not practical.

With a proper setup, flow-based procedures can drastically reduce the cost of a fluid flow simulation, while providing an accuracy comparable to the one obtained with traditional fine-mesh discretization techniques, such as FE or FV (see [35, 36, 48, 49, 60, 61, 175] for details). However, local and extended flow-based procedures can lack accuracy when the local boundary conditions chosen are not properly chosen, and when heterogeneous connectivities have a spatial extent/scale that is larger than the target coarse cell.

To overcome the lack of accuracy in local and extended flow-based procedures, global procedures can be combined with local or extended flow-based methods. Such combined procedures are referred in the literature as local-global upscaling methods. The investigations in [35–37, 49, 61] are examples of some local-global methods that show how global upscaling procedures can be performed using a simplified version of the fine-scale PDE in order to obtain a better set of boundary conditions to setup a local or an extended upscaling procedure.

A significant amount of research has been developed in order to improve the flow-based upscaling procedures. Some of the most important research directions to do so are: a) testing different boundary conditions for the set of local diffusions problems that need to be solved for 2D and 3D problems, b) understanding how to better capture full-tensor effects derived from the upscaling procedure c) investigating how the combination of different upscaling procedures perform for different problems, d) proposing flow-based coarse-mesh generation methods and investigating the effect of this type of mesh setup in the resulting upscaled coefficients, and e) assessing the quality of the resulting upscaled permeability model. See [35, 36, 49, 50, 60, 61, 112] and references within for details and discussion regarding these topics.

The Output Least-Squares Upscaling

Among the various existing global upscaling formulations for flow in porous media problems, there is one that can be generalized to solve upscaling problems in different contexts: the output least-squares global method (OLS) (for reviews see [35, 49, 56, 175]). The OLS method can be considered as a global procedure as it computes upscaled coefficients by performing computations on the entire fine-mesh model.

The OLS method was introduced in early 2000s in the studies by [85, 136], where the authors propose a least-squares formulation for the upscaling problem. All the upscaled permeabilities are computed at once by minimizing the regularized least-squares difference between the pressure and the velocity fields generated using the fine and coarse-scale pressure equations. These studies only provided examples for constructing scalar upscaled coefficients for 2D problems with promising results. However, the OLS method is quite expensive to perform as the fine-mesh problem needs to resolved several times.

A least-squares formulation can be customized to compute either isotropic or fully anisotropic upscaled coefficients, depending on the definition of the objective function and the purpose of the simulation. Due to the flexibility and generality that this formulation offers, I extend and adapt it to solve geophysical EM problems in Chapter 3.

2.6.2 Multiscale Finite Element and Finite Volume Methods

There is a considerable body of research proposing multiscale approaches for problems with features at multiple length scales. Most of the work has been developed for flow in porous media problems. Among the most popular methods are the FE heterogeneous multiscale method [1, 171], the variational multiscale method [92], the generalized FE multiscale method [9–11], and the multiscale FE/FV methods [51, 89, 101]. The book in [51] provides a comprehensive review on this topic.

In this dissertation, I focus on the multiscale FE/FV methods develop for linear elliptic problems originally proposed by [74, 89, 101]. This type of multiscale methods have been successful in reducing the size and cost of the computation while

producing accurate solutions similar to that obtained with FE or FV discretization schemes on a fine mesh.

Multiscale FE/FV methods belong to the family of projection-based model reduction methods, where the fine-mesh system resulting from the discretization of the PDE model is projected onto a reduced subspace [51, 89]. Projected-based methods approximate the unknown physical responses using a basis of reduced dimension and project the governing PDE onto a suitably defined low-dimensional subspace [13]. The setup for these method assumes a fine mesh, which accurately discretizes the fine-scale PDE, and a much coarser mesh, which is overlaid on top of the fine mesh, where the problem is ultimately solved. Multiscale FE/FV methods construct multiscale basis functions for every coarse-mesh cell. The multiscale basis functions are computed by solving sets of local (elliptic) boundary-value problems. This process ensures that the basis captures the fine-scale variations of the PDE coefficients. A global variational formulation couples these basis functions to provide an accurate coarse-mesh solution to the problem.

According to [51], the multiscale FE method was born in early 1980s from the work in [9, 10], where the authors extended the Galerkin FE method for linear steady-state elliptic problems by constructing multiscale basis functions that depend on a particular type of multiscale coefficient. By early 1990s, the investigations in [89, 90] generalized the construction of multiscale basis functions for arbitrary coefficients. In particular, these investigations pointed out that the accuracy of the method strongly depends on the local boundary conditions chosen to construct the multiscale basis functions in the target coarse cell and they proposed oversampling techniques to solve the related accuracy issues. By early 2000s, multiscale FE methods were extended to non-linear, time-dependent (elliptic and parabolic) problems and various other global variational formulations to couple the multiscale basis functions were proposed (see [51] and reference within). During this time, the investigations in [79, 81, 101, 160] proposed multiscale FV methods, where a FV global formulation is used and the multiscale basis functions are computed by discretizing local boundary-value problems in a staggered mesh (as opposed to a nodal mesh as in multiscale FE). By doing so, the multiscale FV method is able to produce mass-conservative, coarse-mesh solutions.

Since early 2010s, some of the most important research directions in the multiscale FE/FV community have been: a) extending the range of applicability of these methods to simulate other physical phenomena, b) analyzing error convergence and improving the approximation properties of the method for different settings, c) generalizing the method by using more basis functions and improving oversampling techniques, d) developing multilevel multiscale methods as well as designing efficient parallel implementations, and e) developing hybrid multiscale methods using ideas from upscaling techniques (see [39, 50–52, 82, 114] for discussion and details on these topics).

Contrary to upscaling methods, which have not been applied to geophysical EM problems, Haber and Ruthotto ([73]) extended the work by Hou and Wu ([89]), Jenny et al. ([101]), and MacLachlan and Moulton ([123]) that propose multiscale FE/FV for elliptic equations, to develop a multiscale FV method for the quasi-static Maxwell's equations in the frequency domain. However, their work did not include oversampling and therefore, their method can result in inaccurate solutions due to 'resonance errors' (i.e., errors that appear when the mesh size and the wavelength of the small-scale oscillation of the coefficient are similar) [51, 89, 90].

In Chapter 4, I extend the oversampling technique proposed by Hou and Wu ([89]) developed for elliptic equations, for application to the quasi-static Maxwell's equations. I

In parallel to the multiscale community, the multigrid community has also been very active in proposing solutions to tackle boundary-value problems with multiple-scale features (for reviews see [22, 167] and references within). In the next section, I discuss some of the connections between the multiscale FE/FV and multigrid approaches proposed by these two communities.

2.6.3 Links between Multiscale FE/FV and Algebraic Multigrid

Multigrid or multilevel algorithms, introduced in the seminal paper by Brandt in 1977 ([21]), provide a methodology to design faster iterative solvers for systems of algebraic equations. Such a methodology delineates the principles to combine local processing on different levels (scales) with inter-level (inter-scale) transfer operators in order to design solvers that can yield linear (optimal) complexity, i.e.,

the computing processing is proportional to the problem size [24]. Since their inception, this methodology continues to be generalized to tackle a wide range of problems. Multigrid can be classified into two main branches: geometric and algebraic methods (see [24, 164] for details).

The design of an efficient algebraic multigrid (AMG) solver requires an effective coarsening process, i.e., the process of generating coarse-level problems (or operators) and inter-level restriction and interpolation operators. Such operators must satisfy certain weak-approximation properties, i.e., some necessary conditions for the iterative process to be convergent [55, 167]. The coarsening process is usually automatic and operator dependent (i.e., it uses information of the matrix of the system to be solved). An effective coarsening process to design robust AMG solvers is the so-called variational Galerkin coarsening [164].

Variational Galerkin coarsening automatically generates a hierarchy of coarse-level problems and coarse-to-fine interpolation operators by using minimization principles. For example, for a two-level method, given the finest-level operator (A_f, which is the matrix of the system to be solved), a coarse mesh, and an interpolation operator (P, which is also computed using variational principles), the coarse-mesh Galerkin operator ($A_c = P^T A_f P$) that minimizes the error in the range of the interpolation operator P is readily obtained [109, 164]. In this method, the restriction operator (R) is given by $R = P^T$. The construction of P gives rise to a coarse space defined by the range of P. That is, the construction of interpolation operators for a hierarchy of levels implies that a sequence of coarse spaces is also generated [26].

On the other hand, (Galerkin) multiscale FE/FV methods, discussed in the previous section, compute multiscale basis functions by solving local problems on each coarse-mesh cell. These basis functions are used in the weak formulation of the boundary-value problem of interest in order to create a coarse-mesh discretization operator A_c that has a similar form as the Galerkin operator described above (i.e., $A_c = P^T A_f P$), where the columns of P contains the assembled multiscale basis functions computed in each coarse-mesh cell. The above outlines one of the main connections between AMG and multiscale FE/FV methods.

AMG as a Numerical Upscaling Tool

The AMG methodology has also been used as a numerical upscaling tool, i.e., to solve a coarse-mesh problem (of the form $P^T A_f P x_c = P^T b$) rather than a large system of equations (of the form $A_f x = b$) that results from the FE discretization of a PDE on a fine mesh (see [167] for a review). Note that in the AMG context, the word 'upscaling' has a rather different meaning than the one given in Section 2.6.1. Here, it refers to an upscaled model, instead of a model with upscaled coefficients. Two AMG-based upscaling methods that are related to multiscale FE/FV methods for elliptic problems are the element-based AMG method and the multilevel multiscale mimetic method.

The element-based AMG (AMGe) method, originally proposed to design efficient AMG solvers in [26] and later extended for upscaling purposes in [113, 140], uses FE information in order to create a hierarchy of coarse spaces with guaranteed approximation properties that can be used as FE discretization spaces. The approximation properties of the constructed FE-based coarse spaces refer to the necessary and sufficient conditions to guarantee proper error estimates when AMGe is used as a discretization method. For a given level, AMGe computes the corresponding interpolation operator P by assembling local element-based interpolation operators that are computed on each algebraically-defined element in this level. For each element, the corresponding interpolation operator is computed by solving a local problem that is formulated using the FE information (including the local stiffness matrix) of such element. AMGe focuses on constructing hierarchies of FE-based coarse spaces for the De Rham complex, i.e., the sequence of H_1-conforming, $H(\text{curl})$-conforming, $H(\text{div})$-conforming and L_2-conforming spaces. The De Rham complex constitutes a convenient sequence of spaces where a broad class of PDEs problems can be handled. The method can work for unstructured (conforming) meshes and high-order FE. AMGe upscaling has been mostly applied to elliptic problems (e.g. [38, 114]). To the best of my knowledge, AMGe-upscaling applications for the Maxwell's equations have not been published yet.

The multilevel multiscale mimetic (M^3) method proposed in [119, 120] for time-dependent elliptic problems is also inspired in using the AMG methodology as an upscaling tool. M^3 uses Galerking coarsening in order to construct a hierarchy of

mimetic FD-based coarse-mesh problems. The accuracy of this coarsening procedure to generate a sequence of coarse-mesh discretizations was first shown in [122, 123], where a variational upscaling method is proposed for the Poisson's equation. However, this method does not produce locally conservative mass fields. In contrast, the M^3 is locally mass conservative in all levels and works for polyhedral meshes. To the best of my knowlege, extensions of M^3 to solve Maxwell's equations have not been published yet.

Chapter 3

An Upscaling Framework for the Electrical Conductivity

Look closely at the present you are constructing:
it should look like the future you are dreaming. — Alice Walker

3.1 Overview

This chapter[1] proposes an upscaling framework for the electrical conductivity of the mathematical model introduced in Section 2.3. The goal of this framework is to construct accurate coarse-mesh electrical conductivity models from given fine-mesh ones that can be used for faster simulation of the quasi-static EM responses on a coarse mesh.

The main idea behind the proposed framework is to *pose upscaling as a parameter estimation problem to be solved on each coarse-mesh cell*. As we will see in Section 3.2, this formulation is fundamentally different than others proposed in the upscaling literature. This chapter starts by introducing the components of the framework. Then, a 1D example that upscales well log conductivity data from the Canadian McMurray formation is used to illustrate the general principle behind the framework. Afterwards, the upscaling formulation is adapted in order to

---

[1]This chapter contains extended and revised versions of the material published in [29] and [32]. I am the lead author in both of these publications.

obtain a practical method for constructing 3D full-tensor conductivity models. Finally, the performance of the 3D upscaling formulation is demonstrated by using two examples on a single coarse cell, and one synthetic example based on the Canadian Lalor mine. The last example shows the feasibility of combining the proposed upscaling method with OcTree meshes in a parallel environment to boost its performance.

3.2 A Least-Squares Formulation of the Upscaling Problem

This section introduces the mathematical framework that poses the upscaling procedure as a parameter estimation problem.

Remember, the goal is to simulate EM responses for large-scale geophysical settings that consider highly heterogeneous media and features varying at multiple spatial scales. Often, the small-scale features have a significant effect on the measured EM responses (e.g. the thickness of a steel-cased well in Figure 1.3). In such cases, the accuracy of the computed EM responses of interest depends on our ability to capture the relevant fine-scale features into the simulation mesh. This results on using a large mesh, which leads to solving a huge system of equations, making the simulation computationally expensive, or even intractable.

Here, we propose an upscaling framework for the electrical conductivity that provides an alternative to avoid computing the EM responses of interest on a very large and fine mesh. To do so, the framework constructs upscaled electrical conductivities that vary on a coarser spatial scale and that emulate the effect of the fine-mesh electrical conductivity in the EM responses of interest. This set of upscaled electrical conductivities can be used for discretization on a much coarser mesh, thus reducing the size of the system of equations to be solved, and, in some cases, making the simulation doable. The upscaling process is illustrated in Figure 3.1.

Note that we cannot simply replace the fine mesh with a coarse mesh in the simulation procedure. Overlaying a coarse mesh over the fine mesh implies that several fine-mesh cells are captured into each of the coarse-mesh cells. This is illustrated for a single coarse cell in the central part of Figure 3.1. As a result,

41

Fine-scale electrical conductivity model Σ^f

Coarse-scale electrical conductivity model Σ^c

Ω

Ω

Ω_{up}

σ_{up}
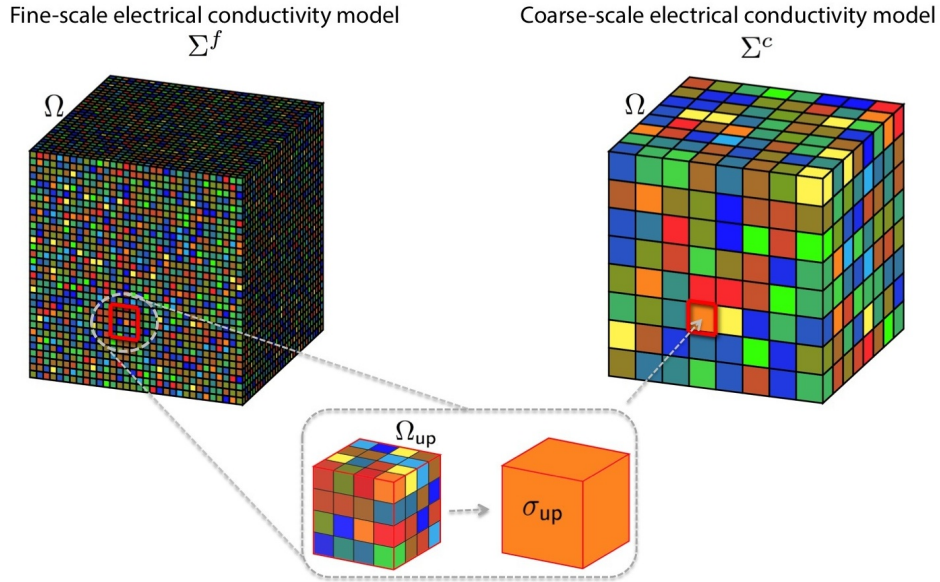
Figure 3.1: Upscaling process. Maxwell's equations are solved over the domain Ω, where the electrical conductivity can vary over multiple spatial scales and several orders of magnitude. The smallest spatial scale over which the conductivity varies defines the size of the fine mesh on which the model is discretized. The goal of an upscaling procedure is to homogenize the conductivity inside a subregion Ω_{up} of Ω in order to construct an upscaled electrical conductivity model suitable for simulation on a much coarser mesh.

a single coarse cell contains a heterogeneous fine-scale conductivity structure. From the continuity conditions of the EM fields across material interfaces [169], this implies that the EM responses within this coarse cell are non-smooth. In this case, using a standard discretization technique on the coarse mesh, such as FE or FV, will produce inaccurate approximations to the EM responses because such techniques assume a certain degree of smoothness in the function to be discretized. To avoid this complication when replacing the fine mesh with a coarse mesh, we first need to homogenize the fine-scale conductivity inside the coarse cells. That is, for each coarse cell, we need to assign a representative quantity for the heterogeneous, fine-scale conductivity contained in it. Doing so, we ensure smoothness in the resulting EM responses inside each cell. Afterwards, we can

safely apply traditional discretization techniques on the coarse mesh. We now proceed to develop the mathematical formulation for the upscaling procedure we propose.

We begin the development of the proposed upscaling framework by considering the quasi-static Maxwell's equations in the frequency domain subject to natural boundary conditions. These equations were introduced in Section 2.3. For simplicity of exposition, we assume that the magnetic permeability (μ) takes its free space value, namely $\mu = \mu_0 = 4\pi \times 10^{-7}$ Vs/Am. We use these quasi-static Maxwell's equations to define a fine- and a coarse-scale Maxwell's problem.

The fine-scale problem considers the Maxwell's equations where the heterogeneous electrical conductivity varies over small spatial scales. In our case, the term *fine scale* refers to the relevant smallest spatial scale over which the conductivity varies, such that this scale defines the size of the fine mesh on which the model is discretized to obtain an accurate approximation to the EM responses (see left-hand side of Figure 3.1). We use the superscript f to denote the fine-scale Maxwell's problem given by:

$$\nabla \times \vec{E}^f + \iota\omega\vec{B}^f \;\; = \vec{0}, \quad \text{in } \Omega, \tag{3.1}$$

$$\nabla \times (\mu_0^{-1})\vec{B}^f - \Sigma^f\vec{E}^f \;\; = \vec{J}_s, \quad \text{in } \Omega, \tag{3.2}$$

$$(\mu_0^{-1})\vec{B}^f(\vec{x}) \times \vec{n} \;\; = \vec{0}, \quad \forall \vec{x} \in \partial\Omega, \tag{3.3}$$

where $\Omega, \partial\Omega, \vec{E}^f, \vec{B}^f, \vec{J}_s, \Sigma^f, \omega, \vec{n}$ and ι are defined as before in Section 2.3.

On the other hand, the coarse-scale problem considers the Maxwell's equations where the electrical conductivity does not vary over small scale heterogeneities. The research work in [16, 17, 110, 173, 174] also assumes that the coarse-scale Maxwell's equation have the same form as the fine-scale Maxwell's equations except that the coefficients are replaced by upscaled coefficients. In our case, the term *coarse scale* refers to the largest spatial scale over which we can construct upscaled conductivities suitable for accurate simulation on a much coarser mesh (see right-hand side of Figure 3.1). We use the superscript c to

denote the coarse-scale Maxwell's problem given by:

$$\nabla \times \vec{E}^c + \iota\omega\vec{B}^c \;\; = \vec{0}, \quad \text{in } \Omega, \tag{3.4}$$

$$\nabla \times (\mu_0^{-1})\vec{B}^c - \Sigma^c\vec{E}^c \;\; = \vec{J}_s, \quad \text{in } \Omega, \tag{3.5}$$

$$(\mu_0^{-1})\vec{B}^c(\vec{x}) \times \vec{n} \;\; = \vec{0}, \quad \forall \vec{x} \in \partial\Omega, \tag{3.6}$$

where Ω, $\partial\Omega$, $\vec{E}^c$, $\vec{B}^c$, $\vec{J}_s$, ω, $\vec{n}$ and ι are defined as before in Section 2.3.

The fine- and coarse-scale problems use the same source term $\vec{J}_s$ as it is independent of the fine and coarse-scale variation of the conductivity. The upscaling problem consists on constructing a coarse-scale electrical conductivity Σ^c (without small scale heterogeneities) such that the solution of the coarse-scale problem is, in some sense, close to the solution of the fine-scale problem [56, 136].

Now, we define the coarse-scale electrical conductivity Σ^c as

$$\Sigma^c(\vec{x}; \sigma_{\text{up}}) = \begin{cases} \sigma_{\text{up}}, & \text{if} \quad \vec{x} \in \Omega_{\text{up}} \\ \Sigma^f(\vec{x}), & \text{otherwise} \end{cases} \tag{3.7}$$

where $\Omega_{\text{up}} \subset \Omega$ is an *upscaling region* where we aim to homogenize the fine-scale conductivity (Figure 3.1), and σ_{up} is an *upscaled electrical conductivity* that aims to capture the effect of the fine-scale heterogeneous conductivity inside Ω_{up} on the EM responses. In this framework, the definition of σ_{up} depends on the context of a simulation. For example, σ_{up} may be given by a positive scalar, a real or even a complex matrix, depending on the complexity and purpose of the simulation. We explore this idea further through examples in Sections 3.3 and 3.5.

We continue by rewriting the fine-scale problem (3.1)-(3.2) and the coarse-scale problem (3.4)-(3.5) as

$$\mathscr{L}(\Sigma^f(\vec{x}))\vec{u}^f = \vec{q}^f \quad \text{and} \quad \mathscr{L}(\Sigma^c(\vec{x}; \sigma_{\text{up}}))\vec{u}^c = \vec{q}^c, \tag{3.8}$$

respectively. Here, $\mathscr{L}$ represents the Maxwell operator (in matrix form), $\vec{u}^f = (\vec{B}^f, \vec{E}^f)^\top$ and $\vec{u}^c = (\vec{B}^c, \vec{E}^c)^\top$ represent the fine- and coarse-scale EM responses, respectively; and $\vec{q}^f$ and $\vec{q}^c$ represent the corresponding source and boundary conditions as given in (3.3) and (3.6), respectively. The fine- and coarse-scale EM

responses are obtained by inverting the Maxwell operator; that is,

$$\vec{u}^f(\Sigma^f(\vec{x})) = \mathscr{L}^{-1}(\Sigma^f(\vec{x}))\vec{q}^f \quad \text{and} \quad \vec{u}^c(\Sigma^c(\vec{x};\sigma_{\mathsf{up}})) = \mathscr{L}^{-1}(\Sigma^c(\vec{x};\sigma_{\mathsf{up}}))\vec{q}^c. \quad (3.9)$$

In practice, a geophysical EM forward modeling simulation is used to compute predicted data at the receiver locations or over the entire domain. The computation of the predicted EM data can be expressed as the action of a linear functional, $\mathscr{P}$, on the fine- and coarse-scale EM responses as follows

$$\vec{D}^f(\Sigma^f(\vec{x})) = \mathscr{P}\vec{u}^f(\Sigma^f(\vec{x})) \quad \text{and} \quad \vec{D}^c(\Sigma^c(\vec{x};\sigma_{\mathsf{up}})) = \mathscr{P}\vec{u}^c(\Sigma^c(\vec{x};\sigma_{\mathsf{up}})). \quad (3.10)$$

Throughout this work, we refer to $\vec{D}^f$ and $\vec{D}^c$ as the *fine- and coarse-scale EM data*, respectively. Note that when $\mathscr{P}$ equals the identity operator, (3.10) returns the EM responses in the entire simulation domain.

To complete the construction of Σ^c, we need to define a criterion for choosing the 'best' upscaled conductivity σ_{up} in the upscaling region Ω_{up}. As mentioned before, the coarse-scale conductivity (Σ^c) should be able to emulate the effect of the fine-mesh electrical conductivity in the EM responses of interest. That is, we require a criterion able to construct a σ_{up} such that the coarse- and fine-scale data are similar. We therefore propose the following definition.

Definition 1. *Let Σ^f be a given fine-scale electrical conductivity model and let $\vec{u}^f = (\vec{B}^f, \vec{E}^f)^\top$ be their induced fine-scale EM responses (i.e., fine-scale electric field and magnetic flux) given by (3.9), for a given angular frequency ω and sources including boundary conditions $\vec{q}^f$ and $\vec{q}^c$. Let $\vec{D}^f$ and $\vec{D}^c$, be some predicted fine- and coarse-scale EM data as defined in (3.10), then the upscaled electrical conductivity in the upscaling region Ω_{up}, denoted as σ_{up}^*, is defined as the solution of the following parameter estimation problem:*

$$\sigma_{\mathsf{up}}^* = \arg\min_{\sigma_{\mathsf{up}}} c(\sigma_{\mathsf{up}}) = \frac{1}{2}\left\|\vec{D}^c(\Sigma^c(\vec{x};\sigma_{\mathsf{up}})) - \vec{D}^f(\Sigma^f(\vec{x}))\right\|_2^2. \quad (3.11)$$

We refer to $c(\sigma_{\mathsf{up}})$ as the upscaling criterion.

The parameter estimation problem (3.11) satisfies that the number of parameters is less than (or equal) to the number of data and it is a well-posed least-

squares problem, hence no additional regularization is required. Our formulation is a type of global upscaling procedure within the classification of upscaling techniques proposed in [49, 56] for fluid flow problems in porous media. In a global upscaling procedure, the entire fine-scale model is simulated for the calculation of the coarse-scale PDE coefficient(s).

The investigations in [85, 136] propose another least-squares upscaling formulation for fluid flow problems in porous media. In such investigations, all the upscaled permeabilities are computed at once by minimizing the regularized least-squares difference between the pressure and the velocity fields generated by the fine- and coarse-scale pressure equations.

We solve the parameter estimation problem (3.11) numerically. We use the discretize-then-optimize approach, where in the first stage we discretize the forward problem and in the second stage we solve the finite-dimensional discrete optimization problem. This approach is typically used in the literature to solve PDE-constrained optimization problems in EM Geophysics (see [20, 67, 68], and references within). The main advantages of this approach are that it allows for an efficient integration of convex optimization algorithms with advanced PDE discretization techniques and solvers, and that it leads to more consistent solutions. In order to use this approach, we require both a stable discretization and an appropriate convex optimization method to solve the discrete version of (3.11). In the examples presented in Sections 3.3 and 3.5 we specify the choices we made in each case.

Remarks

1. The upscaling definition 1 we propose may look rather involved at first; however, an analogy can be drawn from the computation of an apparent conductivity (or resistivity) in a Direct Current Resistivity experiment. Although it would not be used for the purposes of simulation, the apparent conductivity can be considered as an upscaled quantity. For a given electrode geometry, the apparent conductivity is the homogeneous halfspace conductivity that produces an upscaled response to the one observed [169]. Within this upscaling context, the apparent conductivity corresponds to the quantity σ_{up}^*,

Ω_{up} is the homogeneous earth (in this case, $\Omega_{\mathrm{up}} = \Omega$), $\vec{q}$ are the sources, $\vec{u}$ are the potentials, $\mathscr{P}$ projects the fields onto the receiving electrode locations, and the data $\vec{D}^f$ and $\vec{D}^c$ are the measured voltages.

2. One aspect of the upscaling definition 1 is that the upscaling region Ω_{up} can include its surrounding conductivity structure. That is, the upscaled conductivity can correspond to an on-site sampling of the electrical conductivity. We demonstrate that constructing upscaled conductivities in this manner yields to more accurate approximations to their corresponding induced EM responses in the examples included in Sections 3.3 and 3.5.

3. The upscaling formulation 3.11 considers the connection between the particular EM experiment configuration used in the simulation and the type of EM responses that it produces into the calculation of the upscaled conductivities. This is accomplished both through the source term and boundary conditions ($\vec{q}$), and the choice of data of interest ($\vec{D}^c$, $\vec{D}^f$). For instance, the data of interest can be chosen among the electric or magnetic fields or fluxes (i.e., $\vec{E}, \vec{H}, \vec{B}$ or $\vec{J}$), or some combination of them.

4. The upscaling formulation 3.11 is very flexible and provides a user-defined, application-specific framework to upscale the electrical conductivity of our Maxwell's system. The upscaled conductivity can be a real or a complex-valued scalar, or a real or complex-valued matrix, depending on the complexity of the setting, the purpose of the coarse-scale simulation, and the required accuracy of the solution. Furthermore, the upscaling criterion (3.11) need not be based on least-squares. The examples presented in Sections 3.3 and 3.5 are designed to demonstrate these features.

5. Having an application-specific framework is important because it accounts for the fact that there is no unique upscaled conductivity suitable for all simulation purposes. Indeed, constructing a different upscaling criterion by changing the data simulated or sources used to excite the system typically leads to a different upscaled conductivity. We demonstrate this point in the examples presented in Section 3.5.1. Additionally, the experiments

presented in Sections 3.3 and 3.5.2 demonstrate that by changing the frequency of the survey, it is possible to obtain different upscaled conductivity quantities. This can be explained by the fact that different EM survey configurations have different sensitivity functions and sample the earth differently. Thus, the effect of heterogeneous conductivities in the EM data we measure often differs from experiment to experiment. For example, this effect can be observed when considering Direct Current Resistivity surveys, where an apparent conductivity computed from a pole-dipole survey may be different than for a dipole-pole survey [144].

In the next sections we discuss the upscaling procedure for 1D and 3D EM geophysical forward modeling and provide examples that demonstrate its performance.

3.3 Numerical Results in 1D

We show the performance of the proposed global upscaling framework on a 1D example. The purpose of this example is twofold. First, we show how to upscale a well log electrical conductivity model for both a single frequency and a multi-frequency airborne loop-loop survey using our framework. Second, we demonstrate that when coarse-scale conductivity models consider the survey configuration in their construction, they lead to more accurate simulation results.

3.3.1 Simulations Using a Single Frequency

Well logging is the process of recording various physical, chemical, electrical, or other properties of the rock/fluid mixtures penetrated by drilling a borehole into the Earth's crust [144]. Well logs are recorded in nearly all oil and gas wells and in many mineral and geothermal exploration and development wells. Well log conductivity measurements[2] have high resolution, with samples every few centimeters. However, if these conductivity measurements are to be used for earth-scale simulations or inversions, coarse-scale conductivity models, defined on the order of meters, are needed. This context provides the perfect scenario to test

---

[2]In reality, well log data considers resistivity measurements. Since electrical conductivity is the reciprocal value of resistivity, we can obtain conductivity measurements using this relationship.

our upscaling framework and to offer a potential alternative to upscale well log conductivity data in practice. Most of the times in practice, log measurements are simply averaged to obtain effective petrophysical properties, but as we see next, this may lead to large errors.

We use a fine-scale electrical conductivity model, Σ^f, given by an induction resistivity log from the McMurray/Wabiskaw Oil Sands deposit well log public database [176]. The McMurray formation is located in Northern Alberta, Canada, and the log used is shown in Figure 3.2(a). Observe that the interval over which conductivity samples were taken is 80 m, thus we take this as the simulation domain, i.e., $\Omega = [0, 80]$ m. In addition, observe that the electrical conductivity ranges over four orders of magnitude. The log chosen has 320 measurements total, with a measurement taken every 25 cm. Hence, we defined a uniform fine mesh whose thickness is consistent with this scale.

We consider a standard airborne survey configuration ([144]), with a frequency of 300 Hz and a horizontal coplanar arrangement for the source receiver-pair. The source-receiver pair is located at a height of 40 m above the earth's surface and has a separation of 8.1 m. The source produces a magnetic field, which induces currents in the earth, producing secondary magnetic fields, which we measure at the receiver.

We aim to simulate the magnitude of the magnetic field (H-field) for the given survey configuration using a coarse-scale conductivity model that can be discretized using a much coarser mesh. From now on, we refer to the coarse-scale conductivity model as the coarse-mesh conductivity model.

To construct a coarse-mesh conductivity model that varies on the meter scale using the proposed upscaling framework, we need to choose: (a) a suitable coarse mesh, (b) the type of upscaled quantity to be constructed, and (c) an upscaling criterion.

For the coarse mesh, we consider a uniform mesh nested in the fine mesh with 10 m thickness for each coarse layer. Hence, inside the simulation domain we have eight coarse layers, where each of them contains a large range of fine-scale conductivity variation to be upscaled, see Figure 3.2(a). We base the estimate for the proper cell sizes of the coarse mesh on the skin depth ([169]). Practical experience on mesh design for EM problems reported in [68] suggests that

49

the smallest cell size in the mesh should be a quarter the minimum skin depth. We consider the median conductivity value (2.3×10^{-2} S/m) and calculate a skin depths of 191.5 m for the frequency of 300 Hz. Therefore, using cell sizes of 10 m is sufficient to capture the decaying behavior of the EM fields in this setup.

We assume the upscaled conductivity inside each coarse layer is given by a real positive scalar. This is a common assumption in practice when the forward modeling code only handles isotropic conductivity models. A more general assumption is to consider the upscaled conductivity to be a matrix; however, this would require the forward modeling code to be capable of incorporating anisotropy, which is not always the case. We will elaborate further on 3D cases which incorporate anisotropy in Sections 3.4 and 3.5.

Since we aim to simulate the magnitude of the magnetic field at the receiver location, we take this as the EM data to be matched in the upscaling criterion (3.11). By doing so, we have specified the source term (including boundary conditions) and the data of interest, which define the necessary elements of the upscaling criterion for this example.

Once the necessary elements to setup the framework are selected, the construction of the coarse-mesh conductivity model is completed by solving a parameter estimation problem for every coarse layer separately. The set of eight upscaled conductivities will form the coarse-mesh conductivity model.

As mentioned in Section 3.2, we use the discretize-then-optimize approach to solve each of the eight parameter estimation problem (3.11). To compute the upscaled conductivity on a given coarse layer, we use the EM1DFMfwd code developed by members of the Geophysical Inversion Facility to forward model the necessary fine and coarse H-field data. The EM1DFMfwd code implements the matrix propagation approach proposed in [57]. Since we have a single H-field datum and we are inverting for a single scalar, our parameter estimation problem is well-defined for this example. To solve the discrete version of the optimization problem (3.11), we use the MATLAB function fminbnd [162]. Such function implements a standard derivative-free minimization method for single-variable functions on a fixed interval (for more details see [25]). We use a derivative-free optimization method as an explicit calculation of the derivatives of the upscaling criterion are not available in this case. The resulting coarse-mesh conductivity model is

50
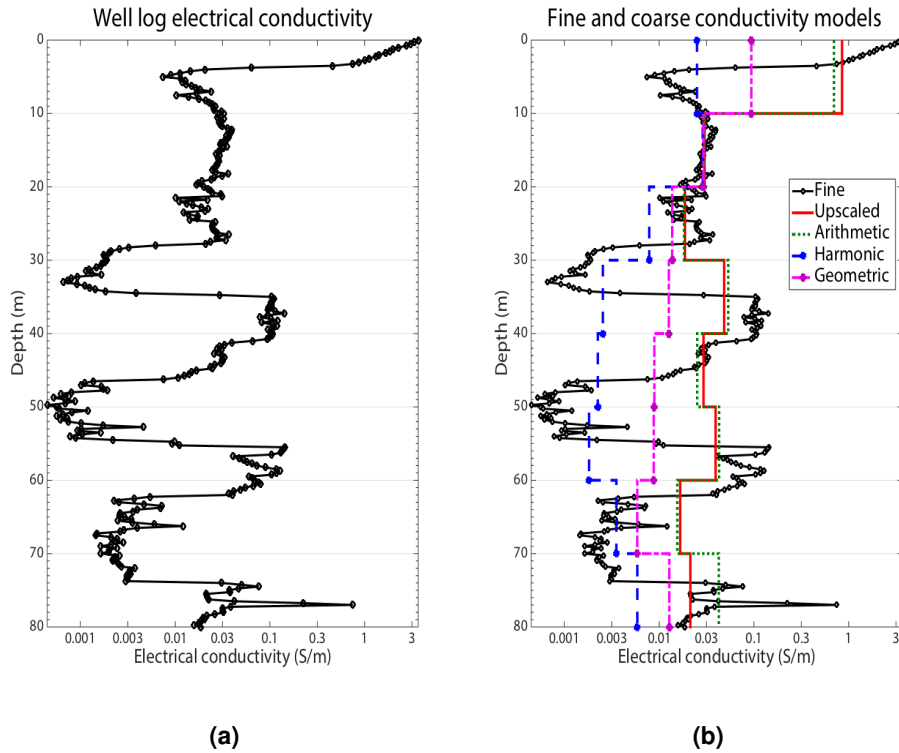
Figure 3.2: Induction resistivity log: AA-05-01-096-11w4-0 from the McMurray/Wabiskaw Oil Sands deposit well log database. (a) Discrete fine-scale conductivity model. Each diamond represents a conductivity value on a uniform fine mesh of thickness 25 cm. Each straight line represents a coarse layer of a uniform mesh of thickness 10 m. The setup considers 320 fine layers and 8 coarse layers. (b) Resulting coarse-mesh conductivity models after applying four upscaling procedures: 1D numerical upscaling procedure (red solid line), and arithmetic (green dot line), geometric (magenta dot dash line), and harmonic (blue dash line) averages.

plotted with a red solid line in Figure 3.2(b).

Note that calculating an upscaled conductivity following the procedure outlined above requires using the fine-mesh conductivity model, which corresponds in the upscaling literature for flow applications to perform a global upscaling procedure [49, 56]. This is a serious drawback to perform 3D simulations in practice. In

51

Section 3.4 we show how to modify our upscaling framework for 3D settings to avoid this complication.

To compare our method to other 1D average-based upscaling methods, we construct coarse-mesh conductivity models using volume-arithmetic, -geometric and -harmonic averaging of the fine-mesh conductivity inside each coarse layer. The resulting coarse-mesh conductivity models are shown in Figure 3.2(b). From this figure, we observe that the coarse-mesh conductivity model produced by our proposed upscaling procedure resembles the coarse-mesh model produced by volume-arithmetic averaging for most of the coarse cells.

To judge the quality of the various coarse-mesh conductivity models as compared to the fine-mesh conductivity model, we use each of the models to forward model a H-field datum at the receiver location using the EM1DFMfwd code on the coarse and fine mesh, respectively. Table 3.1 shows the magnitude of the resulting H-field datum for each of the conductivity models and their corresponding relative errors. The relative error is computed as the ratio of the absolute value of the difference in magnitude of the fine- and coarse-mesh datum to the absolute value of the fine-mesh datum in magnitude.

The results in Table 3.1 demonstrate that the proposed upscaling formulation constructed an optimal coarse-mesh conductivity model, in the sense of equation (3.11), for the airborne survey configuration given and the surrounding conductivity structures, as it yields the smallest relative error in the approximation of the H-field datum of interest. That is, our method gives and optimal on-site prediction of the upscaled conductivity, as defined in equation (3.11), that is fundamentally different from the one given by the other average-based homogenization methods presented. Note that by upscaling the conductivity model we can reduce the mesh size from using 320 cells to use only 8 cells without sacrificing much accuracy.

In the next section, we demonstrate the effect of considering multiple frequencies in the construction of the coarse-mesh conductivity model.

3.3.2 Simulations Using Multiple Frequencies

In this case, we want to construct coarse-mesh conductivity models to simulate H-field measurements at five frequencies logarithmically equispaced in the range

Table 3.1: Magnitude of the magnetic field (H-field) datum and relative errors resulting from forward modeling using the fine-mesh and four coarse-mesh conductivity models. Note: $\%^*$ denotes percentage of primary field.

Conductivity model	Magnitude of H-field ($\%^*$)	Relative error (percent)	No. of layers in mesh
Fine	0.0549	——	320
Upscaled	0.0536	2.37	8
Arithmetic	0.0468	14.74	8
Geometric	0.0102	81.42	8
Harmonic	0.0043	92.22	8

from 10 to 30,000 Hz (i.e., we use the frequencies of 10, 74, 547, 4,053 and 30,000 Hz). To do so, we use the same setup for the fine and coarse meshes, and the same airborne-style survey configuration as described in the previous section.

Considering the median conductivity value (2.3×10^{-2} S/m), the skin depths for the frequencies of 10, 74, 547, 4,053 and 30,000 Hz are roughly 1,049, 386, 142, 52 and 19 m, respectively. Thus, using cells sizes of 10 m continues to be sufficient to capture the behavior of the magnetic fields in this setup for the first four frequencies. We challenge the upscaling method with a larger cell size for the last frequency.

We applied the proposed upscaling procedure by optimizing a discrete version of (3.11) for each of the eight coarse layers separately, and each individual frequency, as described in the previous section. The resulting coarse-mesh conductivity models are shown in Figure 3.3(a). Note that for each frequency, we obtained a different coarse conductivity model. This follows from the fact that the upscaled conductivity model is tailored to match the magnetic field determined by the survey parameters. These parameters influence the sensitivity of the magnetic field to the conductivity structure. Hence, varying any of these parameters alters how the conductivity structure is sampled. As a result, the upscaled conductivity model may take on different values depending on the experimental setting, demonstrating that the proposed upscaling approach provides

a user-defined, application-specific framework. These results also imply that the upscaled conductivity changes as a function of frequency, demonstrating that frequency dependence on the coarse-scale considered may arise as a result of local, fine-scale heterogeneity.

To conclude this example, we construct coarse-mesh conductivity models using volume-arithmetic, -geometric and -harmonic averaging of the fine-mesh conductivity inside each coarse layer. For each of these coarse conductivity models, H-field data were then simulated on the coarse mesh using the given airborne survey configuration using the EM1DFMfwd code. We compare the resulting H-field data with those computed using the fine-mesh conductivity model for each frequency in Figure 3.3(b). The H-field data shown are given in percentage of the magnitude of the primary field. Table 3.2 shows the relative errors obtained for each case. The relative error is computed as the ratio of the Euclidean norm of the difference in magnitude of the fine- and coarse-mesh data to the Euclidean norm of the fine-mesh data in magnitude. From this table, we observe that, once again, the proposed upscaling approach leads to better approximations to the desired H-field data than using the coarse models constructed by average-based upscaling procedures for all the frequencies used.

Table 3.2: Relative errors for four coarse-mesh conductivity models and for five frequencies.

	Relative errors for coarse-mesh conductivity models			
Frequency (Hz)	Upscaled (percent)	Arithmetic (percent)	Geometric (percent)	Harmonic (percent)
10	0.64	9.93	83.46	93.34
74	2.78	12.76	83.36	93.23
547	8.21	15.55	80.85	92.05
4,053	11.76	15.80	66.83	85.09
30,000	0.84	9.59	32.55	55.30

Performing 1D upscaling of well log conductivity measurements, as shown in this example, provides a practical technique to construct accurate coarse-scale conductivity models to be used on large-scale 3D simulations or inversions. Our upscaling procedure resulted in more accurate approximations to the EM responses
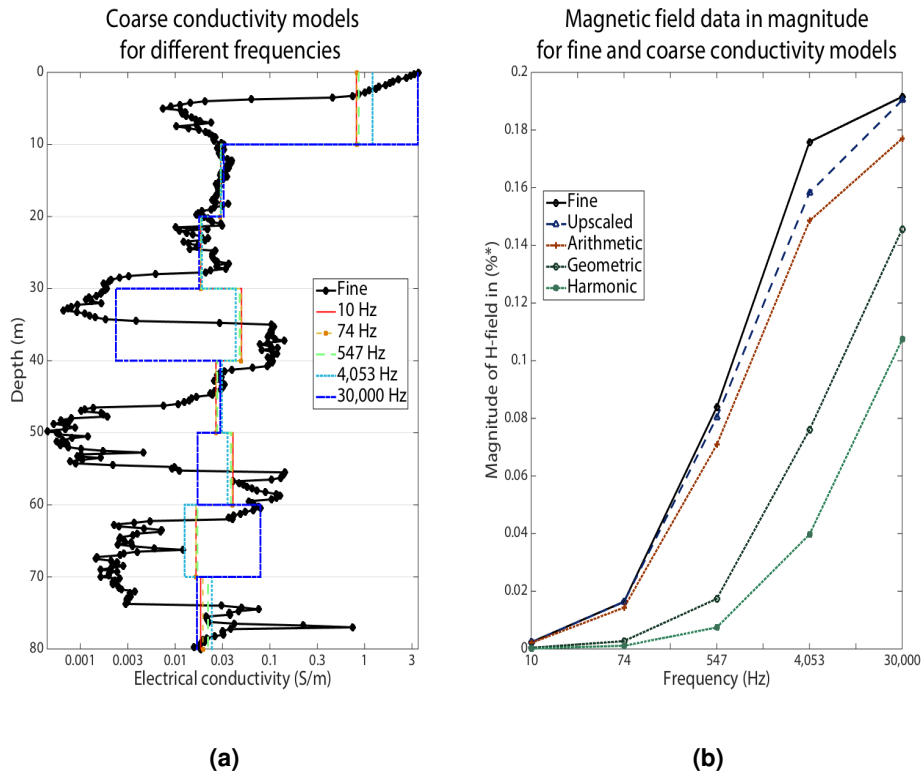
Figure 3.3: (a) Coarse-mesh electrical conductivity models obtained by using the proposed upscaling method for different frequencies. The setup considers 320 fine layers and 8 coarse layers. (b) Magnitude of magnetic field for each frequency, in % of primary field ($\%^*$), resulting from forward modeling using the fine-mesh electrical conductivity model (black solid line), the different coarse-mesh conductivity models displayed in (a) (blue dash line), and the coarse-mesh models produced by using arithmetic (red plus dot line), geometric (gray circle dot line), and harmonic averages (green square dot line).

of interest at the cost of more computational performance, as compared to traditional average-based upscaling procedures. However, for 1D problems, using our (global) upscaling framework may be considered to be more appealing as 1D simulations present minimal computational bottlenecks.

The example presented illustrates the general principle behind our upscaling framework by showing its performance in 1D well log data. However, applying

the current upscaling formulation (3.11) to a general 3D setting is not practical. It requires simulating the data to be matched (3.10) on the entire fine mesh, which can be computationally demanding. In the next section, we address the challenge of creating a practical upscaling approach for a 3D setting.

3.4   A Local Upscaling Framework for 3D Simulations

Applying the global upscaling framework introduced in Section 3.2 as shown in Section 3.3 is impractical for 3D simulations. It requires simulations using the entire fine-mesh conductivity model. In this section, we adapt the proposed upscaling framework for practical application to 3D settings.

To create a pragmatic upscaling method, we combine our least-squares formulation with the methodology proposed by Durlofsky in [48, 49] for the field of simulating flow in heterogeneous porous media to EM modeling. That is, using some specialized boundary conditions, we apply the upscaling procedure locally instead of globally. In our case, this means that for each coarse-mesh cell, we locally solve a parameter estimation problem to construct an upscaled conductivity. Doing so cell by cell, potentially in parallel, yields the desired coarse-mesh conductivity model. This approach enables us to solve several smaller problems rather than a single large one, making this procedure suitable for tackling large-scale EM problems.

We now discuss, in detail, how to locally apply the upscaling framework. We assume that a given fine-scale conductivity model is discretized at the cell-centers of a 3D fine staggered mesh, $\mathcal{M}^h$. The fine mesh sufficiently captures the relevant conductivity variations in the model. We denote the discrete fine-mesh conductivity model as $\mathbf{\Sigma}^h$. We aim to construct a coarse-mesh conductivity model, $\mathbf{\Sigma}^H$, that is also discretized at the cell-centers of a user-chosen 3D coarse staggered mesh, $\mathcal{M}^H$. Typically, $\mathcal{M}^H$ is much coarser than $\mathcal{M}^h$. Throughout this section, the superscripts h and H denote dependency on the fine and coarse meshes, respectively. The fine and coarse meshes are a union of n fine cells and N coarse cells, respectively. That is, $\mathcal{M}^h = \cup_{i=1}^{n} \Omega_i^h$ and $\mathcal{M}^H = \cup_{k=1}^{N} \Omega_k^H$, where $N \ll n$. For simplicity, we also assume that the meshes are nested, that is $\mathcal{M}^H \subset \mathcal{M}^h$; however, the argument presented here can be extended to include more general mesh
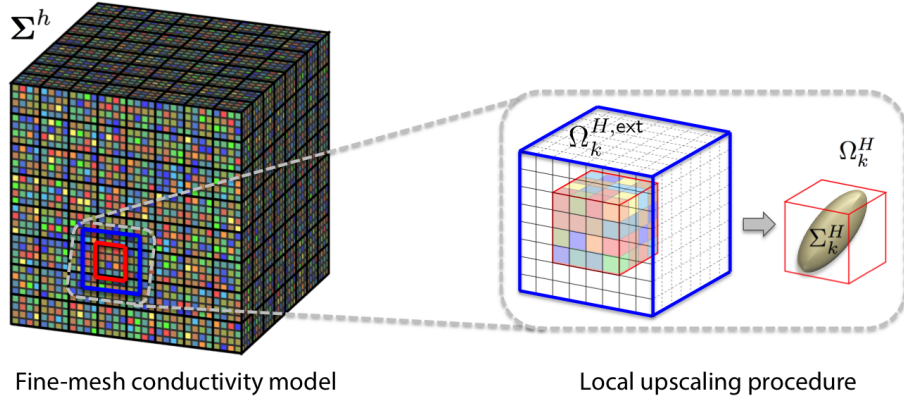
Figure 3.4: Local upscaling procedure for 3D settings. Left: fine-mesh electrical conductivity model and example of nested meshes setup. Right: extended domain ($\Omega_k^{H,\text{ext}}$) for a given coarse-mesh cell (Ω_k^H) and resulting anisotropic upscaled electrical conductivity ($\mathbf{\Sigma}_k^H$).

setups. A sketch of the mesh setup described is shown in Figure 3.4.

Since the goal is to apply the upscaling procedure on each coarse-mesh cell independently and locally, we need to identify: (a) the upscaling region, (b) the type of upscaling quantity to be constructed, and (c) the data to be matched in a local version of the parameter estimation problem (3.11). We discuss each of these choices for a single coarse cell below.

Let us consider a single coarse-mesh cell, Ω_k^H. The upscaling region corresponds to Ω_k^H, which is composed of the fine cells and the fine conductivity structure it encloses. To construct an upscaled conductivity in Ω_k^H that takes into account the surrounding conductivity structure (i.e., to preserve the on-site sampling feature of the fine-scale conductivity), we embedded Ω_k^H in an extended domain, $\Omega_k^{H,\text{ext}}$. This extended domain $\Omega_k^{H,\text{ext}}$ includes Ω_k^H and a neighborhood of fine cells (and their corresponding conductivity values) around Ω_k^H. This is illustrated in Figure 3.4. The size of the extended domain is user-chosen. We explore the effect of different extensions in the examples presented in Section 3.5.

To better represent most of the existing heterogeneity inside Ω_k^H, we assume the upscaled conductivity to be constructed for this cell to be a full SPD matrix (i.e., fully anisotropic). Full-tensor effects generally arise at the coarse scale, even

though the fine-scale conductivity is isotropic [35]. We denote the upscaled conductivity in Ω_k^H as Σ_k^H. That is, Σ_k^H is a real SPD matrix that can be parametrized using six scalars, $\vec{\sigma}_k = (\sigma_1^k, \sigma_2^k, \sigma_3^k, \sigma_4^k, \sigma_5^k, \sigma_6^k) \in \mathbb{R}^6$, as follows:

$$\Sigma_k^H(\vec{\sigma}_k) = \begin{bmatrix} \sigma_1^k & \sigma_4^k & \sigma_5^k \\ \sigma_4^k & \sigma_2^k & \sigma_6^k \\ \sigma_5^k & \sigma_6^k & \sigma_3^k \end{bmatrix}. \tag{3.12}$$

According to Definition 1 given in Section 3.2, in order to construct Σ_k^H by solving a parameter estimation problem, we require some fine- and coarse-scale data to be matched in the upscaling criterion (3.11). To generate such data, the Maxwell system should be excited by either a source or some boundary conditions, see (3.10).

Since we apply the upscaling procedure locally, we assume that sources do not reside inside $\Omega_k^{H,\text{ext}}$. Therefore, rather than choosing some local source(s) to induce EM responses, we assume that the system is excited by some non-homogeneous boundary conditions. Such boundary conditions should reflect the behavior of the EM responses of interest across the boundary of Ω_k^H, which is denoted as $\partial\Omega_k^H$.

In principle, the correct boundary conditions can be obtained numerically by solving the fine-mesh problem; however, they are impractical to compute. One remedy for this problem, suggested in [49] (for fluid flow problems), is to use a set of linearly independent boundary conditions. Note that using linear boundary conditions in the context of the EM problem can be appropriate to model the action of distant sources on $\partial\Omega_k^H$ as such action can be perceived as a 'plane wave'.

Now, to generate the data, we first generate fine- and coarse-scale EM responses by locally exciting the Maxwell system using a set of twelve linearly independent, non-homogeneous Dirichlet boundary conditions (one per edge of $\Omega_k^{H,\text{ext}}$). This yields the following set of twelve local problems:

$$\nabla \times \vec{E}_l^k + \iota\omega\vec{B}_l^k = \vec{0}, \text{ in } \Omega_k^{H,\text{ext}}; \tag{3.13}$$

$$\nabla \times (\mu_0^{-1}\vec{B}_l^k) - \Sigma^k \vec{E}_l^k = \vec{0}, \text{ in } \Omega_k^{H,\text{ext}}; \tag{3.14}$$

$$\vec{E}_l^k(\vec{x}) \times \vec{n} = \vec{\Phi}_l(\vec{x}) \times \vec{n}, \ \forall \vec{x} \in \partial\Omega_k^{H,\text{ext}}, \tag{3.15}$$

with $l = 1, \ldots, 12$. Here, $\vec{x} = (x_1, x_2, x_3) \in \mathbb{R}^3$, $\partial\Omega_k^{H,\text{ext}}$ denotes the boundary of $\Omega_k^{H,\text{ext}}$, and $\vec{\Phi}_l$ is a vector function that denotes the lth Dirichlet boundary condition as defined in Table 3.3. From Figure 3.5, we observe that each $\vec{\Phi}_l$ takes the value 1 along the tangential direction to the lth edge of Ω_k^H and decays linearly to 0 in the normal directions to the same edge.

Table 3.3: Analytical expressions for the set of linearly independent boundary conditions used to locally generate data in the cuboid cell $\Omega_k^{H,\text{ext}}$ (one per edge). Note that $\vec{x} = (x_1, x_2, x_3) \in \mathbb{R}^3$.

$\vec{\Phi}_1(\vec{x}) = [x_2 x_3, 0, 0]^\top$	$\vec{\Phi}_5(\vec{x}) = [0, x_1 x_3, 0]^\top$	$\vec{\Phi}_9(\vec{x}) = [0, 0, x_1 x_2]^\top$
$\vec{\Phi}_2(\vec{x}) = [x_3(1-x_2), 0, 0]^\top$	$\vec{\Phi}_6(\vec{x}) = [0, x_3(1-x_1), 0]^\top$	$\vec{\Phi}_{10}(\vec{x}) = [0, 0, x_2(1-x_1)]^\top$
$\vec{\Phi}_3(\vec{x}) = [x_2(1-x_3), 0, 0]^\top$	$\vec{\Phi}_7(\vec{x}) = [0, x_1(1-x_3), 0]^\top$	$\vec{\Phi}_{11}(\vec{x}) = [0, 0, x_1(1-x_2)]^\top$
$\vec{\Phi}_4(\vec{x}) = [(1-x_2)(1-x_3), 0, 0]^\top$	$\vec{\Phi}_8(\vec{x}) = [0, (1-x_3)(1-x_1), 0]^\top$	$\vec{\Phi}_{12}(\vec{x}) = [0, 0, (1-x_2)(1-x_1)]^\top$

The set of boundary conditions used ($\{\vec{\Phi}_l\}_{l=1}^{12}$) form the natural basis functions for linear edge degrees of freedom of a hexahedral finite element [104, 131]; they can be used to model general linearly varying EM responses. That is, this set of boundary conditions allows us to generate a set of linearly independent (local) data, which can be used to formulate a full-rank, overdetermined parameter estimation problem. Similar choices were proposed in [49, 51] for the problem of simulating fluid flow in porous media, where the PDE model is the Poisson equation. Different studies for flow in porous media have shown that different choices of boundary conditions lead to different upscaled quantities [48, 49, 56, 175].

To compute the fine-scale EM responses for the kth local problem, we use the fine-mesh conductivity contained in $\Omega_k^{H,\text{ext}}$, denoted as Σ_k^h. To compute the coarse-scale EM responses for the kth local problem, we assign Σ_k^H as the conductivity value of every fine-mesh cell inside $\Omega_k^{H,\text{ext}}$. Using the corresponding conductivity values of every fine cell inside $\Omega_k^{H,\text{ext}}$, we can now forward model each of the twelve problems (3.13)-(3.15) to obtain a set of fine and coarse EM responses, respectively. To obtain each set, we discretize each of these problems using the MFV method as outlined in Section 2.4. Other traditional edge-based discretization methods, such as an edge-based FE method [104, 131], can be used for this part as well as long as they provide a consistent, conservative and stable discretization for our Maxwell system. After the discretization, we obtain a

set of twelve discrete electric fields, $\mathbf{E_k} = \{\mathbf{e_1^k}, \ldots, \mathbf{e_{12}^k}\}$, and a set of twelve discrete magnetic fluxes, $\mathbf{B_k} = \{\mathbf{b_1^k}, \ldots, \mathbf{b_{12}^k}\}$. Note that each $\mathbf{e_l^k}$ is a vector whose length equals the number of fine-mesh edges in $\Omega_k^{H,\text{ext}}$, and that each $\mathbf{b_l^k}$ is a vector whose length equals the number of fine-mesh faces in $\Omega_k^{H,\text{ext}}$.
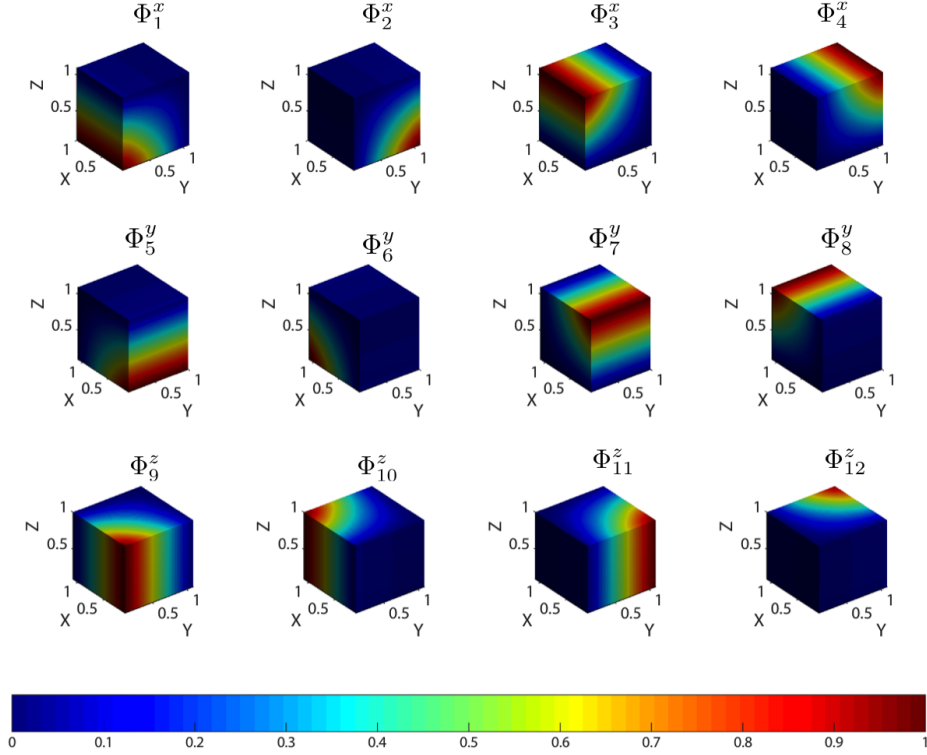
Figure 3.5: Non-zero component of each vectorial basis function $\vec{\Phi}_l$ (defined in Table 3.3) plotted on a unitary cube.

Next, we need to choose which fine and coarse data are to be matched and how the local version of the upscaling criterion (3.11) will be formulated. We note that the heterogeneous fine-scale conductivity structure inside Ω_k^H generates non-smooth responses on $\partial\Omega_k^H$. Since the role of the upscaled conductivity is to emulate the effect of the fine-scale conductivity inside Ω_k^H on the EM responses at $\partial\Omega_k^H$, for us it makes sense to consider the data to be either the integral of the electric field over the twelve edges of $\partial\Omega_k^H$, or the integral of the magnetic flux

over the six faces of $\partial\Omega_k^H$. We refer to these data as the total electric fields or total magnetic fluxes, respectively.

To be more specific, we define the *total electric field data* as

$$d_{lm} = \int_{\text{edge}_m} \vec{E}_l^k \cdot \vec{\tau}_{\text{edge}_m} \, d\ell; \quad l = 1, \ldots, 12, \; m = 1, \ldots, 12, \qquad (3.16a)$$

and the *total magnetic flux data* as

$$d_{lj} = \int_{\text{face}_j} \vec{B}_l^k \cdot \vec{n}_{\text{face}_j} \, dS; \quad l = 1, \ldots, 12, \; j = 1, \ldots, 6, \qquad (3.16b)$$

where edge_m represents the mth edge of $\partial\Omega_k^H$, $\vec{\tau}_{\text{edge}_m}$ denotes the unit tangent vector to edge_m, face_j represents the jth face of $\partial\Omega_k^H$, and $\vec{n}_{\text{face}_j}$ represents the unit outward-pointing normal vector to face_j. The data can be calculated by numerically integrating (3.16a) and (3.16b) using the set of discrete fields $\mathbf{E_k}$ or fluxes $\mathbf{B_k}$, respectively. Remember that $\mathbf{E_k}$ and $\mathbf{B_k}$ are discretized on the fine-mesh edges and fine-mesh faces inside $\Omega_k^{H,\text{ext}}$, respectively.

As before, the choice of the data to be matched during the local upscaling procedure depends on the context of a given simulation and it significantly influences the construction of the upscaled conductivity. We will demonstrate both of this aspects in the examples presented in Section 3.5. These phenomena have been also observed on upscaling procedures for fluid flow problems in porous media [47, 49, 56, 60, 85, 136, 175].

Finally, we formulate the local version of the discrete parameter estimation problem (3.11) to be solved in order to construct $\mathbf{\Sigma}_k^H$ as follows:

$$\vec{\sigma}_k^{\text{opt}} = \underset{\vec{\sigma}_k \in \mathbb{R}^6}{\arg\min} \; \overline{c}(\vec{\sigma}_k) = \frac{1}{2} \sum_{l=1}^{12} \left\| \mathbf{d}_l\big(\overline{\mathbf{\Sigma}}_k^H(\vec{\sigma}_k)\big) - \mathbf{d}_l\big(\mathbf{\Sigma}_k^h\big) \right\|_2^2$$
$$\text{subject to } \overline{\mathbf{\Sigma}}_k^H(\vec{\sigma}_k) \text{ is SPD.} \qquad (3.17)$$

Here, $\mathbf{d}_l\big(\mathbf{\Sigma}_k^h\big)$ denotes the 12×1 vector whose entries are the lth total electric field data (3.16a) or the 6×1 vector whose entries are the lth total magnetic flux data (3.16b) computed for the fine-mesh conductivity in $\Omega_k^{H,\text{ext}}$ (that is, $\mathbf{\Sigma}_k^h$), respectively. Analogously, $\mathbf{d}_l\big(\overline{\mathbf{\Sigma}}_k^H(\vec{\sigma}_k)\big)$ denotes the vector whose entries are the lth total

electric field data (3.16a) or total magnetic flux data (3.16b) computed for the up-scaled conductivity $\overline{\mathbf{\Sigma}}_k^H(\vec{\sigma}_k)$, given by (3.12), extended to $\Omega_k^{H,\text{ext}}$, respectively. That is, the *anisotropic upscaled conductivity for the cell* Ω_k^H is given by $\mathbf{\Sigma}_k^H = \mathbf{\Sigma}_k^H(\vec{\sigma}_k^{\text{opt}})$, as parametrized in (3.12). We refer to $\bar{c}(\vec{\sigma}_k)$ as the *local upscaling criterion*. In this case, our formulation is a type of extended upscaling procedure within the classification of upscaling techniques proposed in [49, 56].

Once again, the parameter estimation problem (3.17) satisfies that the number of parameters is less than (or equal) to the number of data and it is a well-posed least-squares problem, hence no additional regularization is required.

In order to solve the discrete optimization problem (3.17) using a gradient based optimization method (see [107, 117, 137] for details), we first compute the gradient and an approximation to the Hessian of the local upscaling criterion $\bar{c}$ as discussed in [68]. The gradient of the local upscaling criterion (3.17) is given by

$$\nabla \bar{c}(\vec{\sigma}_k) = \sum_{l=1}^{12} \text{Real}\left(\mathbf{J}_l^*(\vec{\sigma}_k)\left[\mathbf{d}_l\big(\overline{\mathbf{\Sigma}}_k^H(\vec{\sigma}_k)\big) - \mathbf{d}_l\big(\mathbf{\Sigma}_k^h\big)\right]\right), \qquad (3.18)$$

where $\mathbf{J}_l$ represents the lth sensitivity matrix defined as the Jacobian resulting after deriving the lth residual, $\mathbf{d}_l\big(\overline{\mathbf{\Sigma}}_k^H(\vec{\sigma}_k)\big) - \mathbf{d}_l\big(\mathbf{\Sigma}_k^h\big)$, with respect to $\vec{\sigma}_k$, and $*$ denotes the conjugate transpose operator. Since each sensitivity matrix has dimensions 12 $\times$ number of data (e.g. 12 $\times$ 6 or 12 $\times$ 12), we can compute them explicitly.

The Gauss-Newton approximation to the Hessian of the local upscaling criterion (3.17) is given by

$$\mathbf{H}_{\bar{c}}(\vec{\sigma}_k) \approx \sum_{l=1}^{12} \text{Real}\big(\mathbf{J}_l^*(\vec{\sigma}_k)\,\mathbf{J}_l(\vec{\sigma}_k)\big). \qquad (3.19)$$

where $\mathbf{J}_l$ is the lth sensitivity matrix defined as before.

The pseudo-code in Algorithm 1 summarizes the steps to compute an upscaled conductivity $\mathbf{\Sigma}_k^H$ in the coarse cell Ω_k^H when a discrete fine-mesh conductivity model $\mathbf{\Sigma}^h$ is given. Observe that all the calculations are done in $\Omega_k^{H,\text{ext}}$, where each optimization problem is small and can be solved quickly. Furthermore, since the problem defined for each coarse cell is independent, the upscaling procedure

---

Algorithm 1 Computation of the upscaled conductivity $\mathbf{\Sigma}_k^H$ in the coarse cell Ω_k^H:

1: Choose the size of the extended local domain $\Omega_k^{H,\text{ext}}$ (Figure 3.4) where the coarse cell, Ω_k^H, is embedded.

2: Compute sets of discrete fine and coarse EM responses using the fine-mesh conductivity in $\Omega_k^{H,\text{ext}}$. To do so, forward model the twelve local Maxwell's problems (3.13)-(3.15) defined on $\Omega_k^{H,\text{ext}}$ using the MFV method as outlined in Section 2.4. This yields the sets of discrete electric fields $(\mathbf{E_k} = \{\mathbf{e_1^k}, \ldots, \mathbf{e_{12}^k}\})$ and magnetic fluxes $(\mathbf{B_k} = \{\mathbf{b_1^k}, \ldots, \mathbf{b_{12}^k}\})$.

3: Choose the type of data to be matched in the local upscaling criterion (3.17) according to the context of the given simulation. That is, chose either the set of total electric fields as defined in (3.16a), or the set of total magnetic fluxes as defined in (3.16b). Compute the fine and coarse data to be matched using the discrete fields and fluxes obtained in the previous step.

4: Optimize the constrained parameter estimation problem (3.17) to obtain the desired anisotropic upscaled conductivity $\mathbf{\Sigma}_k^H$. Depending on the choice of the optimization method to solve this problem, this step may require the computation of the gradient (3.18), and/or the Hessian approximation (3.19). Note that solving such an optimization problem involves performing steps 2 and 3 (for the upscaled conductivity model $\overline{\mathbf{\Sigma}}_k^H$) to compute $\mathbf{d}_l(\overline{\mathbf{\Sigma}}_k^H)$ at each iteration.

---

can be done in parallel.

Once all the upscaled conductivities are computed, we assemble the coarse-mesh conductivity model. Using this coarse conductivity model, the original problem can then be discretized and solved on the coarse mesh using a traditional discretization approach, such as the MFV method (Section 2.4).

Remarks

1. Observe that the upscaled conductivity constructed using formulation (3.17) can result in a SPD diagonal matrix or a full matrix depending on the problem. That is, the formulation leads to the appropriate form of the best upscaled conductivity (in the sense of equation (3.17)) for the problem at hand. This feature of the proposed upscaling formulation can be advantageous as for some averaged-based upscaling methods proposed for flow in porous media problems this is not the case. For example, two-point flux approximation upscaling methods assume that the upscaled quantity is a diagonal

matrix. This assumption may not be sufficient to obtain an accurate solution in the situations where a full-tensor is more appropriate. For those cases, full-tensor effect or full anisotropy of the upscaled permeability can be achieved by post-processing the diagonal tensor using fine-mesh information where care must be taken to preserve the symmetry of the matrix [35, 36, 49, 56].

2. The proposed upscaling formulation (3.17) can be extended to construct complex anisotropic conductivities as well. One way to do so is by adapting the parametrization of the upscaled conductivity given by (3.12) accordingly and solving the resulting optimization formulation in a similar manner as described before. That is, rather than using six scalars to parametrize $\mathbf{\Sigma}_k^H$, we use twelve scalars where six of them are used to define the real part of $\mathbf{\Sigma}_k^H$ and the other six scalars define the imaginary part of $\mathbf{\Sigma}_k^H$. Using such parametrization leads to a real optimization problem with a similar optimization formulation as before where $\vec{\sigma}_k \in \mathbb{R}^{12}$ and $\mathrm{Real}(\mathbf{\Sigma}_k^H(\vec{\sigma}_k))$ should be SPD. The computation of the discrete data to be matched in the upscaling criterion can be done in a similar manner as described before; however, the interested reader can find more detailed information on how to compute EM fields when the electrical conductivity is a complex quantity in [68].

3. The data to be matched by the local upscaling criterion (3.17) can also be chosen among the total magnetic fields, or the total electric fluxes on $\partial \Omega_k^H$. The total magnetic field can be computed as the integral of the magnetic field, $\vec{H}$, over the twelve edges of $\partial \Omega_k^H$ (i.e., replace $\vec{E}$ with $\vec{H}$ in (3.16a)). The total electric flux can be computed as the integral of the electrical current density, $\vec{J}$, over the six faces of $\partial \Omega_k^H$ (i.e., replace $\vec{B}$ with $\vec{J}$ in (3.16b)). The discretization of the magnetic field and the electrical current density can be done using the $\vec{H}$-$\vec{J}$ formulation of the quasi-static Maxwell's equations and the MFV in a similar way as described in Section 2.4 for the $\vec{E}$-$\vec{B}$ formulation. In Section 3.5.1, we show two examples that use total magnetic and electric fluxes to compute upscaled electrical conductivities on a single coarse cell.

3.5 Numerical Results in 3D

In this section, we demonstrate the performance of the local upscaling framework proposed in Section 3.4 by simulating EM responses for two 3D settings. The first setting illustrates the use of the framework to upscale fine-scale conductivity structures on a single coarse-mesh cell, and the impact that the choice of the upscaling criterion has on the resulting upscaled quantity. The second setting demonstrates how the framework can be combined with an adaptive mesh refinement technique to construct anisotropic, coarse-mesh conductivity models for a large-loop EM survey of a mineral deposit on a geologically-rich background.

3.5.1 Simulations on a Single Coarse-mesh Cell

We demonstrate the upscaling procedure and the impact of the choice in upscaling criterion on a single coarse-mesh cell. To do so, we use two electrical conductivity models: one of an isolated conductive block on a resistive background, and one of a conductive sheet on a resistive background. These conductivity models are visualized in Figure 3.6 (a) and (b), respectively.

In both examples, the local upscaling domain is given by a cuboid coarse-mesh cell with dimensions $(100 \text{ m})^3$. We denote the local upscaling domain as Ω_k^H. We extend the local domain a further 50 m along each direction such that Ω_k^H is positioned in the center (Figure 3.6). This conforms the local extended domain, which we denote as $\Omega_k^{H,\text{ext}}$. Note that the local extended domain has dimensions $(200 \text{ m})^3$.

We discretize the local extended domain using uniform fine-mesh cells, which are $(12.5 \text{ m})^3$. Hence, the total number of fine cells in $\Omega_k^{H,\text{ext}}$ is 16^3, and in Ω_k^H is 8^3. As discussed in Section 3.4, we assume the fine-scale conductivity model to be isotropic and the upscaled conductivity to be anisotropic in the coarse cell we aim to upscale. The magnetic permeability takes its free space value, namely $\mu = 4\pi \times 10^{-7}$ Vs/Am.

To construct an anisotropic upscaled conductivity using the upscaling criterion (3.17), we must first select the data to be matched on it. For the following two examples, we consider two types of data: the total magnetic flux on each of the six faces of Ω_k^H, and the total current density flux on each of the six faces of Ω_k^H.
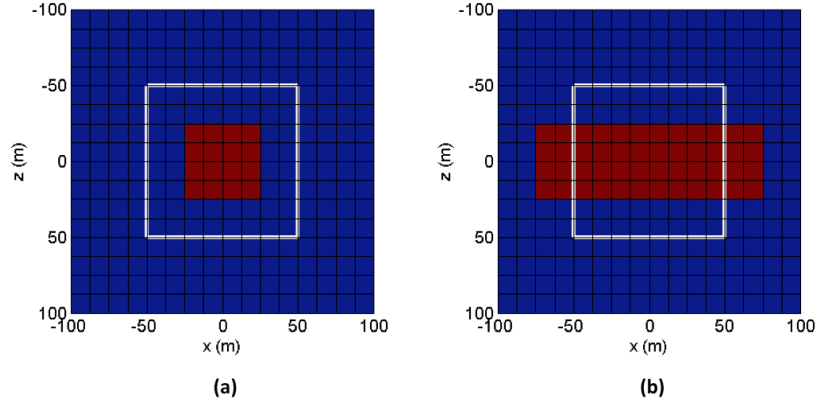
Figure 3.6: Cross sections of the fine scale conductivity model for (a) the isolated block and (b) the sheet. Conductive bodies are displayed in red. The resistive background is displayed in blue. The coarse-mesh cell, Ω_k^H, which we aim to upscale is outlined in white.

The total flux (either current density or magnetic field) over each face is defined as the surface integral of the flux through that face (see (3.16b)). Throughout this section, we say that we use the $\mathbf{b}-$criterion when the data to be matched in the upscaling criterion (3.17) are total magnetic flux. Similarly, we say that we use the $\mathbf{j}-$criterion when the data to be matched in the upscaling criterion (3.17) are total current density flux.

Once we selected the necessary elements to setup the local upscaling framework proposed in Section 3.4, let us see how the framework performs for the two conductivity models we are interested in.

Conductive Block in a Resistive Background

First, we study the case of an isolated conductive block in a resistive background. To setup this example, we assume that at the center of Ω_k^H there is a $(50 \text{ m})^3$ conductive block, as shown in Figure 3.6(a). The surrounding material is resistive (10^{-4} S/m). We use a frequency of 1 Hz and consider three different electrical conductivities of the block: 10^{-2}, 10^{-1} and 1 S/m.

Following Algorithm 1, next we need to solve the optimization problem (3.17)

66

to construct anisotropic upscaled conductivities, as defined in equation (3.12), for the **b**−criterion and **j**−criterion, and each of the three conductivity values of the block, respectively. The initial conductivity model, $\vec{\sigma}_0$, is given by a 3×3 diagonal matrix with all its main diagonal entries being equal to the geometric mean of the fine-mesh conductivity in Ω_k^H. We choose the geometric mean as it is often used to approximate the homogenized permeability for fluid flow problems with random heterogeneous media with reasonable accuracy [163].

In order to solve the constrained optimization problem (3.17), we tested both a projected steepest descent and a projected Gauss-Newton method (see [68, 137]). Both methods were implemented with a backtracking line search. The projection in this case consisted of computing the eigenvalues of the 3×3 matrix defined by (3.12) after $\vec{\sigma}_k$ was computed at each iteration to ensure the positive definiteness of such matrix. When necessary, the nonpositive eigenvalues of such matrix were modified to be positive. For both optimization methods, the iteration was halted when

$$\|\vec{\sigma}_k - \vec{\sigma}_{k+1}\|_2 < 10^{-8} \ \text{ or } \ \|\nabla \overline{c}(\vec{\sigma}_k)\|_2 < 10^{-8} \|\nabla \overline{c}(\vec{\sigma}_0)\|_2. \tag{3.20}$$

Although the use of the projected Gauss-Newton method lacks theory for convergence in this case, in practice we observe that this method reaches results similar to those obtained with the projected steepest descent method but in a much faster way. For this reason, we decided to use the projected Gauss-Newton method to carry out the simulations.

For each of the three conductivity values considered, the resulting upscaled conductivities are diagonal matrices with all diagonal entries being equal. This result is expected due to the symmetry of the fine-mesh conductivity model. When using the **b**−criterion, the stopping criterion (3.20) was fulfilled for each of the three conductivity values of the block considered after 18, 4 and 26 iterations, respectively. When using the **j**−criterion, the stopping criterion (3.20) was fulfilled for each of the three conductivity values of the block considered after 17, 14 and 20 iterations, respectively. The values of the main diagonal entries of each of upscaled conductivity are shown in Figure 3.7.

Clearly, there is a large discrepancy between the upscaled conductivities con-

67
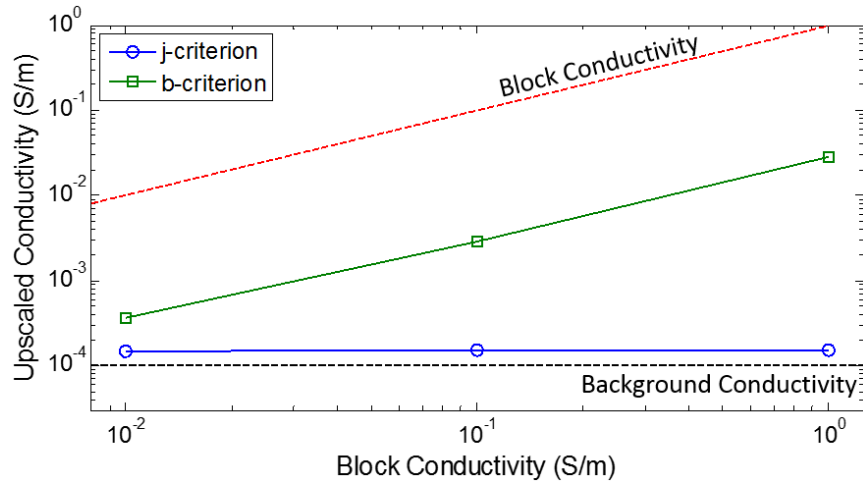
Figure 3.7: Upscaled conductivity results found using the **b** and **j** criteria for the conductive block model. Note that the upscaled conductivity in this case can be defined by a scalar, as the matrix recovered was diagonal, with all diagonal elements being equal.

structed using the **b**− and **j**− upscaling criteria for each of the three block conductivities. Physically, this discrepancy can be reconciled by recognizing that the current density and magnetic flux density reflect different physical processes. Current is the flow of electrical charges through a material. In the case of a conductive block in a resistive background, the current must be driven through the resistive background irrespective of the conductivity of the block. Thus, the resistive background dominates the upscaled conductivity constructed using the **j**-criterion. On the other hand, magnetic flux is produced as a result of induced currents. Currents can be induced in the conductive block regardless of the conductivity of the background. Therefore, we see that the conductivity of the block dominates the upscaled conductivity recovered using the **b**-criterion.

Conductive Sheet in a Resistive Background

Next, we examine the case of a conductive sheet in a resistive background positioned at the center of Ω_k^H, as shown in Figure 3.6(b). The sheet has dimensions 150 m $\times$ 150 m $\times$ 50 m. It is stopped short of the boundary of the coarse cell

in order to avoid applying the boundary conditions directly on the sheet. For this simulation, we also use a frequency of 1 Hz.

Now that the model is no longer identical in each direction, we expect to construct an anisotropic upscaled conductivity, as defined in (3.12), where $\sigma_1 = \sigma_2$ which is distinct from σ_3.

Typically, one would draw the analogy between layered conductors and a simple circuit model. In this case, we would expect that the components of the upscaled conductivity matrix, σ_1 and σ_2 would conform closely the approximation of conductors in parallel, while σ_3 would be similar to the approximation of conductors in series. Note however, that this approximation accounts for only one physical behavior: galvanic current flow, to which the **j**-criterion is sensitive. It does not account for any inductive currents, to which the **b**-criterion is sensitive.

To investigate, we again assign the electrical conductivity of the background to be 10^{-4} S/m and examine three conductivities for the sheet: 10^{-2}, 10^{-1} and 1 S/m. Using both the **b**$-$ and **j**$-$ criteria, we perform the upscaling process as indicated in Algorithm 1, and recover the upscaled conductivities shown in Figure 3.8.

To obtain the results described above we use the stopping criterion (3.20) and the same initial conductivity model ($\vec{\sigma}_0$) as before. We also run the simulations using both projected steepest descent and projected Gauss-Newton methods. Once again, we notice that the results obtained with projected Gauss-Newton are similar to those obtained with projected steepest descent, but the convergence when using projected Gauss-Newton is faster. When using the **b**$-$criterion, the stopping criterion (3.20) was fulfilled for each of the three conductivity values of the sheet considered after 24, 54 and 142 iterations, respectively. When using the **j**$-$criterion, the stopping criterion (3.20) was fulfilled for each of the three conductivity values of the sheet considered after 29, 67 and 181 iterations, respectively.

As expected, the resulting upscaled conductivity is a diagonal SPD matrix with two unique entries: $\sigma_1 = \sigma_2$ and σ_3 (see (3.12)). Figure 3.8(a) shows the $\sigma_1 = \sigma_2$ entries of the matrix, and Figure 3.8(b) shows the σ_3 entry. The values constructed using the **j**-criterion conform well to the parallel and series circuit approximations for $\sigma_1 = \sigma_2$ and σ_3, respectively. For each scenario the value for σ_3 constructed using the **j**-criterion is nearly identical to the resistive background,
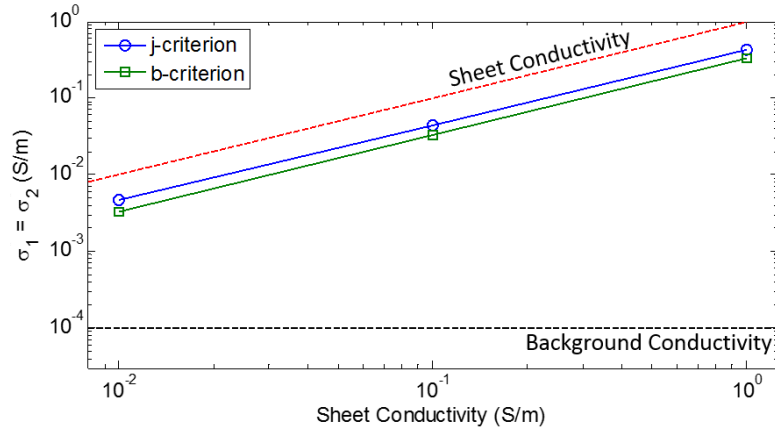
(a)
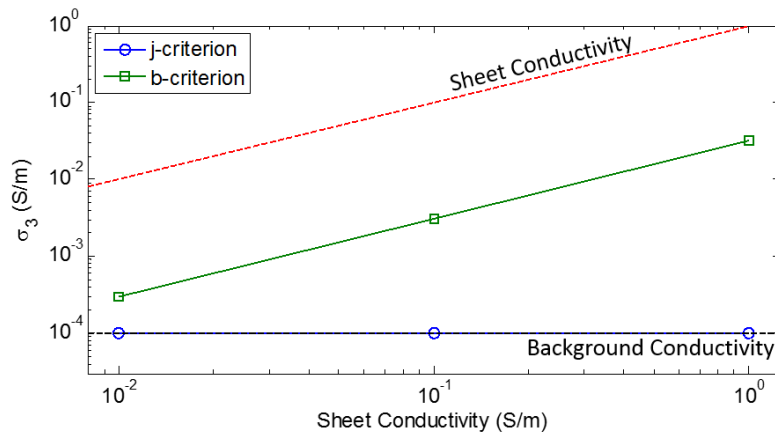
(b)

Figure 3.8: Upscaled conductivity results found using the **j** and **b** criteria for the conductive sheet. Since the upscaled conductivity is a diagonal 3×3 SPD matrix, it can be described by two positive scalars: $\sigma_1 = \sigma_2$ and σ_3. $\sigma_1 = \sigma_2$ is shown in plot (a), and σ_3 is shown in plot (b).

as is to be expected using a series circuit approximation. Similar to the block model results, this is as a consequence of having to drive the current through the resistive background in the z direction, regardless of the conductivity of the sheet. On the other hand, for the entries σ_1 and σ_2, the conductivity of the sheet has a

large impact on the value we construct. In this case, the conductive sheet forms a connected pathway from one side of the cell we aim to upscale to the other along both horizontal directions. As a result, current is channeled along this pathway, causing the conductivity of the sheet to have a large impact on the σ_1 and σ_2 entries of the upscaled conductivity, as shown in Figure 3.8.

Using the **b**-criterion, we see that the conductivity of the sheet has a significant impact on both the $\sigma_1 = \sigma_2$ (Figure 3.8(a)) entries and the σ_3 entry (Figure 3.8(b)), contrary to the parallel-series circuit approximations. This is again because the magnetic flux density is sensitive to inductive currents. Since the sheet has a finite thickness, these currents can be induced in any direction, and therefore contribute to the upscaled values σ_1, σ_2 and σ_3 we construct using the **b**-criterion.

Lessons Learned

As discussed in the block and sheet examples, the current density and magnetic flux density each sample the conductivity structure differently, and are therefore sensitive to different features of the fine-mesh conductivity model. As a result, the constructed upscaled conductivities using either upscaling criteria may vary over orders of magnitude. Therefore, for a given fine-scale conductivity structure, there is not a unique upscaled conductivity which completely describes it.

3.5.2   Simulations Using the Synthetic Lalor Model

In this section, we demonstrate how to use the upscaling framework introduced in Section 3.4 in combination with an adaptive mesh refinement technique to construct anisotropic, coarse-mesh electrical conductivity models from a given fine-scale conductivity model of a mineral deposit. We use these coarse-mesh conductivity models to predict magnetic field data for a large-loop EM survey. Since no analytical solutions are available for this example, we compare our results with those obtained on a fine mesh. We also compare our results with those obtained from applying simple average-based upscaling approaches.

We construct a synthetic electrical conductivity model based on the inversion results of EM field measurements over the Canadian Lalor mine obtained by [177]. The Lalor mine targets a large zinc-gold-copper deposit that has been the subject

71
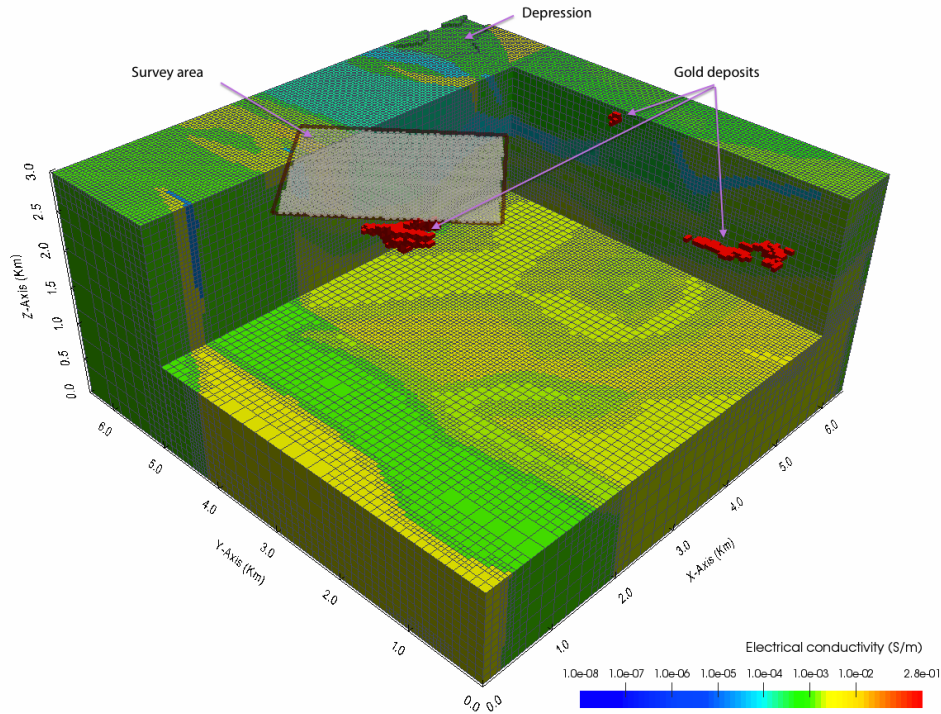
Figure 3.9: Subsurface part of the synthetic electrical conductivity Lalor model and large-loop EM survey setup. The model is discretized on a fine OcTree mesh with 546,295 cells. The conductivity varies over five orders of magnitude throughout the whole model.

of several EM surveys. The synthetic conductivity model, shown in Figure 3.9, has an area with non-flat topography and extends from 0 to 6.5 km along the x, y and z directions, respectively. The model comprises air and the subsurface that is composed of 35 geologic units. The unit with the largest conductivity value represents the mineral deposit, which is composed of three bodies. We assume a conductivity of 10^{-8} S/m in the air. The subsurface conductivity values range from 1.96×10^{-5} to 0.28 S/m. We assume that the magnetic permeability takes its free space value, namely $\mu = 4\pi \times 10^{-7}$ Vs/Am.

We consider a frequency-domain, large-loop EM survey, where we use a rectangular transmitter loop with dimensions 2 km $\times$ 3 km, operating at the frequencies of 1 and 20 Hz. The transmitter is placed on the earth's surface and it is

centered above the largest body of the mineral deposit, as shown in Figure 3.9. Inside the loop, we place a uniform grid of receivers that measure the three components of the magnetic flux ($\vec{B} = [B^x, B^y, B^z]^\top$). The receivers are separated by 50 m along the x and y directions, respectively. To reduce the effect of the imposed natural boundary conditions (2.5), we embed the survey area into a much larger computational domain, which replaces the true decay of the fields towards infinity (Figure 3.9).

We discretize the synthetic Lalor electrical conductivity model using a staggered fine OcTree mesh, which allows for an adaptive local refinement of the mesh where the electrical conductivity and the EM responses vary drastically. We base the estimate for the proper cell sizes of the mesh on the skin depth [169]. Practical experience on mesh design for EM problems reported in [68] suggests that the smallest cell size in the mesh should be a quarter the minimum skin depth. We consider the largest background conductivity value (4.5×10^{-3} S/m) and calculate skin depths of 7,498 and 1,677 m for the frequencies of 1 and 20 Hz, respectively. Hence, we use cells of size $(50 \text{ m})^3$ within the survey area and at the interfaces of the model where the conductivity varies, the rest of the domain is padded with gradually increasing OcTree cells. The fine OcTree mesh is illustrated in Figure 3.9. This mesh has 546,295 cells.

We aim to estimate the *secondary magnetic flux induced by the ground* in the survey area. For this purpose, we simulate two sets of the magnetic flux data for each frequency. The first data set considers the conductivity model including all geologic units, and the second data set considers the conductivity model of a halfspace with an earth conductivity of 10^{-2} S/m. Each of these two data sets consists of the measurements of $\vec{B}$ taken at the receiver locations. The secondary magnetic flux induced by the ground at the survey area, denoted as $\Delta\vec{B}$, is then computed by subtracting the two data sets.

In order to construct a single anisotropic, coarse-mesh conductivity model using the upscaling methodology introduced in Section 3.4, we need to choose the following parameters: (a) a suitable coarse mesh, (b) the size of the extended local domain, and (c) the data to be matched in the upscaling criterion (3.17).

As a coarse mesh, we consider an OcTree mesh that is nested within the fine OcTree mesh previously described. Since we are interested in accurately

73
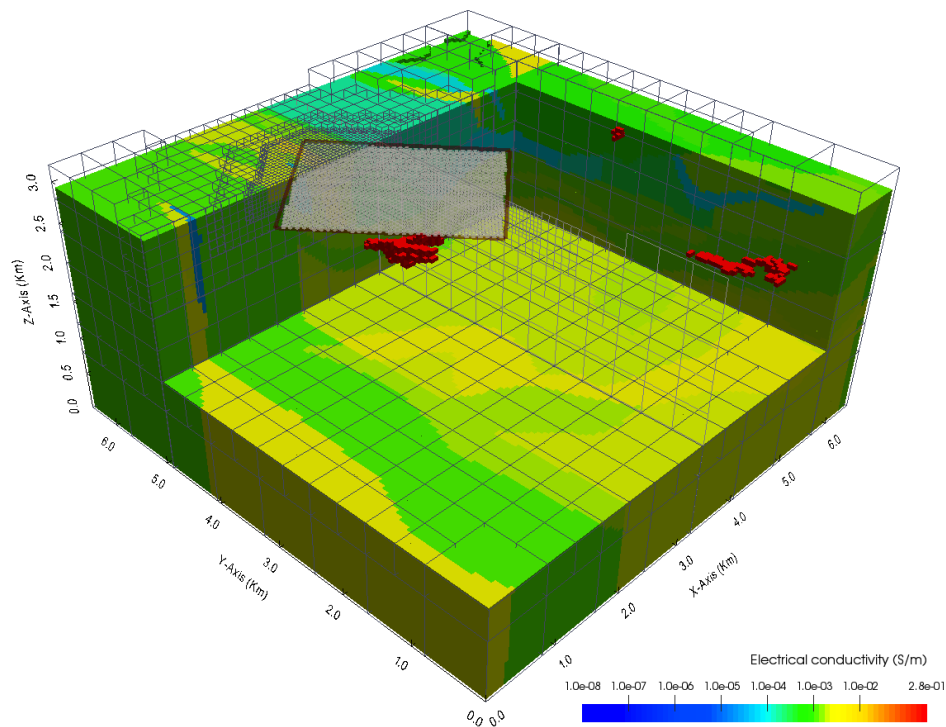
Figure 3.10: Subsurface part of the synthetic electrical conductivity Lalor model and large-loop EM survey setup. The model is discretized on a coarse OcTree mesh with 60,656 cells. The conductivity varies over eight orders of magnitude throughout the whole model.

simulating magnetic flux data in the survey area, the OcTree mesh is designed to maintain the fine mesh resolution of $(50 \text{ m})^3$ inside the area of interest, whereas the rest of the domain is filled with increasingly coarser cells. In total it contains only 60,656 cells — this number of cells is roughly 10% of the number of cells in the fine OcTree mesh. Figure 3.10 shows the coarse OcTree mesh. Note that the coarse mesh is not refined outside the survey area where a large conductivity contrast is present in the model. For example, at the interface between the highly conductive gold units and the more resistive background, and at the air-earth interface which contains a not flat area. These interfaces are not represented in the coarse OcTree mesh. We challenge the upscaling procedure with the large conductivity contrast across the subsurface interfaces.

Next, we need to choose the size of the extended domain to solve the local Maxwell problems, that is, the number of fine-mesh padding cells by which we extend every coarse cell to be upscaled as shown in Figure 3.4. To investigate the effect of this size on the resulting upscaled conductivity, we performed the extension using the sizes of 4 and 8 padding cells. These local extended domain sizes extend each $(200 \text{ m})^3$-coarse cell by one and two coarse cells, respectively. The $(200 \text{ m})^3$ cells are the majority of the coarse cells where the largest conductivity contrast happens in this setting (Figure 3.10).

Since the receivers measure magnetic flux data, we consider the total magnetic flux as defined in (3.16b) through each of the faces of the coarse cell to be upscaled as the data to be matched by the upscaling criterion (3.17). By doing so, we have connected the upscaling criterion to the large-loop EM survey configuration.

Once the necessary elements to setup the upscaling framework are selected, the construction of the desired coarse-mesh conductivity models is completed by solving the constrained parameter estimation problem (3.17) for each of the coarse cells separately, each individual size of the extended domain, and each individual frequency. Each individual parameter estimation problem is solved as indicated in Algorithm 1. To solve each local parameter estimation problem we use the same stopping criterion and optimization parameters as described in the previous section.

Next, we use the coarse conductivity models obtained previously to estimate $\Delta \vec{B}$. To do so, we apply the MFV discretization method on the described coarse OcTree mesh as outlined in [72, 86]. This discretization yields linear systems of equations with 169,892 edge degrees of freedom (DOF), which we solve using the parallel sparse direct solver MUMPS [3]. The total average run times per single simulation for extended domain sizes of 4 and 8 padding cells are 5.3 h and 3.7 days, respectively, on a two hexa-core Intel Xeon X5660 CPUs at 2.8 Hz with 64 GB shared RAM using the parallel computing toolbox of MATLAB ([162]). The right-hand panel of Figure 3.11 shows the magnitude of $\Delta \vec{B}$ obtained for the frequencies of 1 and 20 Hz for the extended domain size of 8 padding cells.

To evaluate the accuracy of our results, we compute a reference (fine-mesh) solution. To do so, we apply the MFV method on the described fine OcTree mesh

(Figure 3.9) as discussed in [72, 86]. This yields linear systems of equations with roughly 1.5 millions DOF, which we also solve using MUMPS. The average computation time per single simulation is 704.5 s on the same machine. The left-hand panel of Figure 3.11 shows the magnitude of $\Delta\vec{B}$ obtained for the frequencies of 1 and 20 Hz.

We also carry out MFV forward modeling simulations using homogenized electrical conductivity models that we construct using volume-arithmetic, -geometric and -harmonic averaging of the fine-mesh conductivity inside each coarse cell of the OcTree mesh shown in Figure 3.10. The total average run time per single simulation is 125.5 s on the same machine.

Table 3.4 shows the relative errors in Euclidean norm for the magnitude of $\Delta\vec{B}$ obtained from comparing the reference (fine-mesh) solution with the different homogenized solutions for each frequency and local extended domain size. The relative error is computed as the ratio of the norm of the difference in magnitude of the fine- and coarse-mesh data to the norm of the fine-mesh data in magnitude.

Table 3.4: Relative errors in Euclidean norm for the magnitude of the secondary magnetic fluxes induced by the ground in the survey area, $\Delta\vec{B}$. The relative errors are given in per cent.

Conductivity model	1 Hz	20 Hz
Arithmetic	9.028	1.534
Geometric	8.990	0.594
Harmonic	8.987	0.403
Upscaling (4 padding cells)	8.989	0.532
Upscaling (8 padding cells)	8.991	0.383

From Table 3.4 we see that while upscaling has an effect when using 20 Hz data, the effect is smaller when considering the 1 Hz data. This should not come as a surprise, as the fields at 1 Hz are mainly in the real component, and are less sensitive to fine-scale variations in conductivity than at 20 Hz. Indeed, for the Magnetostatic case, the magnetic fields are conductivity independent [68]. As a result, the error that we observe in this frequency is mostly due to discretization error. However, when considering 20 Hz, the effect of using an appropriate aver-

aging scheme is more evident and in fact, our averaging scheme does better than other averaging schemes. Nonetheless, for this case, it is surprising to see how well simple harmonic averaging did. We suspect that, unlike the 1D case where harmonic averaging performs poorly, the 3D conductivity model requires averaging over a much smaller, local area which leads to a much smaller difference in the data.
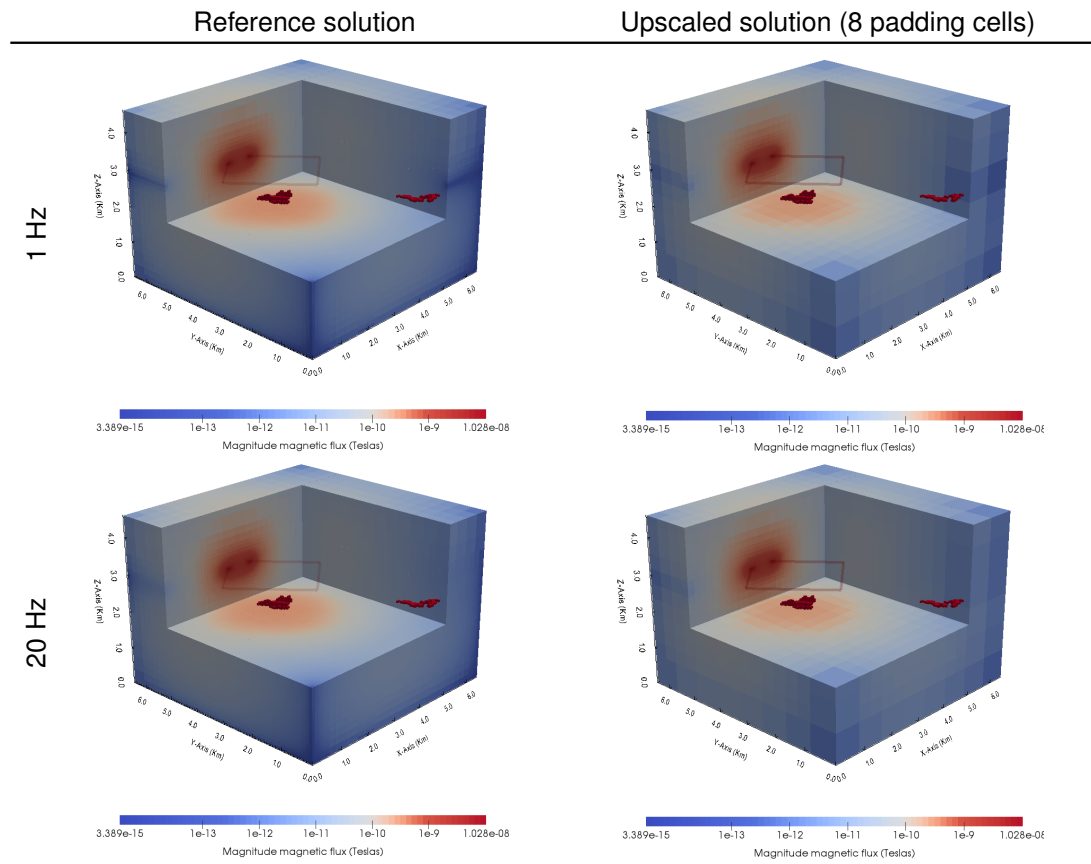
Figure 3.11: Magnitude of the secondary magnetic flux induced by the ground in the survey area, Δ, for the large-loop EM survey configuration. First and second rows show the results for 1 and 20 Hz, respectively. The left-hand panel shows the reference solution computed using the MFV method on the fine OcTree mesh with 546,295 cells. The right-hand panel shows the upscaled solution computed using 8 padding cells on the coarse OcTree mesh with 60,656 cells.

3.6 Discussion

The global and local upscaling formulations proposed in this chapter are appropriate in different situations. For example, Section 3.3 shows the benefit of using the global upscaling formulation (in 1D) when upscaling well log conductivity data. On the other hand, Section 3.5.1 shows the benefit of using the local upscaling formulation to construct 3D anisotropic coarse-mesh conductivity models for a large-loop EM survey of a mineral deposit. This investigation supports the remarks made in the field of fluid flow problems regarding the use of upscaling methods (cf. [49]): the upscaling formulation to use on a particular problem depends on the simulation question being addressed and the level of detail that can be accommodated in the coarse conductivity model.

The 1D and 3D experiments presented show that the coarse-mesh models constructed with the proposed upscaling framework yield accurate approximations to the EM responses that are comparable to those obtained by using MFV on a fine mesh in the forward modeling process, and that the size of the problem can be reduced significantly, specially when upscaling is combined with an adaptive mesh refinement technique, such as OcTree. For the examples presented, the size of the coarse-mesh system solved was roughly 10% of the fine-mesh system size, while the relative errors (in the secondary fields) were less than 5%. That is, the coarse conductivity models are able to emulate the behavior of the heterogeneity present in the prescribed fine-mesh electrical conductivity model.

The 3D local upscaling framework has two main issues. First, it constructs an upscaled conductivity that depends significantly on the set of boundary conditions imposed to compute the synthetic data used in the upscaling criterion. This issue is consistent with what has been reported in the upscaling procedures developed in the community that simulates flow in porous media [49, 56, 175]. I use the set of standard bilinear decaying functions on a coarse cell as the set of boundary conditions based on the arguments described in Section 3.4. I recognize that such a set of boundary conditions may not be the most appropriate for constructing accurate coarse models for all cases. However, for the experiments presented, these boundary conditions give reasonable estimates. Second, the proposed upscaling method is more computationally expensive than simple average-based upscaling

methods, as one solves a local optimization problem in each coarse cell. However, since each local problem is formulated independently of the others, one can reduce the cost by using a more efficient parallel implementation of the method on a more powerful machine.

3.7   Summary

This chapter proposes a least-squares formulation for the upscaling problem and develops a numerical framework to construct accurate coarse-mesh electrical conductivity models based on prescribed fine-mesh ones for a broad range of quasi-static EM geophysical problems in the frequency domain. In practice, simulating these types of problems is computationally expensive; they often consider highly heterogeneous geologic media that require a very large and fine mesh to be discretized accurately.

In the proposed framework, we pose upscaling as a parameter estimation problem. Thus, a coarse-mesh electrical conductivity model is obtained by solving an optimization problem for each coarse-mesh cell. The optimization criterion (i.e., upscaling criterion) can be customized to construct isotropic or fully anisotropic real or even complex upscaled quantities to approximate any of the EM fields and/or fluxes depending on the geophysical EM experiment of interest. The computation of the upscaled conductivity can be done in a global or an extended setting. Contrary to other least-squares upscaling formulations in the literature for fluid flow problems, the formulation proposed in this investigation does not require regularization and it is practical to tackle 3D geophysical EM problems with arbitrary electrical conductivity structures.

The upscaling framework demonstrates that the construction of upscaled quantities should be specific to, and highly dependent on, the purpose of the simulation and the EM experiment configuration. In fact, this investigation shows that different EM experiments use different upscaling criteria that result in different upscaled quantities. The proposed upscaling formulation is a reflection of the fact that an upscaled quantity is a property that one constructs, and it will take on different values, depending on how one formulates the problem. The choices of the EM responses of interest, boundary conditions, and type of the upscaled quan-

tity employed (i.e., isotropic or anisotropic) all influence the nature of the resulting upscaled conductivity model. As a result, for a given fine-scale conductivity structure, *there is no unique upscaled model which completely describes it*. I believe that the proposed framework can be used to tackle upscaling problems with a different perspective when care is taken to properly define the upscaled quantity needed.

This investigation demonstrates that upscaling methods can be used for solving frequency-dependent, quasi-static EM geophysical problems with highly discontinuous electrical conductivity, especially given the work done on improving the computation performance and accuracy of the proposed framework. Simultaneously, Haber and Ruthotto ([73]) showed that multiscale techniques are also a feasible method to tackle this problem with some additional advantages. Multiscale methods are further investigated in the next chapter.

Chapter 4

A Multiscale Finite Volume
Method with Oversampling

Every pawn is a potential queen. — James Mason

4.1 Overview

This chapter[1] proposes a multiscale FV method with oversampling for faster sim-
ulation of the quasi-static EM responses on a coarse mesh.

The main contribution of this chapter is to show how the core mathemati-
cal concepts used to develop oversampling techniques for flow in porous media
problems can be extended to geophysical EM problems, as well as to show how
multiscale techniques can be combined with OcTree in a parallel environment to
tackle more challenging geophysical EM simulations.

This chapter starts by providing a summary of the multiscale FV method pro-
posed by Haber and Ruthotto [73] for geophysical EM problems. Then, the pro-
posed oversampling technique for such method is developed. Finally, the perfor-
mance of the multiscale FV with oversampling method is demonstrated by using
two 3D synthetic electrical conductivity models: a) the Lalor model, and b) one

---

[1]This chapter contains extended and revised versions of the material published in [30], [31] and
[33]. I am the lead author in all of these publications.

with a random isotropic heterogeneous medium. Both examples show the feasibility of combining the proposed multiscale FV with oversampling method with OcTree meshes in a parallel environment to boost its performance.

4.2 An Overview of the Multiscale Finite Volume Method

Haber and Ruthotto ([73]) adapted the general lines proposed by Hou and Wu ([89]), Jenny et al., ([101]), and MacLachlan and Moulton ([123]), where multiscale FE and FV methods are developed for elliptic problems with strongly discontinuous coefficients, to develop a multiscale finite volume method (MSFV) that fits the staggered discretization of vector fields typically used in the MFV discretization method introduced in Section 2.4. Since we use the MSFV method as a building block for the oversampling technique we propose in this work, we provide next an overview of this method, which can be summarized in the following four steps (Figure 4.1).
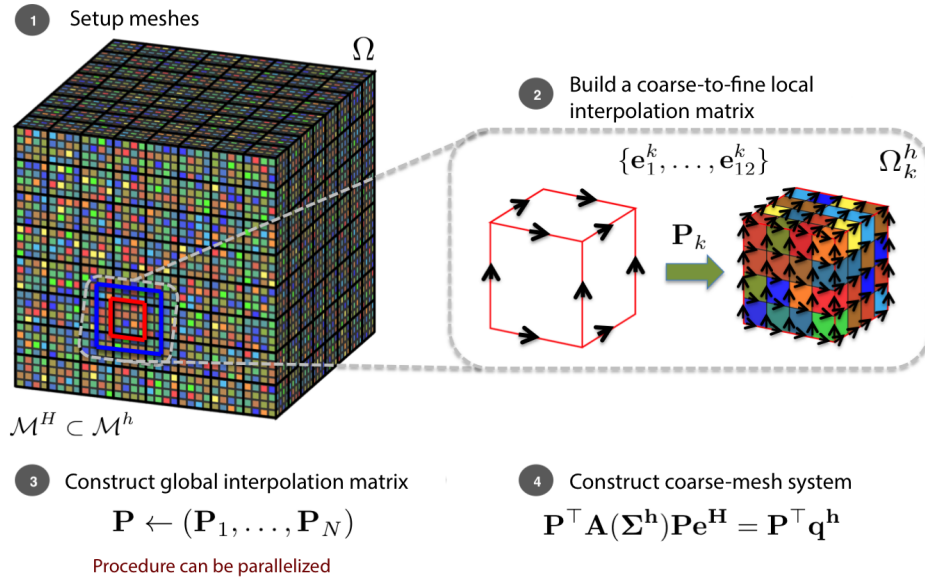
Figure 4.1: Schematic representation of the procedure to implement the MSFV method.

First, let us assume a coarse mesh, $\mathcal{M}^H$, nested into a fine mesh, $\mathcal{M}^h$, i.e., $\mathcal{M}^H \subset \mathcal{M}^h$ (Step 1 in Figure 4.1). $\mathcal{M}^h$ accurately discretizes the features in the model where the electrical conductivity varies, and $\mathcal{M}^H$ is a user-chosen mesh that is typically much coarser than the fine mesh and satisfies the guidelines for mesh design in the areas where the EM responses are measured. In particular, $\mathcal{M}^H = \cup_{k=1}^N \Omega_k^H$, where N is the number of coarse-mesh cells and Ω_k^H denotes the kth coarse-mesh cell; $\mathcal{M}^h = \cup_{i=1}^n \Omega_i^h$, where n is the number of fine-mesh cells and Ω_i^h denotes the ith fine-mesh cell; and $N \ll n$. The MSFV method was originally developed for nested tensor meshes, we will show an example in Section 4.4 where we use nested OcTree meshes as the mesh setup.

Second, for each coarse-mesh cell, Ω_k^H; $k = 1, \ldots, N$, we independently solve a local version of the source-free Maxwell system subject to a set of twelve linearly independent, non-homogeneous Dirichlet boundary conditions (one for every edge of Ω_k^H) given by

$$\nabla \times \vec{E}_l^k + \iota\omega\vec{B}_l^k = \vec{0}, \text{ in } \Omega_k^H, \tag{4.1}$$

$$\nabla \times (\mu^{-1,k}\vec{B}_l^k) - \Sigma^k\vec{E}_l^k = \vec{0}, \text{ in } \Omega_k^H, \tag{4.2}$$

$$\vec{E}_l^k(\vec{x}) \times \vec{n} = \vec{\Phi}_l(\vec{x}) \times \vec{n}, \ \forall \vec{x} \in \partial\Omega_k^H, \tag{4.3}$$

with $l = 1, \ldots, 12$. Here, $\vec{x} = (x_1, x_2, x_3)$, $\partial\Omega_k^H$ denotes the boundary of Ω_k^H, $\vec{B}_l^k$, $\vec{E}_l^k$, μ^k, Σ^k, ω, ι and $\vec{n}$ are defined as before in Section 2.3; and $\vec{\Phi}_l$ is a vector function that denotes the lth Dirichlet boundary condition as defined in Table 3.3. This set of boundary conditions form the natural basis functions for linear edge degrees of freedom of a hexahedral finite element [104, 131]; therefore, they can be used to model general normal-linearly varying EM responses. From Figure 3.5, we observe that each $\vec{\Phi}_l$ takes the value 1 along the tangential direction to the lth edge of Ω_k^H and decays linearly to 0 in the normal directions to the same edge.

To numerically solve the twelve local Maxwell systems (4.1)-(4.3), we forward model them using the fine mesh contained in Ω_k^H and the MFV method as discussed in Section 2.4 (Step 2 in Figure 4.1). That is, the set of discrete solutions for the electric field, $\{\mathbf{e}_1^k, \ldots, \mathbf{e}_{12}^k\}$, can be obtained by solving twelve linear sys-

tems of the form (2.27), where each $\mathbf{e}_l^k$; $l = 1, ..., 12$, is a vector whose length equals the number of fine-mesh edges in Ω_k^H. We use the MFV method because it provides a consistent and stable discretization of the Maxwell's equations with highly discontinuous coefficients. However, other traditional edge-based discretization methods, such as FE ([104, 131]), can be used for this part as well as long as they provide a consistent, conservative and stable discretization for our Maxwell system. In this chapter, we refer to the set of discrete solutions $\{\mathbf{e}_1^k, \dots, \mathbf{e}_{12}^k\}$ as the *multiscale basis functions* for the cell Ω_k^H. The MSFV method proposed by Haber and Ruthotto ([73]) only covers the necessary steps to compute multiscale basis functions for the electric field. They do not compute basis functions for the magnetic flux, and neither do we. To see full derivation details of these multiscale basis functions, we refer the interested reader to the body of the paper [73].

Note that using formulation (4.1)-(4.3) implies that $\vec{E}_l^k$ is oscillatory at the interior of the coarse cell Ω_k^H, and that it coincides with the natural basis functions $\{\vec{\Phi}_l\}_{l=1}^{12}$ at the boundary of Ω_k^H, that is

$$\vec{E}_l^k \cdot \vec{\tau}_{\text{edge}_m} = \delta_{lm}; \quad l, m = 1, \dots, 12, \tag{4.4}$$

where $\vec{\tau}_{\text{edge}_m}$ is the unit tangent vector to the mth edge of $\partial\Omega_k^H$, and δ_{lm} is the Kronecker delta that takes the value 1 when $l = m$ and 0 otherwise. Naturally, the multiscale basis functions also satisfy these properties. It follows that the tangential components of the multiscale basis functions are continuous at the boundaries of the coarse-mesh cells.

As shown in [51, 69, 89], the multiscale basis functions can be arranged as the columns of a local coarse-to-fine interpolation matrix $\mathbf{P}_k$, that is

$$\mathbf{P}_k = \left[\mathbf{e}_1^k, \dots, \mathbf{e}_{12}^k \right], \tag{4.5}$$

for the fine-mesh electric field in Ω_k^H (Step 2 in Figure 4.1). This type of interpolation is also known as operator-induced interpolation, which was originally developed in the Multigrid community for the diffusion equation with strongly discontinuous coefficients [2, 44].

Once we have computed a local interpolation matrix for each coarse cell (4.5), the third step is to assemble a global coarse-to-fine interpolation matrix, $\mathbf{P}$ (Step 3 in Figure 4.1). The continuity of the tangential components of the multiscale basis functions at the boundaries of the coarse cells is a necessary requirement for the proper assembly of $\mathbf{P}$ in this step [51].

We point out that the calculations involved to compute the local interpolation matrices ($\mathbf{P}_k$; $k = 1, \ldots, N$) as defined in (4.5), are done locally inside each coarse cell independently of each other, hence they can perfectly be done in parallel. This greatly reduces the overhead time in constructing each $\mathbf{P}_k$ in practice.

The fourth step is to use the global interpolation matrix $\mathbf{P}$ as a projection matrix within a Galerkin approach ([51]) to construct a coarse-mesh version of the fine-mesh system (2.25) that is much cheaper to solve as follows

$$\mathbf{A}^H \mathbf{e}^H = \left(\mathbf{P}^\top \mathbf{A}^h(\mathbf{\Sigma}^h) \mathbf{P} \right) \mathbf{e}^H = \mathbf{P}^\top \mathbf{q}^h. \tag{4.6}$$

The superscripts H and h denote dependency to the coarse and fine meshes, respectively, the vector $\mathbf{q}^h$ and the system matrix $\mathbf{A}^h(\mathbf{\Sigma}^h)$ are defined as in (2.25), and $\mathbf{e}^H$ denotes the coarse-mesh electric field. To compute the coarse-mesh magnetic flux, $\mathbf{b}^H$, we use $\mathbf{e}^H$ in (2.23).

As shown in [69], the fine-mesh electric field, $\mathbf{e}^h$, can be obtained from the solution to the coarse-mesh problem as follows

$$\mathbf{e}^h = \mathbf{P} \mathbf{e}^H. \tag{4.7}$$

To compute the fine-mesh magnetic flux, $\mathbf{b}^h$, we use $\mathbf{e}^h$ in (2.23). This concludes the overview of the MSFV method proposed by Haber and Ruthotto in [73].

Note that we use the exact same formulation for the local Maxwell's problems (4.1)-(4.3) for both the MSFV method and the local upscaling method in 3D introduced in Section 3.4 (see equations (3.13)-(3.15)). Although the formulation of these local problems is the same, they differ in the context in which they were formulated. The difference is that in the local upscaling method the formulation comes from using physical arguments that describe the behavior of our problem to define the elements needed in the upscaling criterion (3.17); whereas in the MSFV method the formulation comes from the Galerkin framework we use to compute a

set of basis functions that are necessary to construct the projected system (4.6).

In the above process, we opt for the construction of the operator-induced interpolation matrix $\mathbf{P}$; however, it is possible to avoid its construction. As shown in Chapter 2 of the book by Efendiev and Hou ([51]), it is possible to assemble directly the matrix $\mathbf{A}^H$ of the coarse-mesh system in (4.6) through locally projected stiffness matrices, which are generated using $\mathbf{P}_k$. The former approach is preferred when the solution is needed in the coarse mesh only as it reduces the storage requirements. In Section 4.4, I show examples of an application of this type. If the fine-mesh solution is needed, then the first approach is preferred.

The accuracy of the solutions obtained with multiscale FV/FE methods depends on the choice of boundary conditions used to construct the multiscale basis functions (second step outlined before) for each coarse cell. If these boundary conditions fail to reflect the effect of the underlying media heterogeneity contained by the coarse cell on the physical responses, multiscale procedures can have large errors [51, 89].

Researchers in the field of multiscale methods for elliptic problems have noted that by choosing a set of linear boundary conditions for the construction of the multiscale basis functions, a mismatch between the exact solution and the discrete solution across the coarse-cell boundary may be created, thus yielding to inaccurate solutions. The error analyses presented in [89] and in [51] demonstrate that the source of inaccuracy in the solution comes from resonance errors; that is, errors that appear when the mesh size and the wavelength of the small-scale oscillation of the media heterogeneity are similar. A solution in such cases is to use oversampling techniques for the construction of the multiscale basis functions [51, 79, 88, 89, 101].

In the next section, we discuss the case where the choice of linear boundary conditions to construct the multiscale basis functions may yield inaccurate solutions using the MSFV method, and we develop an oversampling technique to fix this accuracy issue.

4.3   The Oversampling Method

As discussed in the previous section, the MSFV method imposes linear bound-
ary conditions to the local Maxwell's formulation (4.1)-(4.3) used to compute the
multiscale basis functions inside each coarse-mesh cell. Note that by choosing
linear boundary conditions for the multiscale basis functions, the MSFV method
assumes that the tangential components of the electric field behave linearly at
the interfaces between coarse-mesh cells. However, this assumption fails for the
cases where the media contained by the coarse cells is highly heterogeneous,
as it is well known that heterogeneous conductive media induce a non-linear and
non-smooth behavior of the electric field across media interfaces ([169]). In par-
ticular, when the heterogeneity is located close to the boundary of the coarse cell,
the non-linear behavior of the electric field significantly violates the assumption
of linear fields at the boundaries. Hence, by imposing linear boundary conditions
in such cases for the construction of the multiscale basis functions, the MSFV
method creates a mismatch between the true and the multiscale solution across
the coarse cell boundary. This mismatch yields to produce inaccurate solutions.
In this section, we propose an oversampling technique to overcome this difficulty.

Oversampling methods are used to reduce boundary effects in the construc-
tion of the multiscale basis functions per single coarse-mesh cell [51, 89]. The
main idea is to compute the multiscale basis functions using a local extended
domain, and to use only the fine-mesh information at the interior of the cell to
construct the multiscale basis functions.

We now proceed to develop our oversampling technique. To do so, we adapt
the oversampling technique originally proposed by [89] for linear elliptic problems
with strongly discontinuous coefficients and for a nodal FE discretization, to ap-
ply to the MSFV method for EM modeling with edge variables discussed in the
previous section, which uses a staggered FV discretization (i.e., the MFV method
discussed in Section 2.4).

For a given coarse cell Ω_k^H, the core idea behind our oversampling method
consists of the following two steps, which are illustrated in Figure 4.2.

First, we compute multiscale basis functions using a *local extended domain*,
denoted as $\Omega_k^{H,\text{ext}}$, which includes the coarse cell Ω_k^H and a neighborhood of fine
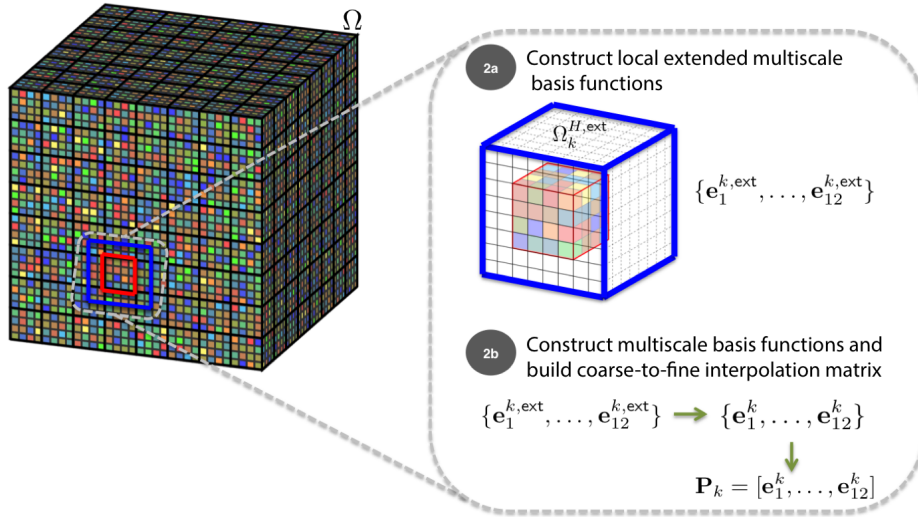
Figure 4.2: Schematic representation of the two main steps to implement the oversampling method.

cells around it. If the coarse cell Ω_k^H is at the boundary of the computational domain, then we only extend the local domain to where it is possible. To compute the multiscale basis functions in $\Omega_k^{H,\text{ext}}$, we formulate the twelve local Maxwell systems as in (4.1)-(4.3), but rather than using Ω_k^H as the local domain we use $\Omega_k^{H,\text{ext}}$, then we apply the MFV method as discussed in Section 2.4. We refer to the set of discrete solutions $\{\mathbf{e}_1^{k,\text{ext}}, \ldots, \mathbf{e}_{12}^{k,\text{ext}}\}$ as *extended multiscale basis functions* for the cell Ω_k^H.

Second, we use the set of extended multiscale basis functions obtained in the previous step to compute the actual set of multiscale basis functions $\{\mathbf{e}_1^k, \ldots, \mathbf{e}_{12}^k\}$ in Ω_k^H. Since the construction of the multiscale basis is done cell by cell, there is no guaranty that the tangential components of the multiscale basis functions are continuous at the boundary of the coarse cell Ω_k^H. In order to mitigate this issue, we impose the following *weak-continuity condition* in the construction of the

multiscale basis functions to guarantee they will be weakly continuous along each shared boundary among immediate neighboring coarse cells,

$$\mathscr{A}_{\text{edge}_m}\left(\vec{E}_l^k\right) := \frac{1}{L_{\text{edge}_m}} \int_{\text{edge}_m} \vec{E}_l^k \cdot \vec{\tau}_{\text{edge}_m}\, ds = \delta_{ml}; \;\; m,l = 1,\ldots,12, \qquad (4.8)$$

where $\vec{E}_l^k$ denotes the continuous form of the lth multiscale basis function $\mathbf{e}_l^k$, L_{edge_m} denotes the length of the mth edge of Ω_k^H, $\vec{\tau}_{\text{edge}_m}$ denotes the unit tangent vector to the mth edge of Ω_k^H, and δ_{ml} is the Kronecker delta. That is, we take a 'normalized average' of the multiscale basis functions at the boundary of the coarse cell. This condition is equivalent to the definition of edge degrees of freedom of a staggered cell in the context of Nédélec finite elements [130, 131]. Note the difference with the continuity condition (4.4) imposed in the construction of the multiscale functions of the MSFV method without oversampling. Integrating numerically the continuity condition (4.8), we can express it as

$$\hat{\mathscr{A}}_{\text{edge}_m}\left(\mathbf{e}_l^k\right) \approx \mathbf{v}_{\text{edge}_m}^\top \mathbf{e}_l^k = \delta_{ml}; \;\; m,l = 1,\ldots,12, \qquad (4.9)$$

where $\mathbf{v}_{\text{edge}_m}$ is the vector that computes the normalized line integral along the mth edge of Ω_k^H.

Using (4.9) and following the main lines given in the oversampling technique proposed by [89], we continue the development of our oversampling technique by showing how to compute $\{\mathbf{e}_1^k,\ldots,\mathbf{e}_{12}^k\}$ from $\{\mathbf{e}_1^{k,\text{ext}},\ldots,\mathbf{e}_{12}^{k,\text{ext}}\}$ in detail.

We begin by expressing the jth multiscale basis function, $\mathbf{e}_j^k$, as a linear combination of the set of extended basis functions as follows

$$\mathbf{e}_j^k = \sum_{l=1}^{12} c_{l,j}\, \mathbf{e}_l^{k,\text{ext}} = [\mathbf{e}_1^{k,\text{ext}},\ldots,\mathbf{e}_{12}^{k,\text{ext}}]\,\mathbf{c}_j; \quad j = 1,\ldots,12, \qquad (4.10)$$

where $\mathbf{c}_j = [c_{1,j},\ldots,c_{12,j}]^\top$ are coefficients to be determined. Now, to determine uniquely such coefficients, we apply condition (4.9) to (4.10), which results in the

following system of equations

$$
\begin{bmatrix}
\hat{\mathscr{A}}_{\text{edge}_1}(\mathbf{e}_1^{k,\text{ext}}) & \cdots & \hat{\mathscr{A}}_{\text{edge}_1}(\mathbf{e}_{12}^{k,\text{ext}}) \\
\hat{\mathscr{A}}_{\text{edge}_2}(\mathbf{e}_1^{k,\text{ext}}) & \cdots & \hat{\mathscr{A}}_{\text{edge}_2}(\mathbf{e}_{12}^{k,\text{ext}}) \\
\vdots & \ddots & \vdots \\
\hat{\mathscr{A}}_{\text{edge}_{12}}(\mathbf{e}_1^{k,\text{ext}}) & \cdots & \hat{\mathscr{A}}_{\text{edge}_{12}}(\mathbf{e}_{12}^{k,\text{ext}})
\end{bmatrix}
\begin{bmatrix}
c_{1,1} & \cdots & c_{1,12} \\
c_{2,1} & \cdots & c_{2,12} \\
\vdots & \ddots & \vdots \\
c_{12,1} & \cdots & c_{12,12}
\end{bmatrix}
= \mathbf{I}_{12\times12},
$$

(4.11)

where $\mathbf{I}_{12\times12}$ denotes the 12×12 identity matrix. Combining equations (4.9), (4.10) and (4.11), we obtain the expression for the desired coefficients, that is

$$
\mathbf{C} =
\begin{bmatrix}
\mathbf{v}_{\text{edge}_1}^{\top}\mathbf{e}_1^{k,\text{ext}} & \cdots & \mathbf{v}_{\text{edge}_1}^{\top}\mathbf{e}_{12}^{k,\text{ext}} \\
\mathbf{v}_{\text{edge}_2}^{\top}\mathbf{e}_1^{k,\text{ext}} & \cdots & \mathbf{v}_{\text{edge}_2}^{\top}\mathbf{e}_{12}^{k,\text{ext}} \\
\vdots & \ddots & \vdots \\
\mathbf{v}_{\text{edge}_{12}}^{\top}\mathbf{e}_1^{k,\text{ext}} & \cdots & \mathbf{v}_{\text{edge}_{12}}^{\top}\mathbf{e}_{12}^{k,\text{ext}}
\end{bmatrix}^{-1}.
$$

(4.12)

Now, $\mathbf{C}$ is invertible because its columns are linearly independent. To see this, we consider the matrix (4.12) before it is inverted. To show that the columns of this matrix form a linearly independent set, we need to show that for any linear combination of such vectors:

$$
\alpha_1
\begin{bmatrix}
\mathbf{v}_{\text{edge}_1}^{\top}\mathbf{e}_1^{k,\text{ext}} \\
\mathbf{v}_{\text{edge}_2}^{\top}\mathbf{e}_1^{k,\text{ext}} \\
\vdots \\
\mathbf{v}_{\text{edge}_{12}}^{\top}\mathbf{e}_1^{k,\text{ext}}
\end{bmatrix}
+ \cdots + \alpha_{12}
\begin{bmatrix}
\mathbf{v}_{\text{edge}_1}^{\top}\mathbf{e}_{12}^{k,\text{ext}} \\
\mathbf{v}_{\text{edge}_2}^{\top}\mathbf{e}_{12}^{k,\text{ext}} \\
\vdots \\
\mathbf{v}_{\text{edge}_{12}}^{\top}\mathbf{e}_{12}^{k,\text{ext}}
\end{bmatrix}
=
\begin{bmatrix}
0 \\
0 \\
\vdots \\
0
\end{bmatrix}
$$

(4.13)

the scalars $\alpha_1,\ldots,\alpha_{12}$ are zero. As described before (4.9), $\mathbf{v}_{\text{edge}_m}^{\top}$; $m=1,\ldots,12$ denotes the vector that computes the normalized line integral along the mth edge of the coarse cell Ω_k^H. Now, we can write expression (4.13) as

$$
\alpha_1
\begin{bmatrix}
\mathbf{v}_{\text{edge}_1}^{\top} \\
\mathbf{v}_{\text{edge}_2}^{\top} \\
\vdots \\
\mathbf{v}_{\text{edge}_{12}}^{\top}
\end{bmatrix}
\mathbf{e}_1^{k,\text{ext}}
+ \cdots + \alpha_{12}
\begin{bmatrix}
\mathbf{v}_{\text{edge}_1}^{\top} \\
\mathbf{v}_{\text{edge}_2}^{\top} \\
\vdots \\
\mathbf{v}_{\text{edge}_{12}}^{\top}
\end{bmatrix}
\mathbf{e}_{12}^{k,\text{ext}}
=
\begin{bmatrix}
\mathbf{v}_{\text{edge}_1}^{\top} \\
\mathbf{v}_{\text{edge}_2}^{\top} \\
\vdots \\
\mathbf{v}_{\text{edge}_{12}}^{\top}
\end{bmatrix}
\sum_{l=1}^{12} \alpha_l \mathbf{e}_l^{k,\text{ext}} = \vec{0}.
$$

(4.14)

Since $\{\mathbf{e}_l^{k,\text{ext}}\}_{l=1}^{12}$ form a basis, then $\alpha_l = 0$, $\forall l = 1, \ldots, 12$.

After we construct the multiscale basis functions $\{\mathbf{e}_1^k, \ldots, \mathbf{e}_{12}^k\}$ using our over-sampling technique, we continue to follow the procedure for the MSFV method (Figure 4.1) to compute the solution. That is, this set of twelve multiscale basis functions enable the use of the local interpolation matrix $\mathbf{P}_k$, given by (4.5), within the assembly of the global coarse-to-fine interpolation matrix $\mathbf{P}$. The interpolation matrix $\mathbf{P}$ is then used within a Galerkin formulation to obtain the coarse-mesh system (4.6), which we ultimately solve.

4.4   Numerical Results in 3D

In this section, we demonstrate the accuracy and computational performance of our multiscale finite volume method with oversampling (MSFV+O) by simulating EM responses for two 3D synthetic electrical conductivity models: one with a mineral deposit in a geologically-rich medium and one with a random isotropic heterogeneous medium. As analytical solutions are not available for these two examples, the results of these simulations are compared to the simulation results from the fine-mesh reference models, respectively. Since we need to use a fine mesh to compute the multiscale basis functions numerically, it makes sense to compare our MSFV+O method with a traditional FV method at the fine mesh. This example also demonstrates the power of combining adaptive mesh refinement techniques with a multiscale approach to produce faster and accurate simulations.

4.4.1   Simulations for the Synthetic Lalor Model

For the first example, we use the synthetic Lalor electrical conductivity model introduced in Section 3.5.2, which is based on the inversion results of field measurements over the Canadian Lalor mine obtained by [177].

As discussed in Section 3.5.2, the Lalor model, shown in Figure 4.3, has an area with non-flat topography and extends from 0 to 6.5 km along the x, y and z directions, respectively. The model comprises air and the subsurface that is composed of 35 geologic units. The unit with the largest conductivity value represents the mineral deposit, which is composed of three bodies. We assume a conductivity of 10^{-8} S/m in the air. The subsurface conductivity values range
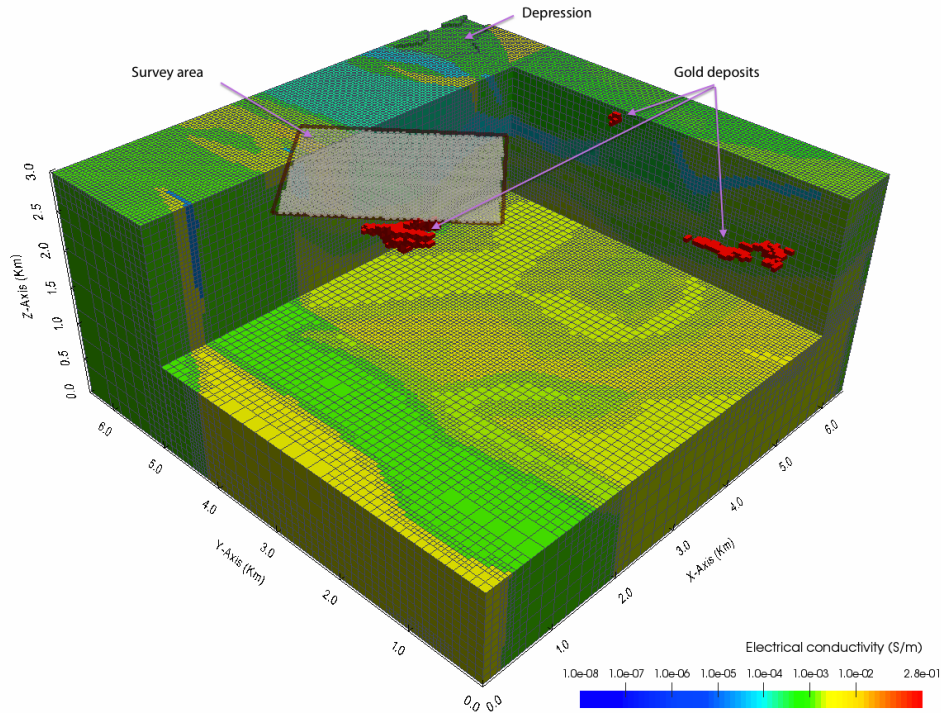
Figure 4.3: Subsurface part of the synthetic electrical conductivity Lalor model and large-loop EM survey setup. The model is discretized on a fine OcTree mesh with 546,295 cells. The conductivity varies over five orders of magnitude throughout the whole model.

from 1.96×10^{-5} to 0.28 S/m. The magnetic permeability takes its free space value (i.e., $\mu = 4\pi \times 10^{-7}$ Vs/Am).

We consider a large-loop EM survey for this example, where we use a rectangular transmitter loop with dimensions 2 km × 3 km, operating at the frequencies of 1, 10, 20, 40, 100, 200 and 400 Hz. The transmitter is placed on the earth's surface and it is centered above the largest body of the mineral deposit, as shown in Figure 4.3. Inside the loop, we place a uniform grid of receivers that measure the three components of the magnetic flux ($\vec{B} = [B^x, B^y, B^z]^\top$). The receivers are separated by 50 m along the x and y directions, respectively.

Our aim is to estimate the *secondary magnetic flux induced by the mineral deposit* in the survey area. For this purpose, we simulate two sets of the magnetic

flux data for each frequency. The first data set considers the conductivity model including all geologic units, and the second data set excludes the mineral deposit from the original conductivity model. Each of these two data sets consists of the measurements of $\vec{B}$ taken at the receiver locations. The secondary magnetic flux induced by the mineral deposit at the survey area, denoted as $\Delta\vec{B}_{\text{deposit}}$, is then computed by subtracting the two data sets. The estimation of $\Delta\vec{B}_{\text{deposit}}$ requires carrying out two forward model simulations per frequency.

To compute a reference solution, we discretize the conductivity model using the MFV method as discussed in [72, 86] at the same fine OcTree mesh described in Section 3.5.2, which is shown in Figure 4.3. The fine mesh has 546,295 cells. Considering the averaged background conductivity value (4.5×10^{-3} S/m), the skin depths for the frequencies of 1, 10, 20, 40, 100, 200 and 400 Hz are roughly 7,498, 2,371, 1,677, 1,186, 750, 530 and 375 m, respectively. Thus, using cells sizes of $(50 \text{ m})^3$ within the survey area continues to be sufficient to capture the behavior of the EM fields in this setup. Using the MFV method on the fine OcTree mesh yields systems with roughly 1.5 millions edge DOF which we solve using the parallel sparse direct solver MUMPS [3]. The average computation time per single simulation is roughly 721 s on a two hexa-core Intel Xeon X5660 CPUs at 2.8 Hz with 64 GB shared RAM using the parallel computing toolbox of MATLAB ([162]). Figure 4.4 shows the Euclidean norm of the total, real and imaginary parts of $\Delta\vec{B}_{\text{deposit}}$ for each frequency considered. The real and imaginary parts of the results obtained for the z-component of $\Delta\vec{B}_{\text{deposit}}$, denoted as $\Delta B^z_{\text{deposit}}$, at 100 Hz are shown in Figure 4.6(a) and Figure 4.7(a), respectively.

In order to use the MSFV+O method introduced in Section 4.3, we need to choose a suitable coarse mesh to discretize the conductivity model and the size of the local extended domain to compute its corresponding projection matrix.

As a coarse mesh, we consider the same coarse OcTree mesh nested in the fine OcTree mesh previously described in Section 3.5.2, which is shown in Figure 4.5. The coarse OcTree mesh is designed to maintain the fine-mesh resolution of $(50 \text{ m})^3$ inside the survey area, whereas the rest of the domain is filled with gradually increasing coarser cells. In total, this coarse mesh has 60,656 cells. To analyze the performance of our MSFV+O method for coarse OcTree meshes, we do not refine the mesh outside the survey area where a large conductivity contrast
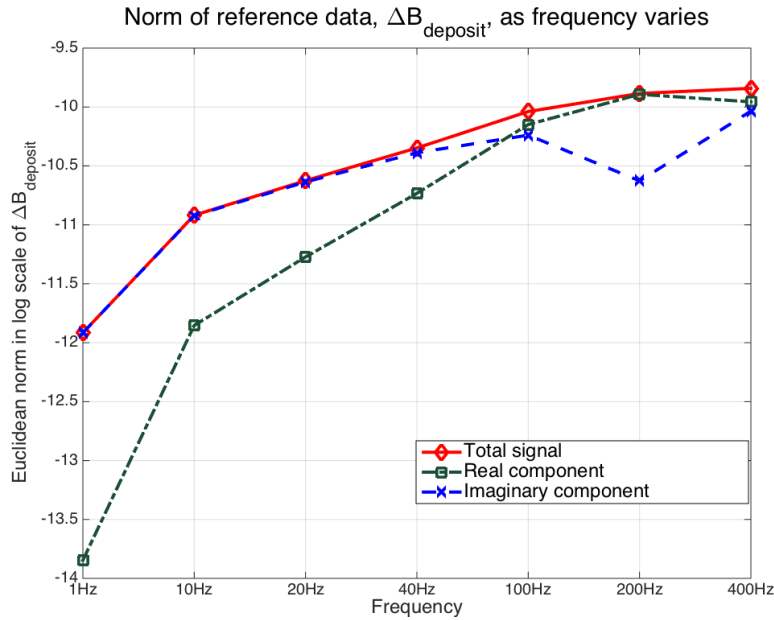
Figure 4.4: Euclidean norm of total, real and imaginary parts of the reference (fine-mesh) solution for the Lalor conductivity model per frequency.

is present in the model. For example, this mesh discretizes the mineral deposit with cells of size $(200 \text{ m})^3$ and $(400 \text{ m})^3$, and the non-flat topography with cells of size $(400 \text{ m})^3$ and $(800 \text{ m})^3$. We expect the simulations for the frequencies of 200 and 400 Hz to be particularly challenging for our MSFV+O method as the coarsening in those areas can be considered extreme due to the cell size is in the order of the skin depth.

Next, to investigate the effect of the size of the local extended domain, i.e., the number of fine-mesh padding cells by which we extend every coarse cell, on the resulting magnetic flux data, we pad the coarse cell using 2, 4 and 8 fine cells. Each fine padding cell is of size $(50 \text{ m})^3$. The chosen local extended domain sizes correspond to extending each $(200 \text{ m})^3$-coarse cell by half, one and two coarse cells, respectively. The $(200 \text{ m})^3$-coarse cells are the majority of the coarse cells where the largest conductivity contrast happen in this setting (Figure 4.5).

Applying MSFV and MSFV+O on the coarse mesh shown in Figure 4.5, we
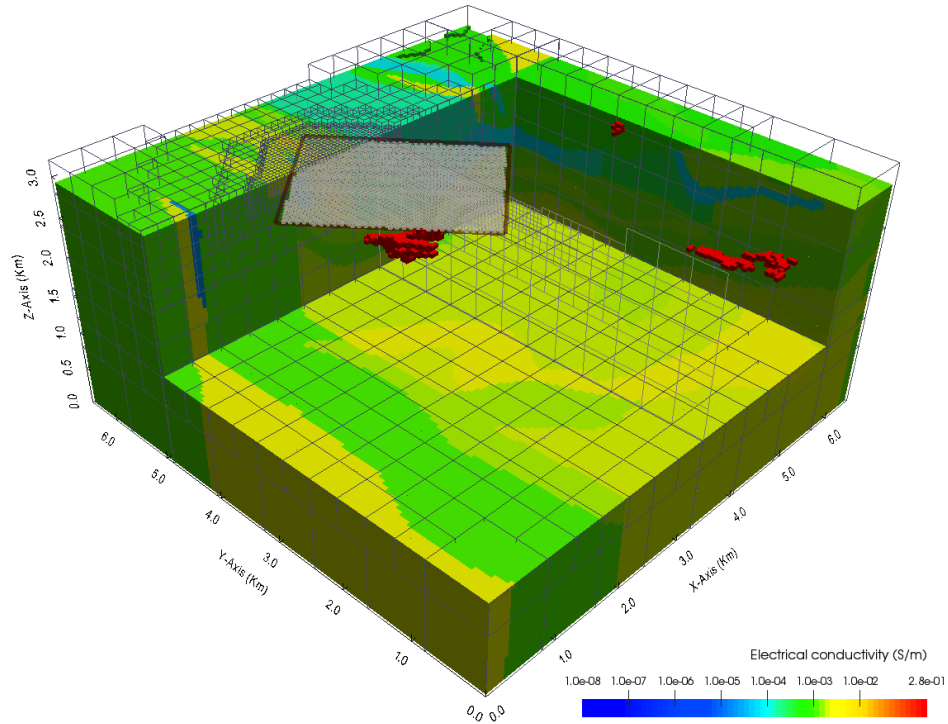
Figure 4.5: Subsurface part of the synthetic electrical conductivity Lalor model and large-loop EM survey setup. The model is discretized on a coarse OcTree mesh with 60,656 cells. The conductivity varies over eight orders of magnitude throughout the whole model.

obtain reduced linear systems with 169,892 DOF, which are also solved using MUMPS. When using MSFV+O the total average run times per single simulation for extended domain sizes of 2, 4 and 8 padding cells are roughly 185 s, 442 s and 1 h, respectively, on the same machine. The real and imaginary parts of $\Delta B^z_{\text{deposit}}$ at 100 Hz for extended domain sizes of 2, 4 and 8 padding cells are shown in Figures 4.6(b), 4.6(c) and 4.6(d), respectively; and Figures 4.7(b), 4.7(c) and 4.7(d), respectively. In order to use MSFV (without oversampling), we first adapt this method for OcTree meshes, as the original version is derived for tensor meshes only (cf. [73]). In this case, the total average run time per single simulation is roughly 73 s on the same machine. The real and imaginary parts of $\Delta B^z_{\text{deposit}}$ at 100 Hz are shown in Figure 4.6(e) and Figure 4.7(e), respectively.

96

We also carry out MFV simulations using homogenized electrical conductivity models that we construct using volume-arithmetic, -geometric and -harmonic averaging of the fine-mesh conductivity inside each coarse cell of the OcTree mesh shown in Figure 4.5. Doing so allows us to compare the accuracy that MFV solutions achieve on the coarse mesh with the one achieved by MSFV with and without oversampling. The total average run time per single simulation is roughly 128 s on the same machine. The real and imaginary parts of $\Delta B^z_{\mathrm{deposit}}$ at 100 Hz for each of the three homogenized solutions are shown in Figures 4.6(f), 4.6(g) and 4.6(h), respectively; and Figures 4.7(f), 4.7(g) and 4.7(h), respectively.

Figures 4.6 and 4.7 show the results obtained for the real and imaginary parts of $\Delta B^z_{\mathrm{deposit}}$ with MFV on the fine-mesh, MSFV, MSFV+O with three different oversampling sizes, and MFV with three different homogenized conductivity models for the frequency of 100 Hz, respectively. All results are plotted using the same color scale and range. From these figures we see that our oversampling technique produces the most accurate results in comparison with the rest of the methods used. Observe that using only an oversampling size of 2 padding cells significantly improves the quality of the approximations, whereas MSFV tends to overestimate the approximation for both real and imaginary parts of $\Delta B^z_{\mathrm{deposit}}$.

97
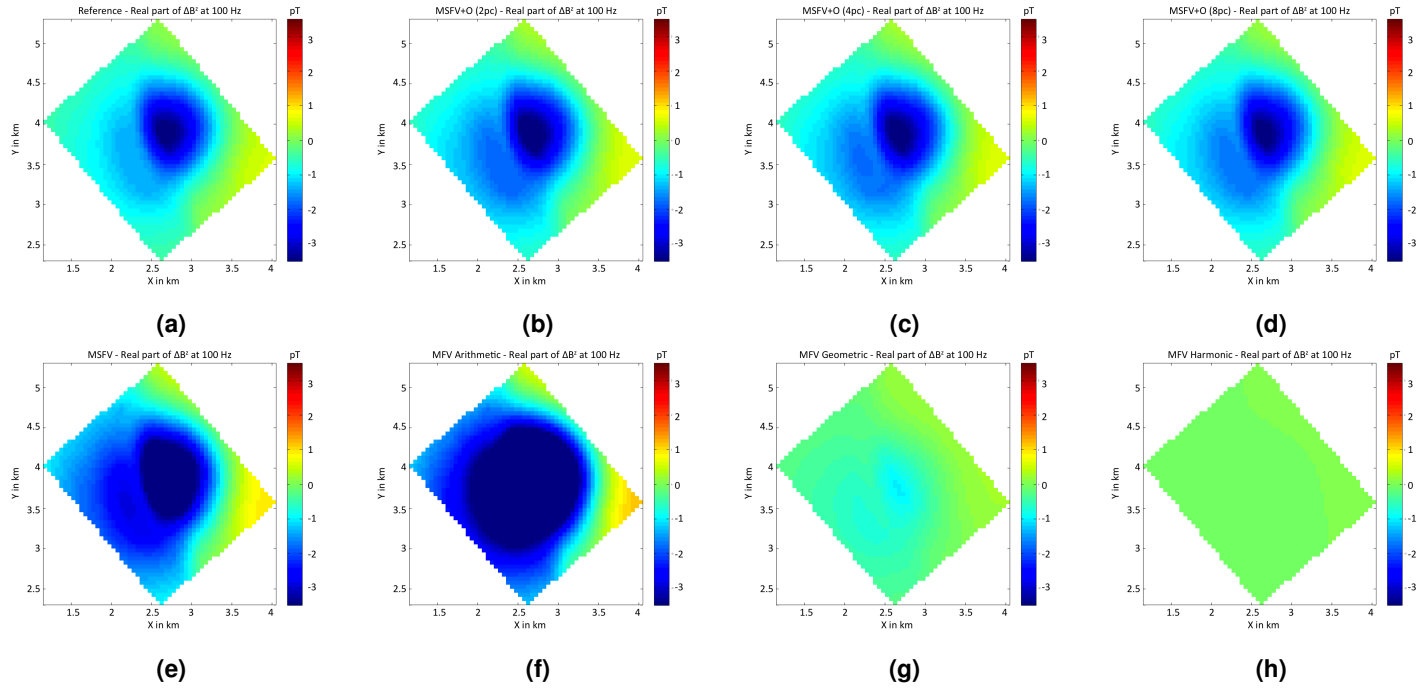
Figure 4.6: Real part of the z component of the secondary magnetic flux induced by the mineral deposit in the survey area, $\Delta B^z_{\text{deposit}}$, for our large-loop EM survey at 100 Hz. (a) reference solution computed using the MFV method on the fine OcTree mesh with 546,295 cells. (b), (c) and (d): results using the MSFV+O method with 2, 4 and 8 padding cells on the coarse OcTree mesh, respectively. (e): results using the MSFV (without oversampling) method on the coarse OcTree mesh with 60,656 cells. (f), (g) and (h): results using MFV with the conductivity model homogenized using arithmetic, geometric and harmonic averaging on the coarse OcTree mesh, respectively. All results are shown in picoteslas (pT) and plotted using the same color scale.

Figure 4.7: Imaginary part of the z component of the secondary magnetic flux induced by the mineral deposit in the survey area, $\Delta B^z_{\text{deposit}}$, for our large-loop EM survey at 100 Hz. (a) reference solution computed using the MFV method on the fine OcTree mesh with 546,295 cells. (b), (c) and (d): results using the MSFV+O method with 2, 4 and 8 padding cells on the coarse OcTree mesh, respectively. (e): results using the MSFV (without oversampling) method on the coarse OcTree mesh with 60,656 cells. (f), (g) and (h): results using MFV with the conductivity model homogenized using arithmetic, geometric and harmonic averaging on the coarse OcTree mesh, respectively. All results are shown in picoteslas (pT) and plotted using the same color scale.

Table 4.1 shows the relative errors in Euclidean norm for the total, real and imaginary parts of $\Delta\vec{B}_{\text{deposit}}$ obtained from comparing the reference (fine-mesh) solution with the MSFV, MSFV+O and MFV with three different homogenized solutions for each frequency and local extended domain size. Table 4.2 shows the relative errors in Euclidean norm for the magnitude of the three components of $\Delta\vec{B}_{\text{deposit}}$ ($\Delta\vec{B}_{\text{deposit}} = [\Delta B^x_{\text{deposit}}, \Delta B^y_{\text{deposit}}, \Delta B^z_{\text{deposit}}]^\top$) obtained from comparing the reference (fine-mesh) solution with the MSFV, MSFV+O and MFV with three different homogenized solutions for each frequency and local extended domain size. The relative error is computed as the ratio of the Euclidean norm of the difference of the fine and coarse-mesh data to the Euclidean norm of the fine-mesh data. The coarse-mesh solutions are not interpolated to the fine mesh to compute the error. Table 4.3 summarizes the average run time per single simulation required to compute $\Delta\vec{B}_{\text{deposit}}$ for each of the methods discussed. From these tables we observe the following:

First, we see that our oversampling technique significantly improves the accuracy for the total, real and imaginary response as well as for each of the three components of the solution in comparison to the MSFV and MFV with three different homogenized conductivity models as the errors decrease with oversampling. In particular, it is surprising to see how well MFV with simple geometric averaging did when compared with MSFV.

Second, as the size of the local extended domain increases the error decreases at the expense of more computational run time, which, however, is still considerably lower compared to the time of the reference solution for the cases of 2 and 4 padding cells (see Table 4.3). These results suggest that by using a local extended domain size of at least a half the number of fine cells contained in the coarse cell(s) where the major contrast of conductivity happens, we may increase significantly the accuracy obtained with MSFV+O.

Third, the magnitude of the errors come from comparing secondary magnetic field data obtained on the fine and coarse mesh, respectively. The data is the response of the deep and buried conductive mineral deposit, which constitutes a rather weak secondary field compared to the primary field induced by the air and background conductivity. The level of accuracy of this simulation is relative to the total signal, which values are quite small (see Figure 4.4). We can improve the

100

accuracy of MSFV and MSFV+O by refining the coarse mesh and interpolating the coarse-mesh solution to the fine mesh as shown in [73]. Yet, MSFV+O provides a reasonable approximation to the fine-mesh solution using a coarse mesh that is only 10% the size of the fine mesh.

Fourth, the errors for the imaginary part of $\Delta\vec{B}_{\mathrm{deposit}}$ for the frequencies of 1, 10, 20 and 40 Hz resemble the errors for total $\Delta\vec{B}_{\mathrm{deposit}}$ due to the real part of $\Delta\vec{B}_{\mathrm{deposit}}$ is up to two orders of magnitude smaller than their corresponding imaginary parts (Figure 4.4). For the frequencies of 100 and 400 Hz, where the real and imaginary parts of $\Delta\vec{B}_{\mathrm{deposit}}$ are roughly in the same order of magnitude, we see the relative error for total $\Delta\vec{B}_{\mathrm{deposit}}$ represents the error contributions of these two components of the data.

Fifth, for the simulation at 200 Hz the errors for the real part of $\Delta\vec{B}_{\mathrm{deposit}}$ resemble the errors for total $\Delta\vec{B}_{\mathrm{deposit}}$ due to the imaginary part of $\Delta\vec{B}_{\mathrm{deposit}}$ is one order of magnitude smaller (Figure 4.4). The large errors in the imaginary part of the data as well as the increase and decrease in the error going from padding cell 2 to 4 and 4 to 8, respectively, can be attributed to the combined discretization error in simulating secondary field data and the extreme coarsening in the mesh shown in Figure 4.5. For this frequency, the cell sizes used to discretize the mineral deposit are in the order of the skin depth.

Sixth, for a simulation at 400 Hz with an extended domain size of 8 padding cells the slight increment in the error of the real part may be attributed to the excessive coarsening in the mesh for such high frequency. In this case, the coarse cells used to discretize the mineral deposit are larger than the skin depth. Despite the excessive coarsening, our oversampled approximation yields comparable results to the reference (fine-mesh) solution for the largest two frequencies.

Seventh, the increment of the MSFV+O setup time as the size of the local extended domain increases (Table 4.3) comes from constructing the local interpolation matrices. Since the computation of these matrices is done locally inside each coarse cell independently of each other, this process can be done in parallel (see discussion in Section 4.2). A robust implementation using a parallel communication protocol (e.g. Message Passage Interface (MPI)) for programming parallel computers should greatly reduce the overhead time in constructing these interpolation matrices. The research work in [46], which focuses in prob-

lems in porous media, shows progress along this lines. However, we note that using oversampling with 2 padding cells is already increasing the accuracy of the solution and the computational time is significantly lower that that of computing the reference solution.

Table 4.1: Relative errors in Euclidean norm for the total, real and imaginary parts of the secondary magnetic fluxes induced by the mineral deposit in the survey area, $\Delta \vec{B}_{\mathrm{deposit}}$. Note that pc stands for padding cells.

Table of relative errors in Euclidean norm for $\Delta \vec{B}_{\mathrm{deposit}}$							
	Frequency						
Method	1Hz	10Hz	20Hz	40Hz	100Hz	200Hz	400Hz
Relative errors for total $\Delta \vec{B}_{\mathrm{deposit}}$ (per cent)							
MFV+Arithmetic	192.05	191.60	190.43	187.70	183.25	171.94	149.34
MFV+Geometric	68.57	68.51	68.34	67.72	64.96	60.61	55.62
MFV+Harmonic	97.20	97.20	97.18	97.11	96.81	96.30	95.57
MSFV	69.70	69.72	69.79	70.32	73.09	72.65	63.93
MSFV+O (2 pc)	15.84	15.83	15.79	15.75	16.17	15.98	13.46
MSFV+O (4 pc)	13.31	13.33	13.38	13.60	14.48	14.63	11.36
MSFV+O (8 pc)	10.63	10.65	10.72	10.98	12.20	12.67	10.08
Relative errors for real part of $\Delta \vec{B}_{\mathrm{deposit}}$ (per cent)							
MFV+Arithmetic	216.47	214.97	211.12	202.06	188.63	170.99	159.57
MFV+Geometric	81.01	80.95	80.75	79.72	73.05	60.33	34.18
MFV+Harmonic	98.46	98.45	98.43	98.33	97.74	96.52	93.45
MSFV	73.09	72.92	72.56	72.29	74.22	70.82	59.47
MSFV+O (2 pc)	21.41	21.34	21.16	20.57	18.11	14.21	8.25
MSFV+O (4 pc)	18.36	18.38	18.39	18.19	15.92	12.49	8.14
MSFV+O (8 pc)	16.12	16.10	16.02	15.49	12.74	10.40	8.51
Relative errors for imaginary part of $\Delta \vec{B}_{\mathrm{deposit}}$ (per cent)							
MFV+Arithmetic	192.05	191.26	189.26	184.63	174.80	197.75	133.27
MFV+Geometric	68.57	68.32	67.61	64.99	50.30	68.40	76.55
MFV+Harmonic	97.20	97.18	97.11	96.86	95.38	89.47	98.52
MSFV	69.70	69.67	69.64	69.91	71.34	114.01	69.83
MSFV+O (2 pc)	15.84	15.74	15.45	14.57	12.68	42.77	18.53
MSFV+O (4 pc)	13.31	13.24	13.06	12.46	11.99	43.84	14.81
MSFV+O (8 pc)	10.63	10.55	10.36	9.81	11.35	41.16	11.98

Table 4.2: Relative errors (per cent) in Euclidean norm for the magnitude of the x, y and z components of the secondary magnetic fluxes induced by the mineral deposit in the survey area, $\Delta \vec{B}_{\text{deposit}}$. Note that pc stands for padding cells.

Method	$\Delta B^x_{\text{deposit}}$	$\Delta B^y_{\text{deposit}}$	$\Delta B^z_{\text{deposit}}$	$\Delta B^x_{\text{deposit}}$	$\Delta B^y_{\text{deposit}}$	$\Delta B^z_{\text{deposit}}$
		Frequency of 1 Hz				
MFV+Arithmetic	176.44	202.20	195.12			
MFV+Geometric	66.26	71.52	68.65			
MFV+Harmonic	97.03	97.38	97.22			
MSFV	65.91	70.44	70.95			
MSFV+O (2 pc)	13.37	19.83	15.53			
MSFV+O (4 pc)	12.04	16.24	12.90			
MSFV+O (8 pc)	10.45	12.13	10.25			
		Frequency of 10 Hz			Frequency of 100 Hz	
MFV+Arithmetic	176.20	201.86	194.59	170.48	198.30	184.62
MFV+Geometric	66.17	71.50	68.60	62.34	68.63	65.11
MFV+Harmonic	97.03	97.37	97.21	96.63	97.05	96.82
MSFV	66.06	70.39	70.94	70.39	73.56	74.16
MSFV+O (2 pc)	13.39	19.78	15.51	14.00	19.41	16.13
MSFV+O (4 pc)	12.05	16.25	12.93	12.56	17.12	14.52
MSFV+O (8 pc)	10.45	12.14	10.29	11.26	13.31	12.30
		Frequency of 20 Hz			Frequency of 200 Hz	
MFV+Arithmetic	175.59	201.03	193.21	159.79	189.57	172.55
MFV+Geometric	65.91	71.44	68.44	58.65	63.69	60.68
MFV+Harmonic	97.00	97.37	97.20	96.20	96.47	96.30
MSFV	66.48	70.30	70.95	68.82	75.18	73.73
MSFV+O (2 pc)	13.45	19.65	15.48	13.41	19.21	16.15
MSFV+O (4 pc)	12.07	16.28	13.01	12.76	16.76	14.85
MSFV+O (8 pc)	10.47	12.18	10.39	10.48	15.03	12.92
		Frequency of 40 Hz			Frequency of 400 Hz	
MFV+Arithmetic	174.12	199.32	189.94	141.64	163.62	148.96
MFV+Geometric	65.09	71.10	67.86	54.59	57.49	55.60
MFV+Harmonic	96.92	97.33	97.13	95.57	95.60	95.55
MSFV	67.73	70.43	71.36	60.31	67.47	64.68
MSFV+O (2 pc)	13.63	19.38	15.48	11.04	16.43	13.64
MSFV+O (4 pc)	12.15	16.42	13.33	9.52	13.52	11.56
MSFV+O (8 pc)	10.56	12.36	10.76	7.83	12.82	10.23

Table 4.3: Average run time in seconds per simulation required to compute $\Delta \vec{B}_{\text{deposit}}$ on a two hexa-core Intel Xeon X5660 CPUs at 2.8 Hz with 64 GB shared RAM using MATLAB. *Setup time*: time required to compute the local interpolation matrices and to assemble the reduced system of equations to be solved. *Solve time*: time to solve the reduced system of equations. *Total time*: the sum of the setup and solve times.

Method	Setup time (s)	Solve time (s)	Total time (s)
MFV on fine OcTree mesh	-	721 s	721 s
MFV + Arithmetic	-	127 s	127 s
MFV + Geometric	-	128 s	128 s
MFV + Harmonic	-	128 s	128 s
MSFV	42 s	31 s	73 s
MSFV+O (2 padding cells)	147 s	38 s	185 s
MSFV+O (4 padding cells)	410 s	32 s	442 s
MSFV+O (8 padding cells)	3,566 s	32 s	3,598 s

The next example demonstrates the effect of considering a different heterogeneous conductivity model for the same survey and meshes setup on the results produced by our proposed MSFV+O method.

4.4.2   Simulations for Random Heterogeneous Isotropic Media

In this section, we construct an electrical conductivity model of a random isotropic heterogeneous medium to provide a second magnetic flux data set to validate the proposed oversampling technique. For this example, we use the same large-loop EM survey configuration, computational domain and fine and coarse-mesh setup as described in Section 4.4.1.

The new synthetic conductivity model, shown in Figure 4.8, also comprises air and the subsurface that is composed of random heterogeneous isotropic media. We assume that the subsurface conductivity is log(10)-normally distributed with mean of 2.5×10^{-3} and standard variation of 0.4. To reuse the fine-mesh setup described in Section 4.4.1, we mapped the values of the subsurface conductivity to the interval $[10^{-5}, 10^{-1}]$ S/m. Considering the averaged background conductivity value (1.6×10^{-3} S/m), the skin depths for the frequencies of 1, 10, 20, 40, 100, 200 and 400 Hz are roughly 12,575, 3,977, 2,812, 1,988, 1,258, 889 and

629 m, respectively. Thus, using cells sizes of $(50 \text{ m})^3$ within the survey area continues to be sufficient to capture the behavior of the EM fields in this setup. As in the previous example, we assume that the conductivity of the air is of 10^{-8} S/m and that the magnetic permeability takes its free space value. Note that this conductivity model does not contain clearly defined conductive features (as in the Lalor example); instead the contrast of conductivity is distributed throughout the entire subsurface part of the model. This allows us to challenge the oversampling technique with large conductivity contrast across the material interfaces.

The goal of the simulation in this case is to compute the *secondary magnetic flux induced by the random heterogeneous conductive medium* in the survey area. To do so, we simulate two sets of the magnetic flux data for each frequency. The first data set considers the conductivity model including air and the subsurface; the second data set considers a conductivity model where the subsurface is replaced by air. Each of these two data sets consists of the measurements of the three components of $\vec{B}$ taken at the receiver locations ($[\vec{B} = B^x, B^y, B^z]^\top$). The secondary magnetic flux induced by the random conductive medium at the survey area, denoted as $\Delta \vec{B}_{\text{random}}$, is then computed by subtracting the two data sets. The estimation of $\Delta \vec{B}_{\text{random}}$ requires two forward model simulations per frequency.

Now, to complete the validation for our oversampling technique we need to compute a reference solution, a multiscaled solution with and without oversampling and averaged-based homogenized solutions. We use the same machine described in Section 4.4.1, MUMPS and MATLAB to run all the simulations presented in this section.

To compute a reference solution, we apply the MFV method on the staggered fine OcTree mesh shown in Figure 4.8 (see [72, 86] for details). The average computation time per single simulation is roughly 712 s. Figure 4.9 shows the Euclidean norm of the total, real and imaginary parts of $\Delta \vec{B}_{\text{random}}$ for each frequency considered. The real and imaginary parts of the results obtained for the z-component of $\Delta \vec{B}_{\text{random}}$, denoted as $\Delta B^z_{\text{random}}$, at 100 Hz are shown in Figures 4.11(a) and 4.12(a), respectively.

Next, we apply the MSFV method with and without oversampling on the coarse OcTree mesh shown in Figure 4.10 to simulate $\Delta \vec{B}_{\text{random}}$. For this example, we use extended domain sizes of 1, 2 and 4 fine-mesh padding cells. Each fine padding
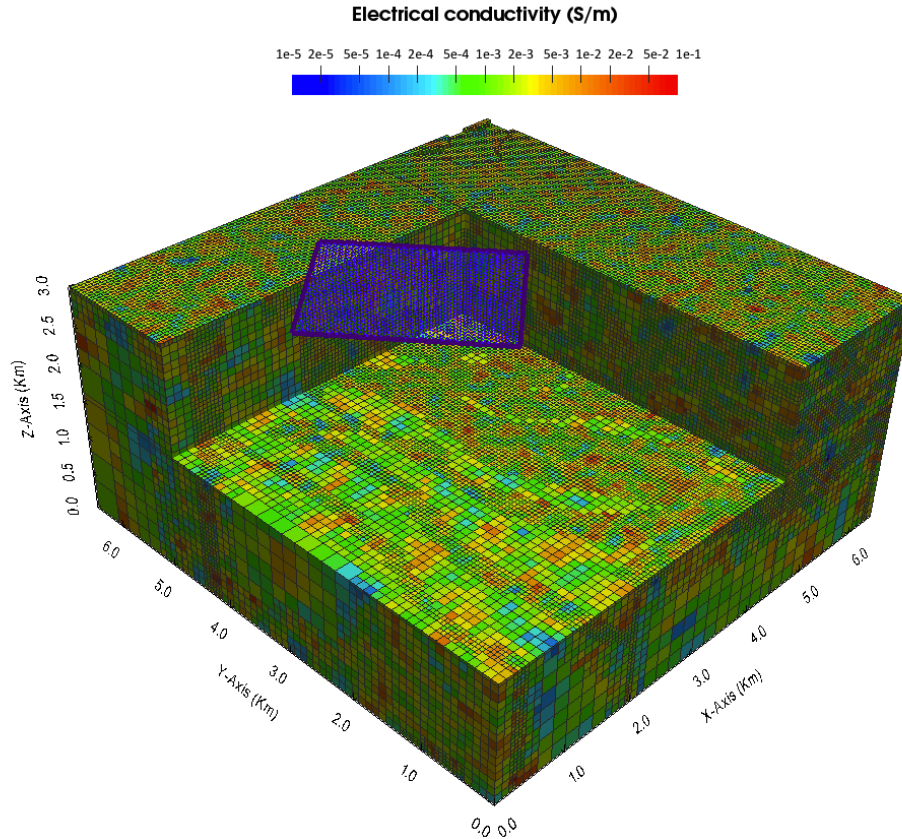
Figure 4.8: Subsurface part of the random heterogeneous isotropic electrical conductivity model and large-loop EM survey setup. The model is discretized on a fine OcTree mesh with 546,295 cells. The conductivity varies over eight orders of magnitude throughout the whole model.

cell is of size $(50\,\text{m})^3$. When using MSFV+O the total average run times per single simulation for extended domain sizes of 1, 2 and 4 padding cells are roughly 106, 156 and 439 s, respectively. The real and imaginary parts of ΔB^z_random at 100 Hz for extended domain sizes of 1, 2 and 4 padding cells are shown in Figures 4.11(b), 4.11(c) and 4.11(d), respectively; and Figures 4.12(b), 4.12(c) and 4.12(d), respectively. On the other hand, when using MSFV (without oversampling), the total average run time per single simulation is roughly 74 s. The real and imaginary
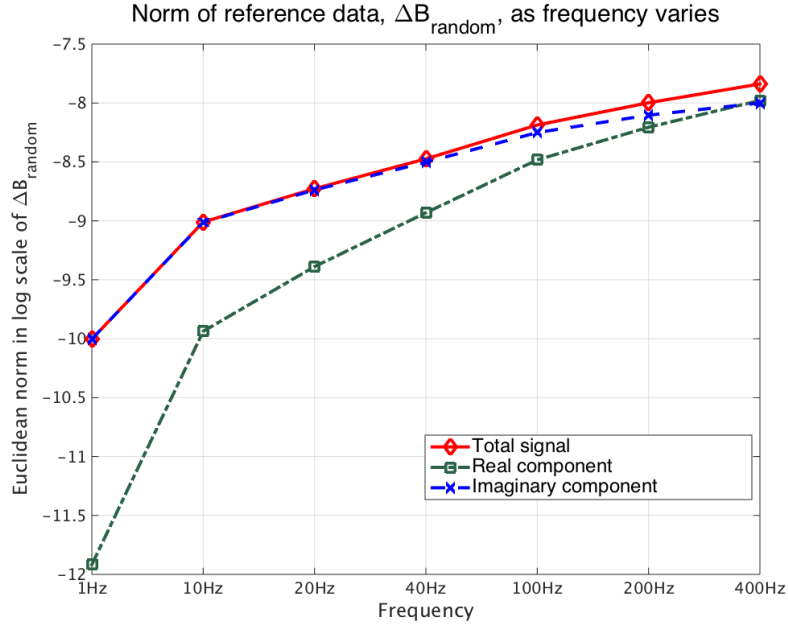
Figure 4.9: Euclidean norm of total, real and imaginary parts of the reference (fine-mesh) solution for the random conductivity model per frequency.

parts of $\Delta B^z_{\text{random}}$ at 100 Hz are shown in Figures 4.11(e) and 4.12(e), respectively.

Finally, we carry out MFV simulations using homogenized electrical conductivity models that we construct using volume-arithmetic, -geometric and -harmonic averaging of the fine-mesh conductivity inside each coarse cell of the OcTree mesh shown in Figure 4.10. The average run time per single simulation is roughly 115 s. The real and imaginary parts of $\Delta B^z_{\text{random}}$ at 100 Hz for each of the three homogenized solutions are shown in Figures 4.11(f), 4.11(g) and 4.11(h), respectively; and Figures 4.12(f), 4.12(g) and 4.12(h), respectively.

Table 4.4 shows the relative errors in Euclidean norm for the total, real and imaginary parts of $\Delta \vec{B}_{\text{random}}$ obtained from comparing the reference (fine-mesh) solution with the MSFV, MSFV+O and MFV with three different homogenized solutions for each frequency and local extended domain size. Table 4.5 shows the relative errors in Euclidean norm for the magnitude of the three components of $\Delta \vec{B}_{\text{random}}$ $(\Delta \vec{B}_{\text{random}} = [\Delta B^x_{\text{random}}, \Delta B^y_{\text{random}}, \Delta B^z_{\text{random}}]^\top)$ obtained from comparing the ref-
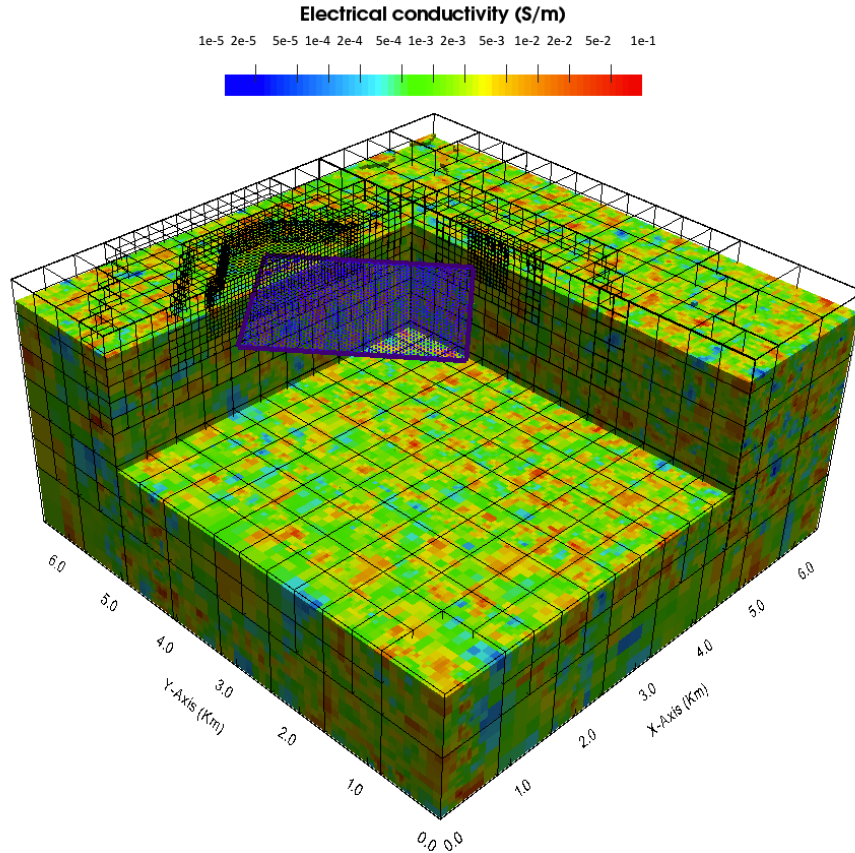
Figure 4.10: Subsurface part of the random heterogeneous isotropic electrical conductivity model and large-loop EM survey setup. The model is discretized on a coarse OcTree mesh with 60,656 cells. The conductivity varies over eight orders of magnitude throughout the whole model.

erence (fine-mesh) solution with the MSFV, MSFV+O and MFV with three different homogenized solutions for each frequency and local extended domain size. Once again, the relative error is computed as the ratio of the Euclidean norm of the difference of the fine and coarse-mesh data to the Euclidean norm of the fine-mesh data. The coarse-mesh solutions are not interpolated to the fine mesh to compute the error. Table 4.6 summarizes the average run time per single simulation required to compute $\Delta\vec{B}_{\text{random}}$ for each of the methods discussed. Figures 4.11 and

4.12 show the results obtained for the real and imaginary parts of $\Delta B_{\text{random}}^z$ with MFV on the fine-mesh, MSFV, MSFV+O with three different oversampling sizes, and MFV with three different homogenized conductivity models for the frequency of 100 Hz, respectively. All results are plotted using the same color scale and range. From these tables and these figures we observe the following:

First, once again, we see that our oversampling technique improves the accuracy for the total, real and imaginary response as well as for each of the three components of the solution in comparison to the MSFV and MFV with three different homogenized conductivity models as the errors decrease with oversampling. As expected, the homogenized conductivity model obtained from using the volume-geometric mean produces the most accurate results as compared to those obtained using volume-arithmetic and volume-harmonic means. The geometric mean provides a reliable approximation of the effective conductivity if the fine-scale variation satisfies certain conditions [163]. We also see that the multi-scaled solutions are more accurate than the homogenized solutions.

Second, using a local extended domain size of 1 fine padding cell suffices to improve the accuracy of the solution when compared with the rest of the methods discussed and it is slightly more expensive than the solution obtained with MSFV. We see that as the size of the local extended domain increases the error also was slightly increased. This small increment in the error is still lower compared to the error of the MSFV solution for most of the cases, except for the imaginary part of $\Delta \vec{B}_{\text{random}}$ at 100 Hz and the real part of $\Delta \vec{B}_{\text{random}}$ at 400 Hz. We attribute the increment in the error to the random and uncorrelated structure of the conductivity model. On the one hand, increasing the oversampling size reduces the effect of the imposed linear boundary conditions. This explains the improved accuracy of the MSFV+O over MSFV. On the other hand, increasing the oversampling size takes into account structures outside the core coarse cell that are not necessarily correlated to the structures inside the core coarse cell. This biases the multiscale basis towards structures outside the core cell and decreases the local approximation quality.

Third, comparing the relative accuracy for the two examples presented we note the two data types differ significantly. In the Lalor example (Section 4.4.1), the data is the response of the deep and buried conductive mineral deposit, which

constitutes a rather weak secondary field compared to the primary field induced by the air and background conductivity (Figure 4.4). In the random medium example, the data is the response of the entire subsurface; the primary field here is only for the air (Figure 4.9). Therefore, the ratio of the secondary to primary field is much higher in the random example than for the Lalor example. Since the level of accuracy of a simulation is relative to the total signal, the accuracy of a weaker secondary signal is lower than for a stronger secondary signal.

Fourth, as in the previous example, the errors for the imaginary part of $\Delta \vec{B}_{random}$ for the frequencies of 1, 10, 20 and 40 Hz resemble the errors for total $\Delta \vec{B}_{random}$ due to the real part of $\Delta \vec{B}_{random}$ is considerably smaller than their corresponding imaginary parts (Figure 4.9). For the frequencies of 100, 200 and 400 Hz, where the real and imaginary parts of $\Delta \vec{B}_{random}$ are roughly in the same order of magnitude (Figure 4.9), we see the relative error for total $\Delta \vec{B}_{random}$ represents the error contributions of these two parts of the data.
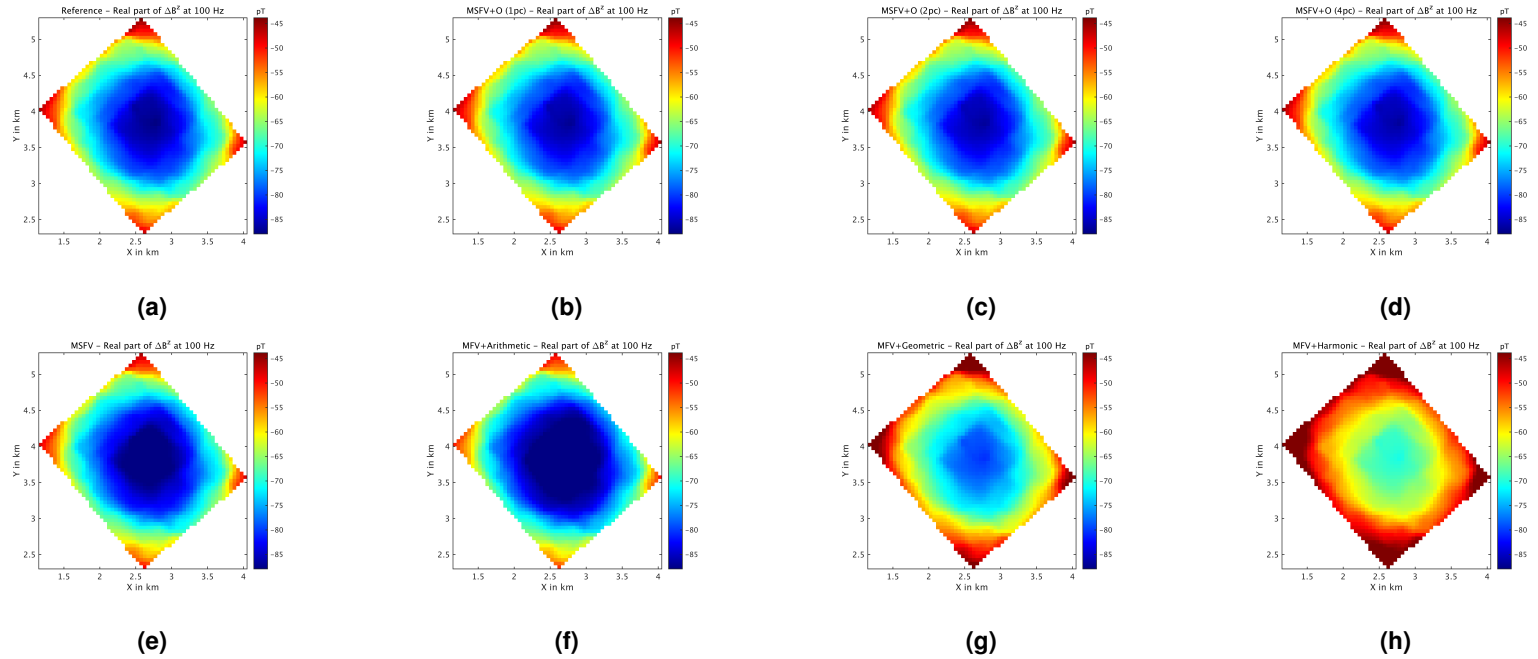
Figure 4.11: Real part of the z component of the secondary magnetic flux induced by the random heterogeneous conductive medium in the survey area, $\Delta B^z_{\text{random}}$, for our large-loop EM survey at 100 Hz. (a) reference solution computed using the MFV method on the fine OcTree mesh with 546,295 cells. (b), (c) and (d): results using the MSFV+O method with 1, 2 and 4 padding cells on the coarse OcTree mesh, respectively. (e): results using the MSFV (without oversampling) method on the coarse OcTree mesh with 60,656 cells. (f), (g) and (h): results using MFV with the conductivity model homogenized using arithmetic, geometric and harmonic averaging on the coarse OcTree mesh, respectively. All results are shown in picoteslas (pT) and plotted using the same color scale.

Figure 4.12: Imaginary part of the z component of the secondary magnetic flux induced by the random heterogeneous conductive medium in the survey area, $\Delta B^z_{\text{random}}$, for our large-loop EM survey at 100 Hz. (a) reference solution computed using the MFV method on the fine OcTree mesh with 546,295 cells. (b), (c) and (d): results using the MSFV+O method with 1, 2 and 4 padding cells on the coarse OcTree mesh, respectively. (e): results using the MSFV (without oversampling) method on the coarse OcTree mesh with 60,656 cells. (f), (g) and (h): results using MFV with the conductivity model homogenized using arithmetic, geometric and harmonic averaging on the coarse OcTree mesh, respectively. All results are shown in picoteslas (pT) and plotted using the same color scale.

Table 4.4: Relative errors in Euclidean norm for the total, real and imaginary parts of the secondary magnetic fluxes induced by the random heterogeneous conductive medium in the survey area, $\Delta\vec{B}_{\text{random}}$. Note that pc stands for padding cells.

Table of relative errors in Euclidean norm for $\Delta\vec{B}_{\text{random}}$							
	Frequency						
Method	1 Hz	10 Hz	20 Hz	40 Hz	100 Hz	200 Hz	400 Hz
Relative errors for total $\Delta\vec{B}_{\text{random}}$ (per cent)							
MFV + Arithmetic	10.50	9.95	8.67	6.27	3.90	2.69	1.81
MFV + Geometric	9.77	9.51	8.83	7.24	4.96	3.35	1.96
MFV + Harmonic	21.38	20.94	19.76	16.53	10.64	7.09	3.84
MSFV	4.41	4.22	3.74	2.77	1.75	1.20	0.76
MSFV+O (1 pc)	0.43	0.53	0.66	0.80	0.66	0.54	0.44
MSFV+O (2 pc)	0.72	0.80	0.94	1.05	0.83	0.64	0.49
MSFV+O (4 pc)	0.93	0.99	1.10	1.17	0.87	0.66	0.49
Relative errors for real part of $\Delta\vec{B}_{\text{random}}$ (per cent)							
MFV + Arithmetic	38.36	35.03	27.89	16.56	7.68	3.52	0.75
MFV + Geometric	25.39	24.38	21.88	16.32	9.33	5.32	2.53
MFV + Harmonic	53.99	52.57	48.75	38.45	20.64	11.03	4.02
MSFV	14.96	13.89	11.46	7.14	3.44	1.67	0.44
MSFV+O (1 pc)	1.60	1.32	0.71	0.72	1.00	0.78	0.59
MSFV+O (2 pc)	0.71	0.50	0.50	1.37	1.38	0.97	0.65
MSFV+O (4 pc)	0.44	0.57	1.02	1.79	1.51	1.02	0.67
Relative errors for imaginary part of $\Delta\vec{B}_{\text{random}}$ (per cent)							
MFV + Arithmetic	10.49	9.11	6.32	2.59	0.44	1.99	2.51
MFV + Geometric	9.77	9.12	7.62	4.79	1.78	0.78	1.00
MFV + Harmonic	21.37	20.14	17.06	10.31	2.35	2.39	3.63
MSFV	4.41	3.91	2.85	1.29	0.24	0.79	0.99
MSFV+O (1 pc)	0.43	0.51	0.67	0.81	0.49	0.31	0.19
MSFV+O (2 pc)	0.73	0.81	0.95	1.00	0.52	0.28	0.19
MSFV+O (4 pc)	0.93	1.00	1.10	1.04	0.48	0.25	0.20

Table 4.5: Relative errors (per cent) in Euclidean norm for the magnitude of the x, y and z components of the secondary magnetic fluxes induced by the mineral deposit in the survey area, $\Delta\vec{B}_{\text{random}}$. Note that pc stands for padding cells.

Method	$\Delta B^x_{\text{random}}$	$\Delta B^y_{\text{random}}$	$\Delta B^z_{\text{random}}$	$\Delta B^x_{\text{random}}$	$\Delta B^y_{\text{random}}$	$\Delta B^z_{\text{random}}$
	Frequency of 1 Hz					
MFV+Arithmetic	8.24	8.56	10.90			
MFV+Geometric	6.80	6.15	10.34			
MFV+Harmonic	16.48	16.06	22.33			
MSFV	3.30	3.34	4.61			
MSFV+O (2 pc)	0.90	0.86	0.26			
MSFV+O (4 pc)	1.13	1.04	0.62			
MSFV+O (8 pc)	1.26	1.18	0.86			
	Frequency of 10 Hz			Frequency of 100 Hz		
MFV+Arithmetic	7.78	8.08	10.33	2.90	3.09	4.12
MFV+Geometric	6.58	5.95	10.07	2.82	2.45	5.43
MFV+Harmonic	16.08	15.66	21.88	7.38	7.00	11.40
MSFV	3.14	3.18	4.41	1.22	1.25	1.87
MSFV+O (2 pc)	0.95	0.91	0.38	0.94	0.89	0.57
MSFV+O (4 pc)	1.17	1.09	0.71	1.06	0.99	0.76
MSFV+O (8 pc)	1.30	1.22	0.92	1.06	0.98	0.82
	Frequency of 20 Hz			Frequency of 200 Hz		
MFV+Arithmetic	6.71	6.97	9.02	2.23	2.44	2.79
MFV+Geometric	6.02	5.43	9.38	1.76	1.57	3.73
MFV+Harmonic	15.03	14.62	20.69	4.81	4.60	7.69
MSFV	2.76	2.78	3.92	0.97	1.04	1.26
MSFV+O (2 pc)	1.04	1.00	0.56	0.78	0.75	0.45
MSFV+O (4 pc)	1.26	1.18	0.86	0.84	0.79	0.58
MSFV+O (8 pc)	1.36	1.28	1.04	0.83	0.77	0.61
	Frequency of 40 Hz			Frequency of 400 Hz		
MFV+Arithmetic	4.72	4.91	6.56	1.83	2.04	1.76
MFV+Geometric	4.70	4.21	7.76	0.92	0.95	2.21
MFV+Harmonic	12.23	11.83	17.42	2.68	2.68	4.18
MSFV	1.98	1.99	2.92	0.83	0.92	0.71
MSFV+O (2 pc)	1.12	1.07	0.71	0.62	0.63	0.35
MSFV+O (4 pc)	1.31	1.24	0.99	0.64	0.63	0.43
MSFV+O (8 pc)	1.37	1.30	1.12	0.62	0.60	0.44

Table 4.6: Average run time in seconds per simulation required to compute $\Delta\vec{B}_{random}$ on a two hexa-core Intel Xeon X5660 CPUs at 2.8 Hz with 64 GB shared RAM using MATLAB. *Setup time*: time required to compute the local interpolation matrices and to assemble the reduced system of equations to be solved. *Solve time*: time to solve the reduced system of equations. *Total time*: the sum of the setup and solve times.

Method	Setup time (s)	Solve time (s)	Total time (s)
MFV on fine OcTree mesh	-	721 s	721 s
MFV + Arithmetic	-	114 s	114 s
MFV + Geometric	-	115 s	115 s
MFV + Harmonic	-	115 s	115 s
MSFV	42 s	32 s	74 s
MSFV+O (1 padding cells)	74 s	32 s	106 s
MSFV+O (2 padding cells)	124 s	32 s	156 s
MSFV+O (3 padding cells)	406 s	33 s	439 s

4.5 Summary

In this chapter, we developed an oversampling technique for the multiscale FV method proposed in [73] to simulate quasi-static EM responses in the frequency domain for geophysical settings that include highly heterogeneous conductive media and features varying at different spatial scales. Simulating these types of geophysical settings requires both large CPU time and memory usage; they often need a very large and fine mesh to be discretized accurately. To the best of my knowledge, this is the first investigation focused on developing an oversampling technique for geophysical EM problems in the multiscale literature.

The method begins by assuming a coarse mesh nested into a fine mesh, which accurately discretizes the geophysical setting. For each coarse cell, we independently solve a local version of the original Maxwell system subject to linear boundary conditions on an extended domain. To solve the local Maxwell system, we use the fine mesh contained in the extended domain and the MFV method (although a FE approach can be used for this part as well). Afterwards, these local solutions, called basis functions, together with a weak-continuity condition are used within a Galerkin approach to construct a coarse-mesh (projected) version of the global problem that is much cheaper to solve.

For the examples presented, the proposed oversampling method significantly improves the accuracy relative to the MSFV method (without oversampling) proposed in [73] at the cost of more computing power, which is still lower than the cost of the fine-mesh solution. Our method produces results comparable to those obtained by simulating EM responses using MFV on a fine mesh, while drastically reducing the size of the linear system of equations and the computational time. Using the oversampling technique in the presented examples in combination with an OcTree mesh (i.e., an adaptive mesh refinement technique), the size of the coarse-mesh system is only about 10% of the fine-mesh system size, while the relative error is significantly reduced for all the cases considered.

Although the examples presented demonstrate a significant advantage of using the MSFV with oversampling (as opposed to using MSFV without oversampling) to forward modeling geophysical EM responses in highly heterogeneous conductive media, there may be some cases where the proposed oversampling

technique may fail. For example, when the underlying conductivity structure contains features with large connectivities (e.g. a steel-cased well). For such cases, one alternative is to use large oversampling domains, which may increase significantly the cost of the forward simulation.

Chapter 5

Concluding Remarks

A smooth sea never made a skillful sailor. — Franklin D. Roosevelt

5.1   Summary of Work and Research Highlights

The aim of this dissertation is to investigate the applicability and feasibility of up-scaling and multiscale methods for efficiently modeling geophysical quasi-static EM frequency-dependent problems. Modeling EM responses in complex geophysical settings is crucial to the exploration, imaging and characterization of buried natural resources, such as mineral and ground water deposits, and hydrocarbon reserves. However, in practice, accurately simulating these types of geophysical settings can be computationally very expensive.

Realistic EM geophysical settings typically consider large computational domains, features that vary at multiple spatial scales, and a wide variation over several orders of magnitude of the physical properties of the heterogeneous media (e.g. electrical conductivity). Since all of these factors can have a significant impact on the behavior of the EM responses of interest, if we need to obtain an accurate approximation to the EM responses, the simulation mesh used in traditional discretization techniques (e.g. FE or FV) should be able to capture the structure of the heterogeneity present in the setting with sufficient detail. This need leads to the use of a very large mesh to discretize the model, which results into solving a very large, and often very ill-conditioned, system of equations —

in some cases, in the order of millions, or even larger than billions of unknowns. Such a large system of equations require specialized computing resources (e.g. clusters) to be solved. When an EM simulation is conducted in practice (e.g. for different frequencies or survey configurations) or within an EM inversion procedure (where there is the need to deal with adjoint operators per frequency and/or source), several forward EM simulations must be conducted [68]. This can lead to a very computational expensive process overall, and therefore it is of interest to reduce effectively the computational cost of individual EM simulations.

In satisfying the aim of this investigation, I initially focused on identifying the core mathematical ideas of some of the successful upscaling and multiscale methods for the problem of modeling single-phase fluid flow in highly heterogeneous porous media, whose leading mathematical model is given by a linear elliptic PDE (i.e., Poisson's equation), which is a real and scalar PDE. Such a problem shares several key challenges similar to the problem of simulating geophysical EM responses in highly heterogeneous settings, namely, the governing PDE model in both problems is linear, the simulation considers large-scale computational domains, features varying at multiple spatial scales, and a wide variation over several orders of magnitude of the physical properties (e.g. permeability) of the media. According to the literature review conducted (see Chapter 2), there is extensive evidence demonstrating that for linear flow in porous media problems, upscaling and multiscale FE/FV methods are able to drastically reduce the cost of the simulation, while yielding results whose accuracy is similar to that of those obtained with FE or FV on a fine mesh. Surprisingly, when I began this investigation, little research was done along these lines for the problem of simulating geophysical EM responses in highly heterogeneous settings.

Once the core mathematical ideas of some of the successful upscaling and multiscale FE/FV methods developed for flow in porous media problems were identified (see Section 2.6), I extended these ideas to develop two new simulation methods for the quasi-static Maxwell's equations in the frequency domain:

1. An upscaling framework for the electrical conductivity, which is thoroughly discussed in Chapter 3. The investigation for this topic resulted in an expanded abstract [29] and a peer-reviewed publication [32].

119

2. A multiscale FV with oversampling method, which is thoroughly discussed in Chapter 4. The investigation for this topic resulted in two expanded abstracts [30] and [31], and a peer-reviewed publication [33].

Both methods were implemented using the parallel computing toolbox of MATLAB, and they can use both tensor and OcTree meshes. In order to test the performance of each method, field-inspired and synthetic examples that include highly heterogeneous conductive media were considered.

The examples presented demonstrate that both proposed upscaling and multiscale with oversampling methods can be feasible and applicable to geophysical quasi-static EM problems in the frequency domain. In addition, this investigation shows that the combination of both methods with locally refined OcTree meshes is particularly advantageous to tackle complex geophysical EM modeling problems. This combination enables both proposed methods to drastically reduce the size of the problem when using a large domain and a mesh that must capture the spatial distribution of the media heterogeneity outside the region where the EM responses are measured. In practice, these two modeling aspects are part of the principle reasons why the cost of geophysical EM simulations is computationally expensive.

The examples presented indicate that the accuracy of a coarse-mesh solution obtained with the two methods proposed in this dissertation depends on two factors. First, the given fine-mesh (conductivity) model should be accurately discretized. The accuracy of the coarse-mesh solution is as good as the accuracy of the conventional discretization method used (in this case MFV) to solve the fine-mesh problem. Second, as it was shown in Sections 3.5 and 4.4, the coarse-mesh needs to be carefully designed because it can significantly impact the quality of the solution. For the examples presented, the mesh is designed to maintain the same resolution as the fine mesh where the EM responses are expected to vary rapidly inside the survey area where they are measured (i.e., at the source(s) and receivers locations). The estimate of the proper cell sizes of the coarse mesh inside the survey area is based on the skin depth, which is a typical mesh-design criterion used in practice for geophysical EM forward modeling simulations [68, 138]. Furthermore, for the conductivity models used to test the two proposed methods,

it is possible to aggressively coarsen the mesh outside the survey area without losing much accuracy. However, aggressively coarsening the mesh outside the survey area may not be possible for all cases. For example, when the underlying electrical conductivity structure have large connectivities.

The set of local Dirichlet boundary conditions (shown in Table 3.3) used to solve the local problems inside every coarse-mesh cell for both proposed upscaling and multiscale with oversampling approaches provided reasonable estimates for the examples presented in this dissertation. However, this set of boundary conditions may not be appropriate to compute accurate coarse-mesh approximations using the proposed two methods for all cases. In this investigation, the use of an extended local domain to solve the local problems mitigated the effect of imposing the chosen local boundary conditions, which may cause a reduction on the accuracy of the coarse-mesh solution for highly heterogeneous conductive media. For example, such effect can be particularly observed when high contrast of conductivity is present at the boundary of a coarse-mesh cell. Although using a local extended domain significantly improved the accuracy of the coarse-mesh solution for the cases considered, there may be other cases where this approach may not be sufficient. For example, when the underlying conductivity structure contains features with rather long connectivities (e.g. a steel-cased well). For such cases, one alternative is to use larger local extended domains, which may come at the cost of more computing time. Similar observations regarding the effect of local boundary conditions and the use of local extended domains are consistent with what has been reported in the upscaling and multiscale literature for flow in porous media problems.

The proposed upscaling method requires a more cautious setup to perform efficiently. It involves a number of parameters to be decided upon depending on the purpose and requirements of the simulation. If the involved parameters are well chosen, the proposed upscaling method retrieves accurate results. Otherwise, the proposed upscaling method can also be quite inaccurate. In general, upscaling methods lack the build-in feature to transition from the coarse mesh to the fine mesh that multiscale approaches have and, often, they lack generality (cf. [23, 51]). The proposed upscaling method is not an exception to this observation. However, if there is the need to generate a coarse-scale electrical conductivity

model from a fine-scale conductivity model, as in the well log conductivity example presented in Section 3.3, the proposed upscaling method offers quite reliable results to do so.

The 3D examples presented in this dissertation, demonstrate that multiscale with oversampling can retrieve accurate solutions at a fraction of the cost of the fine-mesh solution, even when the coarsening is extreme according to the empirical skin depth mesh-design criteria. In contrast, computing an upscaled solution using the proposed upscaling framework is significantly more expensive than computing a fine-mesh or a multiscaled solution. As it was shown in Chapter 3, the computational cost comes from solving a local parameter estimation problem for every coarse cell. In addition, multiscale methods have the built-in feature to interpolate the solution from the coarse mesh to the fine mesh, which opens the door for a natural extension of this methodology to a multilevel method. I will elaborate more about such potential multilevel extension in Section 5.3.

The next two sections summarize the work done and highlight the specific contributions for each of the two methods proposed in this dissertation.

5.1.1   Upscaling: Summary and Highlights

Chapter 3 proposes an upscaling framework for the electrical conductivity that poses upscaling as a least-squares parameter estimation problem. This upscaling framework constructs a coarse-mesh conductivity model by solving a nonlinear optimization problem for each coarse-mesh cell. Such optimization problem minimizes the difference between the user-chosen EM responses, which are computed using the fine- and coarse-scale quasi-static Maxwell's equations. The constructed coarse-mesh conductivity models can be scalar or full SPD tensor models, depending on the purpose and context of the simulation. Contrary to other least-squares upscaling formulations in the literature for flow in porous media problems (Section 2.6.1), the formulation proposed in this investigation does not require regularization and it is practical to tackle 3D geophysical EM problems with arbitrary electrical conductivity structures (for details in the discussion see Section 3.4). For the 1D and 3D examples presented, the size of the coarse-mesh system solved was roughly 10% of the fine-mesh system size, while the

relative errors (in the secondary fields) were less than 5%. To the best of my knowledge, this investigation constitutes the first upscaling approach proposed for geophysical EM problems in the literature.

The proposed upscaling method is more expensive than MFV in a fine mesh as (local) optimization problems need to be solved per coarse-mesh cell; however, since each local problem is formulated independently of the others, the cost can be reduced by using a more efficient parallel implementation of the method on a more powerful machine.

The most important lesson learned from this investigation is that different experiments require different upscaling criteria that result in different upscaled quantities. That is, for a given fine-scale conductivity structure, there is no unique upscaled model which completely describes it. The examples presented demonstrate that using the proposed upscaling method for different frequencies in the survey configuration leads to different upscaled models. Similarly changing the type of EM responses to be matched in the upscaling criterion leads to different upscaled conductivities.

5.1.2 Multiscale with Oversampling: Summary and Highlights

Chapter 4 proposes a MSFV with an oversampling method. Contrary to the case of upscaling methods, where no previous research work along that line was done for geophysical EM problems, the MSFV method for the quasi-static Maxwell's equations was first proposed in [73]. In this investigation, I found that MSFV could produce quite inaccurate solutions due to the effect of the local boundary conditions used to construct the multiscale basis functions in each coarse-mesh cell. In order to solve this issue, I extended the oversampling technique originally proposed by [89], which has been quite effective to tackle a related issue for single-phase flow in porous media problems, for application to geophysical EM problems. In the proposed oversampling technique, the multiscale basis functions are computing using an extended local domain. Doing so, the multiscale basis functions take into account structures outside the core coarse cell and the effect of the local boundary conditions is reduced. Then, the oversampled basis together with a weak-continuity condition are used to construct a coarse-mesh version of

the global problem. To the best of my knowledge, this is the first investigation focused on developing an oversampling technique for geophysical EM problems in the literature.

For the 3D examples presented, the proposed oversampling technique significantly increases the accuracy of the MSFV method at the expense of more computational run time, which however, depending on the size of the extended domain chosen, can still be considerably lower compared to the time of the fine-mesh solution. Although the examples presented demonstrate a significant advantage of using the MSFV with oversampling (as opposed to using MSFV without oversampling) to forward modeling geophysical EM responses in highly heterogeneous conductive media, there may be some cases where the proposed oversampling technique may fail. For example, when the underlying conductivity structure contains features with large connectivities (e.g. a steel-cased well). For such cases, one alternative is to use large oversampling domains, which may increase significantly the cost of the forward simulation.

5.2 Impact to the Field of Computational Methods in Geophysical Electromagnetics

The impact of this investigation to the current field of computational methods in geophysical EM can be summarized in the following three outcomes.

On a theoretical level, one outcome of this study is the advancement of knowledge by contributing two new methods to efficiently solve the quasi-static Maxwell's equations in the frequency domain with highly discontinuous coefficients and features at multiple length scales: (1) an upscaling method and (2) a multiscale FV with oversampling method. Both methods have the potential to be useful for other applications that have the same underlying mathematical model, for example, in the fields of medical imaging and the various engineering branches, such as electrical, mechanical or materials engineering.

On a practical level, a second outcome of this study is that it lays the foundation to develop more efficient and usable parallel computing environments for both multiscale and upscaling methods to simulate EM responses in complex geophysical settings. In particular, these simulation environments combine upscaling

and multiscale methods with adaptive mesh refinement techniques. Doing so increases our current predictive and analytic capabilities by making the simulation of EM responses in larger and more complex geophysical settings more feasible than currently is possible.

A third outcome of this study is that it demonstrates a novel use of upscaling and multiscale methods for geophysical EM applications. Developments in upscaling and multiscale methods have been primarily within the field of modeling flow in porous media. This investigation extends the ideas developed for such methods for application to Maxwell's equations, which is more involved due to the complex, vectorial nature of the Maxwell system.

5.3   Remaining Challenges and Future Research

This study demonstrates the feasibility and applicability of both upscaling and multiscale approaches to simulate EM responses in complex geophysical settings. Nonetheless, there remain some challenges to overcome and there are some interesting paths to extend both research directions.

A natural first extension for both upscaling and multiscale methods proposed here is to adapt them for solving quasi-static EM problems in the time domain. In addition, both proposed methods can be adapted to use a different base discretization method to solve the local Maxwell problems, such as a mimetic FD ([121]) or FE ([104, 131], instead of the MFV method (Section 2.4).

For both proposed upscaling and multiscale methods, the open question remains: 'what is the *best* set of boundary conditions to solve the local problems on each coarse-mesh cell?' An idea for selecting better local boundary conditions would be to incorporate global information in the solution of the problem, as it is done in the upscaling community for local-global approaches (e.g. [49, 61, 112] for flow in porous media upscaling methods.)

This study assumes that only the electrical conductivity (Σ) captures the heterogeneity of the geophysical setting. This is a reasonable assumption as in most geological environments, variations in the Earth's magnetic permeability are insignificant and EM surveys are only sensitive to contrasts in the Earth's electrical conductivity [138]. However, there are geophysical applications where the mag-

netic susceptibility (μ) can be heterogeneous as well. For example, when modeling settings that consider steel-well casing or some ore-bearing rocks, which have very high magnetic permeabilities. An extension of the upscaling framework for μ is possible using the least-squares formulations proposed in Chapter 3. However, it will require a rigorous investigation to make appropriate choices for the number of parameters involved (e.g. data to be matched in the upscaling criterion, boundary conditions for local problems, etc.). Contrary to the upscaling approach, handling both heterogeneous μ and Σ simultaneously in the multiscale FV with oversampling method proposed in Chapter 4 is relatively straight forward. The discretization of the local Maxwell systems required to compute the local projection matrices in this case can be done as described in Section 2.4. The rest of the multiscale-related processes remain the same.

Other possible extensions for the upscaling framework proposed in this study include the construction of complex anisotropic upscaled conductivities, which is of relevance for geophysical EM applications where induced polarization effects appear (e.g. [125]). In addition, the formulation can be adapted to choose the data to be matched in the upscaling criterion among the different electric or magnetic fields or fluxes (i.e., $\vec{E}, \vec{H}, \vec{B}$ or $\vec{J}$), or some combination of them. I elaborated more about these ideas in Sections 3.2 and 3.4.

Another interesting research path is to extend the two-level multiscale FV method for the quasi-static Maxwell's equations into a multilevel method. One of the major challenges along this line is on how to construct a hierarchy of coarse spaces and their corresponding inter-level transfer operators, as well as the corresponding approximation properties that guarantee proper bounds for the discretization error. Once this first (major) challenge has been figure it out, the next major step has to do with designing an efficient parallelization for such a multilevel method. As discussed in Section 2.6.3, the multilevel multiscale mimetic method (M^3) ([119]) and the element-based AMG (AMGe) method ([113, 140]) have shown promising results along these lines for flow in porous media problems. I have conducted some preliminary work along these two directions, which I describe below.

- This study lays the foundation for the construction of oversampled multi-

126

scale basis functions for the electric field, $\vec{E}$ (for every coarse-mesh cell) in a two-level setting. However, in order to construct a hierarchy of coarse spaces required for a robust mimetic multilevel extension, it is also of interest to generate the basis functions for $\vec{B}$. In collaboration with some colleagues at UBC, we are currently investigating the extension of the (two-level) M^3 method to the Maxwell's equations. This investigation focuses on constructing mimetic multiscale basis functions for both $\vec{E}$ and $\vec{B}$, while assuming that both μ and Σ are highly discontinuous (heterogeneous). The extension also considers both frequency- and time-domain EM problems. We have obtained some preliminary positive results. Such results are not documented in this dissertation, since they are out of the scope of this study and they require a significant amount of effort to constitute a full further study.

- While being a summer research intern at Lawrence Livermore National Laboratory, I conducted some preliminary studies on using their (C++) AMGe library to upscale the quasi-static Maxwell's equations in the time domain. Such study focused on investigating the multilevel capability of the AMGe library and its computational performance. In this case, I also obtained some preliminary positive results. Such preliminary results are not documented in this dissertation, since they are off-topic and they require a significant amount of effort to constitute a full further study. However, research along this direction seems promising to speed up the computational performance for further geophysical EM problems.

There are several other research directions to be explored that can lead to interesting extensions for the two methods presented in this dissertation. Only the immediate extensions that I envision where discussed above; however, one can continue to gain inspiration from the current successful developments and applications of both upscaling and multiscale methods in the field of petroleum engineering.

This investigation proposed two innovative mathematical alternatives to improve the computational performance of solving realistic geophysical EM forward problems in a more sustainable way than currently is possible. It also opened the

door to use such alternatives to create more powerful computational environments capable of simulating EM responses in larger and more complex geophysical settings than currently is possible. Working on advancing this type of computational tools is important because they have a tangible impact in the overall processes of imaging and monitoring buried natural resources using geophysical EM methods.

Bibliography

[1] A. Abdulle, E. Weinan, B. Engquist, and E. Vanden-Eijnden. The heterogeneous multiscale method. *Acta Numer.*, 21(April 2012):1–87, apr 2012. ISSN 0962-4929. doi:10.1017/S0962492912000025. → pages 34

[2] R. Alcouffe, A. Brand, J. Dendy, and J. Painter. The Multi-grid method for the difussion equation with strongly discontinuous coefficients. *Siam J. Sci. Stat. Comput.*, 2(4):430–454, 1981. doi:http://epubs.siam.org/doi/abs/10.1137/0902035. → pages 85

[3] P. Amestoy, I. Duff, J. Y. L'Excellent, and J. Koster. MUMPS: a general purpose distributed memory sparse solver. *Int. Work. Appl. Parallel Comput. Springer Berlin Heidelb.*, pages 121–130, 2001. → pages 29, 75, 94

[4] D. A. Aruliah and U. Ascher. Multigrid Preconditioning for Krylov Methods for Time-Harmonic Maxwell's Equations in Three Dimensions. *SIAM J. Sci. Comput.*, 24(2):702–718, jan 2002. ISSN 1064-8275. doi:10.1137/S1064827501387358. → pages 28

[5] D. A. Aruliah, U. Ascher, E. Haber, and D. W. Oldenburg. A method for the forward modelling of 3-D electromagnetic quasi-static problems. *Math. Model. Methods Appl. Sci.*, 11(1):1–21, 2001. doi:10.1142/S0218202501000702. → pages 13, 27, 28

[6] U. Ascher. *Numerical methods for evolutionary differential equations*. Society for Industrial and Applied Mathematics, 2008. ISBN 978-0-898716-52-8. → pages 8, 20, 24

[7] D. Avdeev. Three-dimensional electromagnetic modelling and inversion from theory to application. *Surv. Geophys.*, 26(6):767–799, 2005. doi:10.1007/s10712-005-1836-2. → pages 13

[8] D. Avdeev and S. Knizhnik. 3D integral equation modeling with a linear dependence on dimensions. *Geophysics*, 74(5):F89–F94, sep 2009. ISSN 0016-8033. doi:10.1190/1.3190132. → pages 14

[9] I. Babukat, G. Calozt, and J. E. Osborn. Special Finite Element Methods for a Class of Second Order Elliptic Problems with Rough Coefficients. *SIAM J. Numer. ANAL*, 31(4):945–981, 1994. ISSN 0036-1429. doi:10.1137/0731051. → pages 34, 35

[10] I. Babuška and J. E. Osborn. Generalized finite element methods: Their performance and their relation to mixed methods. *SIAM J. Numer. Anal.*, 20(3):510–536, 1983. ISSN 0036-1429. doi:10.1137/0720034. → pages 35

[11] I. Babuska, U. Banderjee, and J. E. Osborn. Survey of meshless and generalized finite element methods: A unified approach. *Acta Numer.*, 12:1–125, 2003. ISSN 09624929. doi:10.1017/S0962492902000090. → pages 34

[12] E. Badea, M. Everett, G. Newman, and O. Biro. Finite-element analysis of controlled-source electromagnetic induction using Coulomb-gauged potentials. *Geophysics*, 66(3):786–799, 2001. ISSN 00168033. doi:10.1190/1.1444968. → pages 28

[13] P. Benner and K. Willcox. A Survey of Projection-Based Model Reduction Methods for Parametric Dynamical Systems . *SIAM Rev.*, 57(4):483–531, 2015. → pages 35

[14] A. Bensoussan, J.-L. Lions, and G. Papanicolau. *Asymptotic Analysis for Periodic Structures.* North-Holland Pub. Co., New York, vol. 5 edition, 1978. ISBN 0444851720. → pages 30

[15] M. Benzi. Preconditioning Techniques for Large Linear Systems: A Survey. *J. Comput. Phys.*, 182(2):418–477, 2002. ISSN 00219991. doi:10.1006/jcph.2002.7176. → pages 28

[16] A. J. Bergqvist and S. G. Engdahl. A homogenization procedure of field quantities in laminated electric steel. In *IEEE Trans. Magn.*, volume 37, pages 3329–3331, 2001. doi:10.1109/20.952606. → pages 43

[17] A. Bermúdez, D. Gómez, and P. Salgado. Eddy-current losses in laminated cores and the computation of an equivalent conductivity. *IEEE Trans. Magn.*, 44(12):4730–4738, 2008. ISSN 00189464. doi:10.1109/TMAG.2008.2005118. → pages 43

[18] J. G. Berryman and G. M. Hoversten. Modelling electrical conductivity for earth media with macroscopic fluid-filled fractures. *Geophys. Prospect.*, 61 (2):471–493, mar 2013. ISSN 00168025. doi:10.1111/j.1365-2478.2012.01135.x. → pages 31

[19] R. U. Börner. Numerical modelling in geo-electromagnetics: advances and challenges. *Surv. Geophys.*, 31(2):225–245, oct 2010. ISSN 0169-3298. doi:10.1007/s10712-009-9087-x. → pages 3, 4, 13

[20] A. Borzì and V. Schulz. *Computational Optimization of Systems Governed by Partial Differential Equations - Chapter 1.* Society for Industrial and Applied Mathematics, 2012. ISBN 9781611972054. doi:10.1137/1.9781611972054. → pages 46

[21] A. Brandt. Multi-level adaptive solutions to boundary-value problems. *Math. Comput.*, 31(138):333–390, 1977. ISSN 0025-5718. doi:10.1090/S0025-5718-1977-0431719-X. → pages 36

[22] A. Brandt. Multiscale scientific computation: Review 2001. *Multiscale and multiresolution methods*, (6682):3–95, 2002. doi:10.1007/978-3-642-56205-1. → pages 4, 6, 15, 36

[23] A. Brandt. Principles of systematic upscaling. In *Multiscale Methods Bridg. Scales Sci. Eng.*, chapter 7, pages 1–19. Oxford University Press, 2009. ISBN 9780191715532. doi:10.1093/acprof:oso/9780199233854.003.0007. → pages 15, 121

[24] A. Brandt and E. O. Livne. *Multigrid Techniques: 1984 Guide with Applications to Fluid Dynamics, Revised Edition.* Society for Industrial and Applied Mathematics, 2011. ISBN 978-1-61197-074-6. doi:http://dx.doi.org.ezproxy.library.ubc.ca/10.1137/1.9781611970753. → pages 37

[25] R. P. Brent. *Algorithms for Minimization Without Derivatives*, volume 19. Prentice-Hall, 1972. ISBN 0130223352. doi:10.1109/TAC.1974.1100629. → pages 50

[26] M. Brezina, A. J. Cleary, R. D. Falgout, V. E. Henson, J. E. Jones, T. A. Manteuffel, S. F. McCormick, and J. W. Ruge. Algebraic Multigrid Based on Element Interpolation (AMGe). *SIAM J. Sci. Comput.*, 22(5): 1570–1592, 2001. ISSN 1064-8275. doi:10.1137/S1064827598344303. → pages 37, 38

[27] W. L. Briggs, V. E. Henson, and S. F. McCormick. *A Multigrid Tutorial*. Society for Industrial and Applied Mathematics, 2nd edition, 2000. ISBN 9780898714623. doi:http://dx.doi.org.ezproxy.library.ubc.ca/10.1137/1.9780898719505. → pages 28

[28] L. Cao, Y. Zhang, W. Allegretto, and Y. Lin. Multiscale Asymptotic Method for Maxwell's Equations in Composite Materials. *SIAM J. Numer. Anal.*, 47 (6):4257–4289, 2010. doi:10.1137/080741276. → pages 31

[29] L. A. Caudillo-Mata, E. Haber, L. J. Heagy, and D. W. Oldenburg. *Numerical upscaling of electrical conductivity: A problem specific approach to generate coarse-scale models*, chapter 130, pages 680 – 684. Society of Exploration Geophysicists, 2014. doi:10.1190/segam2014-1488.1. → pages 40, 119

[30] L. A. Caudillo-Mata, E. Haber, and C. Schwarzbach. An Oversampling Technique for Multiscale Finite Volume Method to Simulate Frequency-domain Electromagnetic Responses. In *SEG Tech. Progr. Expand. Abstr. 2016*, pages 981 – 985, 2016. doi:10.1190/segam2016-13974625.1. → pages 82, 120

[31] L. A. Caudillo-Mata, E. Haber, and C. Schwarzbach. A Multiscale Finite Volume Method with Oversampling for Geophysical Electromagnetic Simulations. In *EAGE - ECMOR XV - 15th Eur. Conf. Math. Oil Recover. - Expand. Abstr.*, 2016. doi:10.3997/2214-4609.201601892. → pages 82, 120

[32] L. A. Caudillo-Mata, E. Haber, L. J. Heagy, and C. Schwarzbach. A framework for the upscaling of the electrical conductivity in the quasi-static Maxwell's equations. *J. Comput. Appl. Math.*, 317:388–402, 2017. ISSN 03770427. doi:10.1016/j.cam.2016.11.051. → pages 40, 119

[33] L. A. Caudillo-Mata, E. Haber, and C. Schwarzbach. An oversampling technique for the multiscale finite volume method to simulate electromagnetic responses in the frequency domain. *Comput. Geosci.*, pages 1–18, 2017. ISSN 15731499. doi:10.1007/s10596-017-9647-y. → pages 82, 120

[34] J. Chen and Q. H. Liu. Discontinuous Galerkin Time-Domain Methods for Multiscale Electromagnetic Simulations: A Review. *Proc. IEEE*, 101(2): 242–254, feb 2013. ISSN 0018-9219. doi:10.1109/JPROC.2012.2219031. → pages 13

[35] T. Chen. *New Methods for Accurate Upscaling with Full-tensor Effects*. PhD thesis, Stanford University, 2009. → pages 33, 34, 58, 64

[36] T. Chen, M. G. Gerritsen, J. V. Lambers, and L. J. Durlofsky. Global variable compact multipoint methods for accurate upscaling with full-tensor effects. *Comput. Geosci.*, 14(1):65–81, 2010. doi:10.1007/s10596-009-9133-2. → pages 33, 64

[37] Y. Chen, L. J. Durlofsky, M. G. Gerritsen, and X. H. Wen. A coupled localglobal upscaling approach for simulating flow in highly heterogeneous formations. *Adv. Water Resour.*, 26(10):1041–1060, 2003. doi:10.1016/S0309-1708(03)00101-5. → pages 33

[38] C. Christensen. *Multilevel techniques for Reservoir Simulation*. Doctoral dissertation, Technical University of Denmark, 2016. → pages 8, 38

[39] E. Chung, Y. Efendiev, and T. Y. Hou. Adaptive multiscale model reduction with Generalized Multiscale Finite Element Methods. *J. Comput. Phys.*, 320:69–95, 2016. ISSN 10902716. doi:10.1016/j.jcp.2016.04.054. → pages 8, 36

[40] E. T. Chung and J. Zou. The Eigenvalues and Eigenspaces of Some Discrete Div- and Curl-Related Operators. *SIAM J. Matrix Anal. Appl.*, 24 (4):1149, 2003. ISSN 08954798. doi:10.1137/S0895479801382483. → pages 27

[41] M. Commer and G. A. Newman. An accelerated time domain finite difference simulation scheme for three-dimensional transient electromagnetic modeling using geometric multigrid concepts. *Radio Sci.*, 41(3):1–15, 2006. ISSN 00486604. doi:10.1029/2005RS003413. → pages 14

[42] M. Commer, M. B. Kowalsky, J. Doetsch, G. A. Newman, and S. Finsterle. MPiTOUGH2: A parallel parameter estimation framework for hydrological and hydrogeophysical applications. *Comput. Geosci.*, 65:127–135, 2014. ISSN 00983004. doi:10.1016/j.cageo.2013.06.011. → pages 1

[43] T. A. Davis. *Direct Methods for Sparse Linear Systems*. Society for Industrial and Applied Mathematics, 1st edition, 2006. ISBN 0898716136, 9780898716139. → pages 7, 29

[44] J. Dendy. Black box multigrid. *J. Comput. Phys.*, 48(3):366–386, dec 1982. ISSN 00219991. doi:10.1016/0021-9991(82)90057-2. → pages 85

[45] A. J. Desbarats. Numerical estimation of effective permeability in sand-shale formations. *Water Resour. Res.*, 23(2):273–286, 1987. ISSN 19447973. doi:10.1029/WR023i002p00273. → pages 32

[46] A. Druinsky, P. Ghysels, X. S. Li, O. Marques, S. Williams, A. Barker, D. Kalchev, and P. Vassilevski. *Comparative Performance Analysis of Coarse Solvers for Algebraic Multigrid on Multicore and Manycore Architectures*, pages 116–127. Springer International Publishing, Cham, 2016. ISBN 978-3-319-32149-3. doi:10.1007/978-3-319-32149-3_12. → pages 101

[47] L. J. Durlofsky. Numerical calculation of equivalent grid block permeability tensors for heterogeneous porous media. *Water Resour. Res.*, 27(5): 699–708, may 1991. ISSN 00431397. doi:10.1029/91WR00107. → pages 61

[48] L. J. Durlofsky. Coarse scale models of two phase flow in heterogeneous reservoirs: volume averaged equations and their relationship to existing upscaling techniques. *Comput. Geosci.*, 2(2):73–92, mar 1998. ISSN 1573-1499. doi:10.1023/A:1011593901771. → pages 33, 56, 59

[49] L. J. Durlofsky. Upscaling of geocellular models for reservoir flow simulation: a review of recent progress. *7th Int. Forum Reserv. Simul. Bühl/Baden-Baden, Ger.*, pages 1–58, 2003. → pages 8, 30, 31, 32, 33, 34, 46, 51, 56, 58, 59, 61, 62, 64, 79, 125

[50] L. J. Durlofsky, Y. Efendiev, and V. Ginting. An adaptive local-global multiscale finite volume element method for two-phase flow simulations. *Adv. Water Resour.*, 30(3):576–588, 2007. ISSN 03091708. doi:10.1016/j.advwatres.2006.04.002. → pages 33, 36

[51] Y. Efendiev and T. Y. Hou. *Multiscale finite element methods: theory and applications*. Springer New York, 2009. ISBN 9780387094953. doi:10.1007/978-0-387-09496-0. → pages 8, 30, 34, 35, 36, 59, 85, 86, 87, 88, 121

[52] Y. Efendiev, J. Galvis, G. Li, and M. Presho. Generalized Multiscale Finite Element Methods. Oversampling Strategies. *Int. J. Multiscale Comput. Eng.*, 12(6):465–484, 2014. doi:10.1615/IntJMultCompEng.2014007646. → pages 36

[53] R. Eso and D. W. Oldenburg. 3D forward modeling and inversion of CSEM data at the San Nicolas massive sulphide deposit, 2007. → pages 13

[54] R. Eymard, T. Gallouët, and R. Herbin. Finite volume methods (Schemes and Analysis course at the University of Wroclaw), 2000. → pages 14

[55] R. D. Falgout, P. S. Vassilevski, and L. T. Zikatanov. On two-grid convergence estimates. *Numer. Linear Algebr. with Appl.*, 12(5-6): 471–494, 2005. ISSN 10705325. doi:10.1002/nla.437. → pages 37

[56] C. L. Farmer. Upscaling: a review. *Int. J. Numer. Methods Fluids*, 40(1-2): 63–78, 2002. doi:10.1002/fld.267. → pages 8, 30, 31, 32, 34, 44, 46, 51, 59, 61, 62, 64, 79

[57] C. G. Farquharson and D. W. Oldenburg. Inversion of time-domain electromagnetic data for a horizontally layered Earth. *Geophys. J. Int.*, 114 (3):433–442, 1993. ISSN 1365246X. doi:10.1111/j.1365-246X.1993.tb06977.x. → pages 50

[58] D. Fleisch. *A Student's Guide to Maxwell's Equations*. Cambridge University Press, 2008. ISBN 9780521877619. → pages 4, 13, 17, 19

[59] K. Gao, S. Fu, R. L. Gibson, E. T. Chung, and Y. Efendiev. Generalized Multiscale Finite-Element Method (GMsFEM) for elastic wave propagation in heterogeneous, anisotropic media. *J. Comput. Phys.*, 295:161–188, 2015. ISSN 10902716. doi:10.1016/j.jcp.2015.03.068. → pages 8

[60] M. G. Gerritsen and L. J. Durlofsky. Modeling fluid flow in oil reservoirs. *Annu. Rev. Fluid Mech.*, 37(1):211–238, jan 2005. ISSN 0066-4189. doi:10.1146/annurev.fluid.37.061903.175748. → pages 8, 30, 31, 32, 33, 61

[61] M. G. Gerritsen and J. V. Lambers. Integration of localglobal upscaling and grid adaptivity for simulation of subsurface flow in heterogeneous formations. *Comput. Geosci.*, 12(2):193–208, 2008. doi:10.1007/s10596-007-9078-2. → pages 33, 125

[62] P. Ghysels, X. S. Li, F. H. Rouet, S. Williams, and A. Napov. An efficient multi-core implementation of a novel HSS-structured multifrontal solver using randomized sampling. *SIAM J. Sci. Comput.*, 38(5):1–26, 2015. ISSN 10957200. doi:10.1137/15M1010117. → pages 29

[63] G. H. Golub and C. Greif. On Solving Block-Structured Indefinite Linear Systems. *SIAM J. Sci. Comput.*, 24(6):2076–2092, 2003. ISSN 1064-8275. doi:10.1137/S1064827500375096. → pages 7, 28

[64] C. Greif and D. Schötzau. Preconditioners for the discretized time-harmonic maxwell equations in mixed form. *Numer. Linear Algebr. with Appl.*, 14(4):281–297, 2007. → pages 7, 28

[65] A. Gupta and H. Avron. WSMP: Watson Sparse Matrix Package, Part I- direct solution of symmetric systems. Technical Report 98462, IBM Corporation, 2017. → pages 29

[66] E. Haber. A mixed finite element method for the solution of the magnetostatic problem with highly discontinuous coefficients in 3D. *Comput. Geosci.*, 4(4):323–336, 2000. doi:10.1023/A:1011540222718. → pages 28

[67] E. Haber. A parallel method for large scale time domain electromagnetic inverse problems. *Appl. Numer. Math.*, 58(4):422–434, apr 2008. ISSN 01689274. doi:10.1016/j.apnum.2007.01.017. → pages 46

[68] E. Haber. *Computational Methods in Geophysical Electromagnetics*. Society for Industrial and Applied Mathematics, 2014. ISBN 978-1-611973-79-2. → pages 3, 4, 5, 6, 7, 13, 14, 15, 16, 17, 19, 21, 22, 24, 25, 26, 27, 28, 29, 46, 49, 62, 64, 67, 73, 76, 119, 120

[69] E. Haber. Advanced Modeling and Inversion Tools for Controlled Source EM. In *76th EAGE Conf. Exhib.*, number June 2014, pages WS9–B02. EAGE, 2014. doi:10.3997/2214-4609.20140555. → pages 85, 86

[70] E. Haber and U. Ascher. Fast finite volume simulation of 3D electromagnetic problems with highly discontinuous coefficients. *SIAM J. Sci. Comput.*, 22(6):1943–1961, jan 2001. ISSN 1064-8275. doi:10.1137/S1064827599360741. → pages 7, 13, 22, 28

[71] E. Haber and U. Ascher. Preconditioned all-at-once methods for large , sparse parameter estimation problems. *Inverse Probl.*, 17(6):1847–1864, 2001. doi:10.1088/0266-5611/17/6/319. → pages 7

[72] E. Haber and S. Heldmann. An octree multigrid method for quasi-static Maxwell's equations with highly discontinuous coefficients. *J. Comput. Phys.*, 223(2):783–796, may 2007. ISSN 00219991. doi:10.1016/j.jcp.2006.10.012. → pages 7, 26, 75, 76, 94, 105

[73] E. Haber and L. Ruthotto. A multiscale finite volume method for Maxwell's equations at low frequencies. *Geophys. J. Int.*, 199(2):1268 – 1277, 2014. doi:10.1093/gji/ggu268. → pages 11, 36, 81, 82, 83, 85, 86, 96, 101, 116, 123

136

[74] E. Haber and L. Ruthotto. A multiscale finite volume method for Maxwell's equations at low frequencies. *Geophys. J. Int.*, 199(2):1268–1277, 2014. doi:10.1093/gji/ggu268. → pages 34

[75] E. Haber, U. Ascher, D. A. Aruliah, and D. W. Oldenburg. Fast simulation of 3D electromagnetic problems using potentials. *J. Comput. Phys.*, 163(1): 150–171, 2000. doi:10.1006/jcph.2000.6545. → pages 27

[76] E. Haber, U. Ascher, and D. W. Oldenburg. 3D forward modelling of time domain electromagnetic data. *2002 SEG Annu. Meet.*, (1):1–4, 2002. → pages 13

[77] R. Haberman. Elementary Applied Partial Differential Equations With Fourier Series and Boundary Value Problems, 1987. → pages 13

[78] H. Haddar, R. Hiptmair, P. Monk, and R. Rodriguez. *Computational Electromagnetism*. Springer International Publishing, Cetraro, Italy, 2015 edition, 2015. ISBN 9783319193052. doi:10.1007/978-3-319-19306-9. → pages 4

[79] H. Hajibeygi and P. Jenny. Multiscale finite-volume method for parabolic problems arising from compressible multiphase flow in porous media. *J. Comput. Phys.*, 228:5129–5147, 2009. ISSN 00219991. doi:10.1016/j.jcp.2009.04.017. → pages 35, 87

[80] H. Hajibeygi and P. Jenny. Adaptive iterative multiscale finite volume method. *J. Comput. Phys.*, 230(3):628–643, feb 2011. ISSN 00219991. doi:10.1016/j.jcp.2010.10.009. → pages 8

[81] H. Hajibeygi, G. Bonfigli, M. Hesse, and P. Jenny. Iterative multiscale finite-volume method. *J. Comput. Phys.*, 227(19):8604–8621, oct 2008. ISSN 00219991. doi:10.1016/j.jcp.2008.06.013. → pages 8, 35

[82] P. Henning and D. Peterseim. Oversampling for the multiscale finite element method. *SIAM Multiscale Model. Simul.*, 11(4):1149–1175, 2013. doi:10.1137/120900332. → pages 36

[83] R. Hiptmair. Multigrid Method for Maxwell's Equations. *SIAM J. Numer. Anal.*, 36(1):204–225, 1998. doi:10.1137/S0036142997326203. → pages 7, 28

[84] R. Hiptmair. Analysis of Multilevel Methods for Eddy Current Problems. *AMS Math. Comput.*, 72(243):1281–1303, 2003. doi:10.1090/S0025-5718-02-01468-0. → pages 28

[85] L. Holden and B. F. Nielsen. Global upscaling of permeability in heterogeneous reservoirs; the Output Least Squares (OLS) method. *Transp. Porous Media*, 40(2):115–143, 2000. ISSN 01693913. doi:10.1023/A:1006657515753. → pages 34, 46, 61

[86] L. Horesh and E. Haber. A Second Order Discretization of Maxwell's Equations in the Quasi-Static Regime on OcTree Grids. *SIAM J. Sci. Comput.*, 33(5):2805–2819, 2011. doi:10.1137/100798508. → pages 7, 26, 75, 76, 94, 105

[87] M. F. Horstemeyer. *Practical Aspects of Computational Chemistry*. Springer Netherlands, Dordrecht, 2010. ISBN 978-90-481-2686-6. doi:10.1007/978-90-481-2687-3. → pages 8

[88] T. Y. Hou. Numerical Approximations to Multiscale Solutions in Partial Differential Equations. In *Front. Numer. Anal.*, pages 241–301. Springer, 2003. → pages 8, 87

[89] T. Y. Hou and X. Wu. A Multiscale Finite Element Method for Elliptic Problems in Composite Materials and Porous Media. *J. Comput. Phys.*, 134(1):169–189, jun 1997. ISSN 00219991. doi:10.1006/jcph.1997.5682. → pages 8, 34, 35, 36, 83, 85, 87, 88, 90, 123

[90] T. Y. Hou, X. Wu, and Z. Cai. Convergence of a Multiscale Finite Element Method for Elliptic Problems with Rapidly Oscillating Coefficients. *Math. Comput. Am. Math. Soc.*, 68(227):913–943, 1999. doi:10.1155/2013/764165. → pages 35, 36

[91] L. J. Hughes. A Short History of Electrical Techniques in Petroleum Exploration. Technical report, Zonge Engineering & Research Organization, Inc., Tucson, Arizona, U.S.A., 2013. → pages 1

[92] T. J. Hughes, G. R. Feijóo, L. Mazzei, and J. B. Quincy. The variational multiscale methoda paradigm for computational mechanics. *Comput. Methods Appl. Mech. Eng.*, 166(1-2):3–24, 1998. ISSN 00457825. doi:10.1016/S0045-7825(98)00079-6. → pages 34

[93] J. M. Hyman and M. Shashkov. Adjoint operators for the natural discretizations of the divergence, gradient and curl on logically rectangular grids. *Appl. Numer. Math.*, 25(4):413–442, 1997. doi:10.1016/S0168-9274(97)00097-4. → pages 15, 17, 18, 19, 21

[94] J. M. Hyman and M. Shashkov. Natural Discretizations for the Divergence, Gradient, and Curl on Logically Rectangular Grids. *Comput. Math. with Appl.*, 33(4):81–104, 1997. doi:10.1016/S0898-1221(97)00009-6. → pages 18, 19, 21

[95] J. M. Hyman and M. Shashkov. Mimetic discretizations for Maxwell equations and the equations of magnetic diffusion. Technical report, United States. Department of Energy. Office of Energy Research, 1998. → pages 21

[96] J. M. Hyman and M. Shashkov. Mimetic discretizations for Maxwell's equations. *J. Comput. Phys.*, 151(2):881–909, may 1999. ISSN 00219991. doi:10.1006/jcph.1999.6225. → pages 15, 21, 25

[97] J. M. Hyman and M. Shashkov. The orthogonal decomposition theorems for mimetic finite difference methods. *SIAM J. Numer. Anal.*, 36(3): 788–818, jan 1999. ISSN 0036-1429. doi:10.1137/S0036142996314044. → pages 21

[98] J. M. Hyman and M. Shashkov. Mimetic Finite Difference Methods for Maxwell's Equations and the Equations of Magnetic Diffusion. *Prog. Electromagn. Res.*, 32:89–121, 2001. → pages 17, 18

[99] U. S. Inan and R. A. Marshall. *Numerical Electromagnetics: The FDTD Method.* Cambridge University Press, 2011. ISBN 9780521190695. → pages 14

[100] H. Jahandari, S. Ansari, and C. G. Farquharson. Comparison between staggered grid finitevolume and edgebased finiteelement modelling of geophysical electromagnetic data on unstructured grids. *J. Appl. Geophys.*, 138:185–197, 2017. doi:10.1016/j.jappgeo.2017.01.016. → pages 6, 14, 28

[101] P. Jenny, S. Lee, and H. Tchelepi. Multi-scale finite-volume method for elliptic problems in subsurface flow simulation. *J. Comput. Phys.*, 187(1): 47–67, may 2003. ISSN 00219991. doi:10.1016/S0021-9991(03)00075-5. → pages 8, 34, 35, 36, 83, 87

[102] X. Jiang and W. Zheng. Homogenization of Quasi-Static Maxwell's equations. *Multiscale Model. Simul.*, 12(1):152–180, 2014. doi:10.1137/130921398. → pages 31

[103] V. V. Jikov, O. A. Oleinik, and S. M. Kozlov. *Homogenization of differential operators and integral functionals*. Springer-Verlag, 1st edition, 1994. ISBN 9783642846618. doi:10.1007/978-3-642-84659-5. → pages 30, 31

[104] J. Jin. *The Finite Element Method in Electromagnetics*. Wiley, New York, 2nd edition, 2002. ISBN 978-0-471-43818-2. → pages 14, 15, 17, 18, 21, 22, 59, 84, 85, 125

[105] J. E. Jones and B. Lee. A multigrid method for variable coefficient maxwell's equations. *SIAM J. Sci. Comput.*, 27(5):1689–1708, 2006. doi:10.1137/040608283. → pages 28

[106] A. Kelbert, N. Meqbel, G. D. Egbert, and K. Tandon. ModEM: A modular system for inversion of electromagnetic geophysical data. *Comput. Geosci.*, 66:40–53, 2014. ISSN 00983004. doi:10.1016/j.cageo.2014.01.010. → pages 13, 14

[107] C. T. Kelley. *Iterative methods for optimization*. Society for Industrial and Applied Mathematics, 1999. ISBN 0898714338, 9780898714333. doi:http://dx.doi.org.ezproxy.library.ubc.ca/10.1137/1.9781611970920. → pages 62

[108] K. Key and J. Ovall. A parallel goal-oriented adaptive finite element method for 2.5D electromagnetic modelling. *Geophys. J. Int.*, 186(1): 137–154, 2011. doi:10.1111/j.1365-246X.2011.05025.x. → pages 7

[109] S. Knapek. Matrix-dependent multigrid homogenization for diffusion problems. *SIAM J. Sci. Comput.*, 20(2):515—-533 (electronic), 1998. ISSN 1064-8275. doi:10.1137/S1064827596304848. → pages 37

[110] G. Kristensson and N. Wellander. Homogenization of the Maxwell equations at fixed frequency. *SIAM J. Appl. Math.*, 64(1):170–195, 2003. ISSN 0036-1399. doi:10.1137/S0036139902403366. → pages 31, 43

[111] A. Kumar, L. Farmer, G. L. Jerauld, and D. Li. Efficient upscaling from cores to simualtion models. In *SPE Annu. Tech. Conf. Exhib. SPE-38744-MS*, pages 1–16, San Antonio, Texas, 1997. Society of Petroleum Engineers. doi:10.2118/38744-MS. → pages 30

[112] J. V. Lambers, M. G. Gerritsen, and D. Fragola. Multiphase 3-D Flow Simulation with Integrated Upscaling, MPFA Discretization and Adaptivity. In *SPE Reserv. Simul. Symp. 2-4 February, Woodlands, Texas*, number SPE-118983-MS. Society of Petroleum Engineers, 2009. doi:10.2118/118983-MS. → pages 33, 125

[113] I. V. Lashuk and P. S. Vassilevski. The construction of the coarse de Rham complexes with improved approximation properties. *Comput. Methods Appl. Math.*, 14(2):257–303, 2014. ISSN 16099389. doi:10.1515/cmam-2014-0004. → pages 38, 126

[114] C. S. Lee. *Generalization of Mixed Multiscale Finite Element Methods with Applications*. Doctoral dissertation, Texas A&M University, 2016. → pages 8, 36, 38

[115] J. Li, C. G. Farquharson, and X. Hu. 3D vector finite-element electromagnetic forward modeling for large loop sources using a total-field algorithm and unstructured tetrahedral grids. *Geophysics*, 82(1):E1–E16, 2017. ISSN 0016-8033. doi:10.1190/geo2016-0004.1. → pages 14, 28

[116] X. S. Li and J. W. Demmel. SuperLU_DIST: A scalable distributed-memory sparse direct solver for unsymmetric linear systems. *ACM Trans. Math. Softw.*, 29(2):110–140, 2003. ISSN 00983500. doi:10.1145/779359.779361. → pages 29

[117] C. J. Lin and J. J. Moré. Newton's method for large bound-constrained optimization problems. *SIAM J. Optim.*, 9(4):1100–1127, jan 1999. ISSN 1052-6234. doi:10.1137/S1052623498345075. → pages 62

[118] K. Lipnikov, J. Morel, and M. Shashkov. Mimetic finite difference methods for diffusion equations on non-orthogonal non-conformal meshes. *J. Comput. Phys.*, 199:589–597, 2004. ISSN 00219991. doi:10.1016/j.jcp.2004.02.016. → pages 7

[119] K. Lipnikov, J. D. Moulton, and D. Svyatskiy. A multilevel multiscale mimetic (M3) method for two-phase flows in porous media. *J. Comput. Phys.*, 227: 6727–6753, 2008. ISSN 00219991. doi:10.1016/j.jcp.2008.03.029. → pages 30, 38, 126

[120] K. Lipnikov, J. D. Moulton, and D. Svyatskiy. Adaptive Strategies in the Multilevel Multiscale Mimetic Method for Two-Phase Flows in Porous Media. *Multiscale Model. Simul.*, 9(3):991–1016, 2011. ISSN 1540-3459. doi:10.1137/100787544. → pages 38

[121] K. Lipnikov, G. Manzini, and M. Shashkov. Mimetic finite difference method. *J. Comput. Phys.*, 257(PB):1163–1227, 2014. ISSN 10902716. doi:10.1016/j.jcp.2013.07.031. → pages 15, 18, 125

[122] S. MacLachlan. *Improving Robustness in Multiscale Methods*. PhD thesis, University of Colorado, 2004. → pages 8, 15, 30, 31, 32, 39

[123] S. MacLachlan and J. D. Moulton. Multilevel upscaling through variational coarsening. *Water Resour. Res.*, 42(2):W02418:1–9, 2006. doi:10.1029/2005WR003940.1. → pages 8, 36, 39, 83

[124] N. K. Madsen and R. W. Ziolkowski. A Three-Dimensional Modified Finite Volume Technique for Maxwell's Equations. *Electromagnetics*, 10(1-2): 147–161, 1990. doi:10.1080/02726349008908233. → pages 25

[125] D. Marchant, E. Haber, L. Beran, and D. W. Oldenburg. 3D modeling of IP effects on electromagnetic data in the time domain. *SEG 2012 Expand. Abstr.*, pages 1–5, 2012. → pages 126

[126] A. Menshov, Y. Brick, C. Torres-Verdin, and A. E. Yilmaz. Recent progress in rigorous algorithms for the fast solution of 3-D EM frequency-domain integral-equations. In *6th Int. Symp. Three-Dimensional Electromagn. Berkeley,*, pages 1–4, Berkely, California, 2017. → pages 14

[127] G. W. Milton. *The theory of composites*. Cambridge University Press, Cambridge; New York, 2002. ISBN 0521781256. → pages 31

[128] Y. Mitsuhata and T. Uchida. 3D magnetotelluric modeling using the T-Ω finite-element method, 2004. ISSN 00168033. → pages 28

[129] R. Mittra. *Computational Electromagnetics Recent Advances and Engineering Applications*. Springer New York, 2014. ISBN 9781461443810. → pages 4

[130] P. Monk. An analysis of Nedelec's method for the spatial discretization of Maxwell's equations. *J. Comput. Appl. Math.*, 47(1):101–121, 1993. doi:10.1016/0377-0427(93)90093-Q. → pages 14, 90

[131] P. Monk. *Finite element methods for Maxwell's equations*. Clarendon, 2003. ISBN 9780198508885, 0198508883. doi:10.1093/acprof:oso/9780198508885.001.0001. → pages 14, 15, 18, 19, 21, 22, 25, 59, 84, 85, 90, 125

[132] J. D. Moulton, J. E. Dendy, and J. M. Hyman. The black box multigrid numerical homogenization algorithm. *J. Comput. Phys.*, 108(142):80–108, 1998. doi:10.1006/jcph.1998.5911. → pages 8, 32

[133] W. A. Mulder. Geophysical modelling of 3D electromagnetic diffusion with multigrid. *Comput. Vis. Sci.*, 11(3):129–138, 2008. doi:10.1007/s00791-007-0064-y. → pages 28

[134] G. A. Newman. A Review of High-Performance Computational Strategies for Modeling and Imaging of Electromagnetic Induction Data, 2014. ISSN 01693298. → pages 3, 4, 6, 7, 13, 27, 28

[135] G. A. Newman and D. L. Alumbaugh. Frequency-domain modelling of airborne electromagnetic responses using staggered finite differences. *Geophys. Prospect.*, 43(8):1021–1042, nov 1995. ISSN 0016-8025. doi:10.1111/j.1365-2478.1995.tb00294.x. → pages 18, 28

[136] B. F. Nielsen and A. Tveito. An upscaling method for one-phase flow in heterogeneous reservoirs . A weighted output least squares (WOLS) approach. *Comput. Geosci.*, 2:93–123, 1998. ISSN 14200597. doi:10.1023/A:1011541917701. → pages 34, 44, 46, 61

[137] J. Nocedal and S. J. Wright. *Numerical Optimization*. Springer New York, 2nd edition, 2006. ISBN 9780387303031. doi:10.1007/978-0-387-40065-5. → pages 62, 67

[138] D. W. Oldenburg and Y. Li. Inversion for applied geophysics: a tutorial. In *Near-Surface Geophys.*, chapter 5, pages 89–150. Society of Exploration Geophysicists, 2005. ISBN 978-1-56080-130-6. doi:10.1190/1.9781560801719.ch5. → pages 3, 9, 120, 125

[139] D. W. Oldenburg and D. A. Pratt. Geophysical inversion for mineral exploration: A decade of progress in theory and practice. *Proc. Explor.*, 2007. → pages 1, 3, 4

[140] J. E. Pasciak and P. S. Vassilevski. Exact de Rham sequences on spaces defined on macro-elements in two and three spatial dimensions. *SIAM J. Sci. Comput.*, 30(5):2427–2446, 2008. doi:https://doi.org/10.1137/070698178. → pages 38, 126

[141] G. Pavliotis and A. Stuart. *Multiscale methods: averaging and homogenization*. Springer New York, 2008. ISBN 9780387738284. doi:10.1007/978-0-387-73829-1. → pages 8, 31

[142] A. Raiche. Modelling and inversion progress, problems and challenges. *Surv. Geophys.*, 15(2):159–207, 1994. doi:10.1007/BF00689859. → pages 13

[143] P. Renard and G. de Marsily. Calculating equivalent permeability: a review. *Adv. Water Resour.*, 20(5-6):253–278, 1997. ISSN 03091708. doi:10.1016/S0309-1708(96)00050-4. → pages 30

[144] J. M. Reynolds. *An introduction to applied and environmental geophysics*. John Wiley, 1997. ISBN 9780471955559, 0471955558, 9780471968023, 0471968021. → pages 1, 2, 7, 9, 16, 29, 48, 49

[145] K. F. Riley, M. P. Hobson, and S. J. Bence. *Mathematical methods for physics and engineering*. Cambridge University Press, 3rd edition, 2006. ISBN 0521861535, 9780521861533, 0521679710, 9780521679718. → pages 20, 21, 28

[146] Y. Saad. *Iterative Methods for Sparse Linear Systems*. Society for Industrial and Applied Mathematics, 2nd edition, 2003. ISBN 9780898718003. doi:10.2277/0898715342. → pages 7, 27, 28

[147] X. Sánchez-Vila, J. P. Girardi, and J. Carrera. A synthesis of approaches to upscaling of hydraulic conductivities. *Water Resour. Res.*, 31(4): 867–882, 1995. doi:10.1029/94WR02754. → pages 30

[148] O. Schenk, K. Gärtner, W. Fichtner, and A. Stricker. PARDISO: a high-performance serial and parallel sparse linear solver in semi-conductor device simulation. *Futur. Gener. Comput. Syst.*, 18(1):69–78, 2001. → pages 29

[149] C. Schwarzbach. *Stability of finite element discretization of Maxwell's equations for geophysical applications*. PhD thesis, University of Frieberg, Germany, 2009. → pages 7, 14, 15, 18, 28, 29

[150] C. Schwarzbach and E. Haber. Finite element based inversion for time-harmonic electromagnetic problems. *Geophys. J. Int.*, 193(2): 615–634, feb 2013. ISSN 0956-540X. doi:10.1093/gji/ggt006. → pages 14

[151] B. Shafiro and M. Kachanov. Anisotropic effective conductivity of materials with nonrandomly oriented inclusions of diverse ellipsoidal shapes. *J. Appl. Phys.*, 87(12):8561–8569, 2000. ISSN 00218979. doi:10.1063/1.373579. → pages 31

[152] J. Smith. Conservative modeling of 3-D electromagnetic fields, Part I: Properties and error analysis. *Geophysics*, 61(5):1308–1318, sep 1996. ISSN 0016-8033. doi:10.1190/1.1444054. → pages 28

[153] R. Smith. Electromagnetic Induction Methods in Mining Geophysics from 2008 to 2012. *Surv. Geophys.*, 35(1):123–156, apr 2013. ISSN 0169-3298. doi:10.1007/s10712-013-9227-1. → pages 1, 3, 4, 13

[154] L. P. Song, S. D. Billings, L. R. Pasion, and D. W. Oldenburg. Transient Electromagnetic Scattering of a Metallic Object Buried in Underwater Sediments. *IEEE Trans. Geosci. Remote Sens.*, 54(2):1091–1102, 2016. ISSN 01962892. doi:10.1109/TGRS.2015.2473851. → pages 1

[155] K. Steklova and E. Haber. Joint hydrogeophysical inversion: state estimation for seawater intrusion models in 3D. *Comput. Geosci.*, 21(1): 75–94, 2017. ISSN 15731499. doi:10.1007/s10596-016-9595-y. → pages 1

[156] J. A. Stratton. *Electromagnetic Theory*. John Wiley & Sons, Inc., 2007. → pages 4, 13, 16

[157] R. Streich. 3D finite-difference frequency-domain of controlled-source electromagnetic data: Direct solution and optimization for high accuracy. *Geophysics*, 74(5):F95–F105, 2009. doi:10.1190/1.3196241. → pages 13, 28

[158] A. Tarantola. Logarithmic parameters. 2001. → pages 13

[159] A. Tarantola. *Inverse problem theory and methods for model parameter estimation*. Society for Industrial and Applied Mathematics, Paris, 2005. ISBN 0898715725, 9780898715729. → pages 3, 4

[160] H. Tchelepi, P. Jenny, S. Lee, and C. Wolfsteiner. An Adaptive Multiphase Multiscale Finite Volume Simulator for Heterogeneous Reservoirs. In *SPE Reserv. Simul. Symp.*, pages 1–10, 2005. doi:10.2118/93395-MS. → pages 35

[161] W. M. Telford, L. P. Geldart, and R. E. Sheriff. *Applied Geophysics*, volume 2nd. Cambridge University Press, 2nd edition, 1990. ISBN 9781139167932. doi:http://dx.doi.org/10.1017/CBO9781139167932.009. → pages 1, 2, 5, 9, 16

[162] The MathWorks Inc. MATLAB and Statsistics Toolbox Release 2011b. Technical report, Massachusetts, United States, 2014. → pages 50, 75, 94

[163] S. Torquato. *Random heterogeneous materials: microstructure and macroscopic properties*. Springer, 2002. ISBN 0387951679. → pages 30, 31, 67, 109

[164] U. Trottenberg, C. Oosterlee, and A. Schuller. *Multigrid*. Academic Press, 2000. ISBN 012701070X. → pages 28, 37

[165] E. S. Um, M. Commer, G. A. Newman, and G. M. Hoversten. Finite element modelling of transient electromagnetic fields near steel-cased wells. *Geophys. J. Int.*, 202(2):901–913, 2015. ISSN 0956-540X. doi:10.1093/gji/ggv193. → pages 18

[166] M. A. Vallée, R. S. Smith, and P. Keating. Metalliferous mining geophysics State of the art after a decade in the new millennium. *Geophysics*, 76(4): W31–W50, 2011. doi:10.1190/1.3587224. → pages 1, 3, 4, 13

[167] P. S. Vassile. Coarse Spaces By Algebraic Multigrid: Multigrid Convergence and Upscaling Error Estimates. *Adv. Adapt. Data Anal.*, 03 (01n02):229–249, 2011. ISSN 1793-5369. doi:10.1142/S1793536911000830. → pages 36, 37, 38

[168] P. E. Wannamaker and G. W. Hohmann. Electromagnetic modeling of three-dimensional bodies in layered earths using integral equations. Technical Report January, University of Utah Research Institute, Earth Science Laboratory, 1982. → pages 14, 28

[169] S. H. Ward and G. W. Hohmann. Electromagnetic theory for geophysical applications. In M. N. Nabighian, editor, *Electromagn. methods Appl. Geophys.*, volume 1, chapter 4, pages 130–311. Society of Exploration Geophysicists, 1988. ISBN 978-1-56080-263-1. → pages 4, 9, 13, 14, 16, 17, 18, 26, 42, 46, 49, 73, 88

[170] J. E. Warren and H. S. Price. Flow in Heterogeneous Porous Media. *Soc. Pet. Eng. J.*, 1(03):153–169, 1961. ISSN 0197-7520. doi:10.2118/1579-G. → pages 32

[171] E. Weinan, B. Engquist, X. Li, W. Ren, and E. Vanden-Eijnden. Heterogeneous multiscale methods: a review. *Commun. Comput. Phys.*, 2 (3):367–450, 2007. → pages 34

[172] C. J. Weiss and G. A. Newman. Electromagnetic induction in a generalized 3D anisotropic earth, Part 2: The LIN preconditioner. *Geophysics*, 68(3): 922–930, 2003. ISSN 00168033. doi:10.1190/1.1581044. → pages 7, 28

[173] N. Wellander. Homogenization of the Maxwell's equations: case I. Linear Theory. *Appl. Math.*, 46(1):29–51, 2001. doi:10.1023/A:1013727504393. → pages 31, 43

[174] N. Wellander. Homogenization of the Maxwell equations: Case II. Nonlinear conductivity. *Appl. Math.*, 47(3):255–283, 2002. doi:10.1023/A:1021797505024. → pages 31, 43

[175] X. H. Wen and J. J. Gómez-Hernández. Upscaling hydraulic conductivities in heterogeneous media: An overview. *J. Hydrol.*, 183(1):ix – xxxii, 1996. doi:10.1016/S0022-1694(96)80030-8. → pages 8, 30, 31, 32, 33, 34, 59, 61, 79

[176] D. Wynne, M. Attalla, T. Berezniuk, H. Berhane, D. K. Cotterill, R. Strobl, and D. M. Wightman. Athabasca Oil Sands Database. McMurray/Wabiskaw Deposit. Alberta Geological Survey. Technical report, Alberta Research Council, Edmonton, 1994. → pages 49

[177] D. Yang, D. Fournier, and D. W. Oldenburg. 3D Inversion of EM data at Lalor mine: in pursuit of a unified electrical conductivity model. In *Explor. Deep VMS Ore Bodies Hudbay Lalor Case Study*, pages 1–4. BC Geophysical Society, 2014. → pages 71, 92

[178] K. Yee. Numerical Solution of Initial Boundary Value Problems Involving Maxwell's Equations in Isotropic Media. *Antennas Propagation, IEEE Trans.*, 14(3):302–307, 1966. → pages 14, 18

[179] M. S. Zhdanov. Electromagnetic geophysics: Notes from the past and the road ahead. *Geophysics*, 75(5):75A49–75A66, sep 2010. ISSN 0016-8033. doi:10.1190/1.3483901. → pages 1, 3, 4, 9, 13